Royal Netherlands
Meteorological Institute
Ministry of Infrastructure
and Water Management

TROPOMI ATBD of the total and tropospheric NO_2 data products

TROPOMI

sentinel-5p

document number	:	S5P-KNMI-L2-0005-RP
authors	:	J.H.G.M. van Geffen, H.J. Eskes, K.F. Boersma and J.P. Veefkind, with help of M. Sneep and M. ter Linden
CI identification	:	CI-7430-ATBD
issue	:	2.9.0
applicable to processor release	:	2.9.1
product DOI	:	10.5270/S5P-9bnp8q8
date	:	2025-10-27
status	:	released

Document approval record

This document was prepared by J.H.G.M. van Geffen, H.J. Eskes, K.F. Boersma and J.P. Veefkind, with help of M. Sneep and M. ter Linden. It was checked by S. Beirle, A. Richter, B. Sanders.

Document change record

issue	date	item	comments
0.0.1	2012-08-17	All	Initial draft version
0.0.2	2012-09-12	All	Major reordering, adding text and references throughout
0.0.3	2012-09-26	6.1–6.2 7.1–7.2	Several small corrections and additions
0.1.0	2012-09-26	—	First official release
0.2.0	2012-11-15	5.1–5.4 6.1–6.2	Large number of updates throughout the text after internal reviewing by the TROPOMI Level-2 Working Group
0.2.1	2013-04-10	5, 6, 7	Document number corrected, reorganisation of Sect. 6; removal of the discussion on an alternative retrieval approach; various minor corrections, updates and additions
0.2.2	2013-06-03	5, 6, 7 8, 9, 10	Major updates and further reorganisation of Sect. 5–7 first versions of Sect. 8–10
0.3.0	2013-06-04	—	Release for Level-2 Working Group review
0.3.1	2013-06-19	5.1–5.3 6.2–6.6 7.3–7.5 8.4, 9.2	Correction and additions resulting from v0.3.0 internal Level-2 Working Group review, and other minor corrections and additions
0.5.0	2013-06-20	—	Release for external review
0.5.1	2013-09-05	5.1–5.2 6.1–6.6 7.2, 7.5	First round of updates taking into account comments and suggestions of the reviewers of version 0.5.0
0.5.2	2013-11-21	5.5 6.2–6.7 7.1, 7.2 8.2, 8.3	Further updates in view of the reviewers comments, and providing more details regarding the fit procedure and the processing chain
0.9.0	2013-11-27	—	Release to ESA and external reviewers
0.9.1	2014-03-17	4.	Instrument overview section now in separate document; section numbering of this document unchanged to maintain change record
0.9.2	2014-04-07	6.2	Some small typographic corrections and updates
0.10.0	2014-04-15	—	Release to ESA
0.10.1	2014-09-19	6.1–6.6 7.1–7.4	Minor updates and corrections in text and tables; old Sects. 6.5 and 6.7 combined; Sects. 6.6 updated; references updated. Descriptions updated and tables of input and output data added Notation of variables improved or clarified in view of the IODD [RD1]
0.10.2	2014-09-25	6.6	Table added with overview user applications and data the users need
0.11.0	2014-10-02	—	Release to ESA
0.11.1	2015-08-27	6.4.1 6.4.4.1 6.6, 7.4	Update of AMF look-up table entries Update text regarding using cloud fraction from NO_2 spectral window Minor updates in product data set tables, incl. dataset units
0.13.0	2015-09-14	—	Limited release to S5P Validation Team
0.13.1	2015-12-08	6.2, 7.5 7.1	Minor textual corrections Correction of units of input datasets
0.14.0	2015-12-11	—	Release to ESA
0.14.1	2016-01-21	6.4.2 6.4.6	Temperature correction equation updated Description of de-striping implementation clarified

[*continues on next page*]

Document change record – *continued*

issue	date	item	comments
1.0.0	2016-02-05	—	Public release
1.0.1	2017-01-31	All	Corrections and additions in response to internal review comments
1.0.2	2017-06-13	A – D	Appendices added
1.0.3	2017-07-13	All	Finalising the corrections and additions
1.1.0	2017-08-16	—	Updated public release for commissioning phase (E1)
1.1.1	2018-02-02	6.2	Formulation of the Ring term to match operational implementation
		6.2	Improved description of the wavelength calibration
		6.2.3	New section with text from main section to improve readability
		6.4.6	Expanded description of a possible de-striping algorithm
		7.4	Updated detailed product overview table to match output product
1.1.2	2018-05-31	6.2	Updated to match the operational implementation
		C, D	Updated to match the operational implementation
		E	Appendix on the `qa_value` definition added
1.1.3	2018-06-08	5 – 9	Many textual corrections and improvements to match the operational implementation and to incorporate results based on the TROPOMI measurements from the commissioning phase
1.2.0	2018-06-11	—	Release for operational phase (E2) *processor version 1.0.0*
1.2.1	2018-10-15	—	Version with main text changes v1.1.0 to v1.2.0 marked for reviewers
1.2.2	2018-11-08	—	Figures 1, 3, 5, 8, 28 redone using TROPOMI data
		5.4	Text and Table updated
		5.6	Text updated and Table 2 added
		6.3.1	Text on updates in TM5-MP and Figure 9 added
		6.4.6	Text on de-striping expanded and Figure 21 added
		6.6	Improved treatment of snow/ice cases described and Figure 25 added
		7.4	Tables 12 and 13 updated to include stripe amplitude
		8.2	Text updated and superfluous figure removed
		E	Updated `qa_value` for treatment of snow/ice cases (cf. Sect. 6.6)
		—	Further textual updates
1.3.0	2018-11-08	—	Release *processor version 1.2.0*
1.3.1	2019-01-31	6.4.4.1	Text on treatment of cloud data improved; Figure 10 added
		6.6	Product overview Table 5 and product usage Table 6 updated
		7.4	Detailed product overview Table 11 updated
		E	Updated `qa_value` for $M^{\text{trop}}/M^{\text{geo}}$ threshold
		—	Further minor textual updates and corrections
1.4.0	2019-02-06	—	Release *processor version 1.3.0*
1.4.1	2019-04-15	6.2 & F	Added description of removal of outliers from the DOAS fit residual
		C	Description on limiting cloud fraction to $[0:1]$ added
		E	Updated `qa_value` for `solar_eclipse`
1.4.2	2019-10-02	—	Remarks and suggestions from A. Richter & S. Beirle addressed
1.4.3	2019-10-03	6.2	Section structure modified to improve readability
		9	Section on Validation restructured
		—	Further textual updates and corrections
1.5.0	2019-10-03	—	Release to ESA for review
2.0.0	—	—	Not released: no processor update implemented

[*continues on next page*]

Document change record – *continued*

issue	date	item	comments
2.0.1	2020-02-19	—	Textual updates in view of processor version changes
		6.4.4	Usage of ECMWF snow/ice flag & impact of FRESCO update
2.0.2	2020-03-10	—	Textual updates addressing remarks from ESA on v1.5.0
2.0.3	2021-01-21	—	Minor updates and corrections & digital signatures (page 2) removed
2.0.4	2021-02-24	5.1	General NO_2 description expanded
		5.6	Version history expanded, including note on data change
		6.4	Several subsections finetuned and expanded
		6.4.4	Subsection on the FRESCO-wide update added
		6.6	Product description and usage updated
		7.1–4	Feasibility expanded and updated where needed
		9.1–4	Vaidation discussion updated where needed
2.1.0	2021-02-24	—	Release to ESA for review
2.1.1	2021-04-15	All	Minor updates after review and other textual improvements
		6.4.4	Section on cloud data reorganised and somewhat extended
2.1.2	2021-04-20	9.1–4	Validation sections reorganised and shortend
2.1.3	2021-06-15	—	Details finalised
2.2.0	2021-06-16	—	Release *processor versions 1.4.0 & 2.2.0*
2.2.1	2022-01-27	All	Minor updates and textual corrections
2.2.2	2022-06-08	6.4.4.2	Description of new TROPOMI DLER v1 surface albedo usage in the
		6.4.5	FRESCO cloud and NO_2 data retrieval
2.4.0	2022-07-11	—	Release *processor versions 2.4.0*
2.4.1	2023-08-23	5.6	Product version table expanded; old version info move to App. G
		6.2	Short note added on treatment of spectral pixels that are flagged
		6.4 & 6.6	Geometric column added to the data product (as of processor v2.6.0)
2.4.2	2024-03-18	E	Updates of the `qa_value` rules: 2. sun_glint only over water;
			5b. was missing; 12. pressure criterion adjusted
2.4.3	2024-04-03	6.4	Added that negative tropospheric columns are physically sensible
		6.4.3	Harmonisation of cloudy, clear and TOA subscripts
		6.4.5.2	Limiting cloud fraction to $[0, 1]$ limits cloud radiance fraction similarly
		6.4.10	Added note about first stripe amplitude value and missing data
		7.1	Reference to new DEM given
		F	Outliers remaining after a removal round may cause unreliable results
2.4.4	2024-04-04	6.4.5.2	Improved surface albedo climatology DLER v2.1 and its usage in
		6.4.6, D	snow/ice cases added
2.4.5	2024-04-10	6.2.3	Description of background and usage of the Wald-Wolfowitz runs test
2.4.6	2024-04-10	5.6	Overview of the v2.7.1 updates
		E	Adjustment of the `qa_value` for descending pixels added
2.4.7	2024-05-22	6.4.5.2	Impact of new DLER v2.1 described
		—	Minor textual improvements
		—	Release to ESA for evaluation
2.7.0	2024-07-18	—	Release *processor version 2.7.1*

[*continues on next page*]

Document change record – *continued*

issue	date	item	comments
2.7.5	2024-10-24	6.2	Selected wavelength bands can be excluded from the DOAS fit
		6.2.3	Mention how the runs test treats flagged or excluded spectral pixels
		6.4.4.2	Improvements in FRESCO-S: two-band retrieval
		7.1	Pixel surface elevation is now dynamic instead of static input
		E	Adjustment of scene pressure limit in `qa_value` rule 12
2.7.6	2024-11-06	5.6	Some outdated text removed; one graph moved to App. E
		6.4.4.2	Text & figures on impact of DLER instead of LER shortend and moved
		6.4.5.2	from 6.4.4.2 to 6.4.5.2
2.7.7	2024-11-07	—	Version finalised & released to ESA for evaluation
2.8.0	2024-11-18	—	Release *processor version 2.8.0*
2.8.1	2025-10-14	6.2.4	New section describing a change in the DOAS NO_2 slant column fit
2.9.0	2025-10-27	—	Release *processor version 2.9.1*

Contents

List of Tables

List of Figures

1 Introduction to the document

1.1 Identification

This document, identified as S5P-KNMI-L2-0005-RP, is the Algorithm Theoretical Basis Document (ATBD) for the TROPOMI total and tropospheric NO_2 data products. It is part of a series of ATBDs describing the TROPOMI Level-2 data products. The latest public release version of the ATBD is available via [ER1].

This ATBD describes NO_2 processor version 2.9.1 and changes to the processor up to this version.

The OFFL and RPRO data product has the following DOI: 10.5270/S5P-9bnp8q8

An overview of which NO_2 processor version is used for processing which TROPOMI orbits is given in Table 2.

Additional documents related to the TROPOMI NO_2 data products:

- Product User Manual (PUM), identified as S5P-KNMI-L2-0021-MA, available via [ER2].
- Product ReadMe File (PRF), identified as S5P-MPC-KNMI-PRF-NO2, available via [ER3].
- Product User Manual (PUM) for the TM5 NO_2, SO_2 and HCHO profile auxiliary support product, identified as S5P-KNMI-L2-0035-MA, available via [ER2].
- Quarterly Validation Report (ROCVR), identified as S5P-MPC-IASB-ROCVR, available via [ER4].

S5P/TROPOMI product and algorithm documents are also available via [ER5].

1.2 Purpose and objective

The purpose of this document is to describe the theoretical basis and the implementation of the NO_2 Level-2 algorithm for TROPOMI. The document is maintained during the development phase and the lifetime of the data products. Updates and new versions will be issued in case of changes of the algorithm.

1.3 Document overview

Sections 2 and 3 list the applicable and reference documents and the terms and abbriviations specific for this document; references to peer-reviewed papers and other scientific publications are listed in App. H. Section 4 provides a reference to a general description of the TROPOMI instrument, which is common to all ATBDs of the TROPOMI Level-2 data products. Section 5 provides an introduction to the NO_2 data products, their heritage, the set-up of their retrieval, the requirements of the products, and their availability. Section 6 gives an overview of the TROPOMI NO_2 data processing system and important aspects of the various steps in the processing. Section 7 lists some aspects regarding the feasibility of the NO_2 data products, such as the computational effort and the auxiliary information needed for the processing. Section 8 deals with an error analysis of the NO_2 data product. Section 9 gives a brief overview of validation issues and possibilities, such as campaigns and satellite intercomparions. Section 10 formulates some conclusion regarding the NO_2 data products.

1.4 Acknowledgements

The authors would like to thank the following people for useful discussions, information, reviews of earlier versions of this document and other contributions: Andreas Hilboll, Andreas Richter, Angelika Dehn, Bram Maasakkers, Bram Sanders, Deborah Stein – Zweers, Dominique Brunner, Huan Yu, Isabelle De Smedt, Isolde Glissenaar, Jason Williams Johan de Haan, Lidia Saavedra De Miguel, Maarten Sneep, Marina Zara, Mark ter Linden, Michel Van Roozendael, Piet Stammes, Pieter Valks, Ronald van der A, Steffen Beirle, Thomas Wagner.

2 Applicable and reference documents

2.1 Applicable documents

[AD1] Level 2 Processor Development – Statement of Work.
source: ESA/ESTEC; **ref:** S5P-SW-ESA-GS-053; **issue:** 1.1; **date:** 2012-05-21.

[AD2] GMES Sentinel-5 Precursor – S5p System Requirement Document (SRD).
source: ESA/ESTEC; **ref:** S5p-RS-ESA-SY-0002; **issue:** 4.1; **date:** 2011-04-xx.

2.2 Standard documents

There are no standard documents

2.3 Reference documents

[RD1] Sentinel 5 precursor/TROPOMI KNMI and SRON level 2 Input Output Data Definition.
source: KNMI; **ref:** S5P-KNMI-L2-0009-SD; **issue:** 21.0.0; **date:** 2025-10-01.

[RD2] Terms, definitions and abbreviations for TROPOMI L01b data processor.
source: KNMI; **ref:** S5P-KNMI-L01B-0004-LI; **issue:** 3.0.0; **date:** 2013-11-08.

[RD3] Terms and symbols in the TROPOMI Algorithm Team.
source: KNMI; **ref:** S5P-KNMI-L2-0049-MA; **issue:** 2.0.0; **date:** 2016-05-17.

[RD4] TROPOMI Instrument and Performance Overview.
source: KNMI; **ref:** S5P-KNMI-L2-0010-RP; **issue:** 0.10.0; **date:** 2014-03-15.

[RD5] GMES Sentinels 4 and 5 Mission Requirements Document.
source: ESA/ESTEC; **ref:** EOP-SMA/1507/JL-dr; **issue:** 3; **date:** 2011-09-21.

[RD6] QA4ECV - Quality Assurance for Essential Climate Variables.
source: KNMI; **ref:** EU-project 607405, SPA.2013.1.1-03; **date:** November 2012.

[RD7] Science Requirements Document for TROPOMI. Volume I: Mission and Science Objectives and Observational Requirements.
source: KNMI, SRON; **ref:** RS-TROPOMI-KNMI-017; **issue:** 2.0.0; **date:** 2008-10-30.

[RD8] CAPACITY: Operational Atmospheric Chemistry Monitoring Missions – Final report and technical notes of the ESA study.
source: KNMI; **ref:** CAPACITY; **date:** Oct. 2005.

[RD9] CAMELOT: Observation Techniques and Mission Concepts for Atmospheric Chemistry – Final report of the ESA study.
source: KNMI; **ref:** RP-CAM-KNMI-050; **date:** Nov. 2009.

[RD10] TRAQ: Performance Analysis and Requirements Consolidation – Final report of the ESA study.
source: KNMI; **ref:** RP-ONTRAQ-KNMI-051; **date:** Jan. 2010.

[RD11] Sentinel-5P Calibration and Validation Plan for the Operational Phase.
source: ESA; **ref:** ESA-EOPG-CSCOP-PL-0073; **issue:** 1; **date:** 2017-11-6.

[RD12] Algorithm theoretical basis document for the TROPOMI L01b data processor.
source: KNMI; **ref:** S5P-KNMI-L01B-0009-SD; **issue:** 11.0.0; **date:** 2025-10-01.

[RD13] NO2 PGE Detailed Processing Model.
source: Space Sytems Finland; **ref:** TN-NO2-0200-SSF-001; **issue:** 1.2; **date:** 2010-04-21.

[RD14] S5P/TROPOMI Static input for Level 2 processors.
source: KNMI/SRON/BIRA/DLR; **ref:** S5P-KNMI-L2CO-0004-SD; **issue:** 4.0.0; **date:** 2016-03-21.

[RD15] QA4ECV D4.2 - Recommendations on best practices for retrievals for Land and Atmosphere ECVs..
source: KNMI; **ref:** EU-project 607405, SPA.2013.1.1-03; **date:** April 2016.

[RD16] An improved temperature correction for OMI NO_2 slant column densities from the 405-465 nm fitting window.
source: KNMI; **ref:** TN-OMIE-KNMI-982; **issue:** 1.0; **date:** 2017-01-24.

[RD17] Cloud retrieval algorithm for GOME-2: FRESCO+.
source: EUMETSAT/KNMI; **ref:** EUM/CO/09/4600000655/RM; **issue:** 1.3; **date:** 2010-10-18.

[RD18] Sentinel-5 L2 Prototype Processor – Algorithm Theoretical Baseline Document for Cloud data product.
source: KNMI; **ref:** KNMI-ESA-S5L2PP-ATBD-005; **issue:** 3.1; **date:** 2019-05-02.

[RD19] S5P/TROPOMI ATBD Cloud Products.
source: DLR; **ref:** S5P-DLR-L2-ATBD-400I; **issue:** 2.6.1; **date:** 2023-11-10.

[RD20] TROPOMI ATBD of the directionally dependent surface Lambertian-equivalent reflectivity.
source: KNMI; **ref:** S5P-KNMI-L3-0301-RP; **issue:** 1.2.0; **date:** 2022-01-13.

[RD21] TROPOMI ATBD of the directionally dependent surface Lambertian-equivalent reflectivity.
source: KNMI; **ref:** S5P-KNMI-L3-0301-RP; **issue:** 2.1.0; **date:** 2023-09-04.

[RD22] Dutch OMI NO_2 (DOMINO) data product v2.0 – see URL `https://www.temis.nl/airpollution/no2.php`.
source: KNMI; **ref:** OMI_NO2_HE5_2.0_2011; **date:** 18 August 2011.

[RD23] Product user manual for the TM5 NO_2, SO_2 and HCHO profile auxiliary support product.
source: KNMI; **ref:** S5P-KNMI-L2-0035-MA; **issue:** 1.0.0; **date:** 2021-02-04.

[RD24] Preparing elevation data for Sentinel 5 precursor.
source: KNMI; **ref:** S5P-KNMI-L2-0121-TN; **issue:** 2.0.0; **date:** 2015-09-11.

[RD25] S5P/TROPOMI Science Verification Report.
source: IUP; **ref:** S5P-IUP-L2-ScVR-RP; **issue:** 2.1; **date:** 2015-12-22.

[RD26] Wavelength calibration in the Sentinel-5 precursor Level 2 data processors.
source: KNMI; **ref:** S5P-KNMI-L2-0126-TN; **issue:** 1.0.0; **date:** 2015-09-11.

[RD27] Determine the effective cloud fraction for a specific wavelength.
source: KNMI; **ref:** S5P-KNMI-L2-0115-TN; **issue:** 2.0.0; **date:** 2019-04-10.

[RD28] TROPOMI PUM of the directionally dependent surface Lambertian-equivalent reflectivity.
source: KNMI; **ref:** S5P-KNMI-L3-0302-MA; **issue:** 2.1.0; **date:** 2023-09-04.

2.4 Electronic references

[ER1] TROPOMI level-2 product ATBD documents. URL `https://sentiwiki.copernicus.eu/web/s5p-products`.

[ER2] TROPOMI level-2 product PUM documents. URL `https://sentiwiki.copernicus.eu/web/s5p-products`.

[ER3] TROPOMI level-2 product PRF documents. URL `https://sentiwiki.copernicus.eu/web/s5p-products`.

[ER4] TROPOMI Quarterly Validation Report. URL `https://mpc-vdaf-server.tropomi.eu/`.

[ER5] Sentinel-5P TROPOMI Products and algorithms documentation. URL `https://sentiwiki.copernicus.eu/web/s5p-products`.

[ER6] TEMIS website: NO2 data product page. URL `https://www.temis.nl/airpollution/no2.php`.

[ER7] QA4ECV website. URL `http://www.qa4ecv.eu/`.

[ER8] QA4ECV NO2 ECV precursor data. URL `http://www.qa4ecv.eu/ecv/no2-pre`.

[ER9] Copernicus DEM - Global and European Digital Elevation Model. doi:10.5270/ESA-c5d3d65. URL https://spacedata.copernicus.eu/collections/copernicus-digital-elevation-model.

[ER10] Copernicus Data Space Ecosystem. URL https://dataspace.copernicus.eu/.

[ER11] TROPOMI website. URL http://www.tropomi.eu/.

[ER12] Wald-Wolfowitz runs test. URL https://en.wikipedia.org/wiki/Wald-Wolfowitz_runs_test.

[ER13] S5P/TROPOMI ISRF. URL http://www.tropomi.eu/data-products/isrf-dataset.

[ER14] Vandaele et al. NO2 cross sections. URL http://spectrolab.aeronomie.be/no2.htm.

[ER15] TM5 website. URL http://www.projects.science.uu.nl/tm5/.

[ER16] Q. L. Kleipool, M. R. Dobber, J. F. De Haan et al.; OMI Surface Reflectance Climatology (2010). URL https://disc.gsfc.nasa.gov/datasets?page=1&source=AURA~OMI.

[ER17] TROPOMI surface LER & DLER database. URL https://www.temis.nl/surface/albedo/tropomi_ler.php.

[ER18] S5P-PAL reprocessing: NO2 dataset. URL https://data-portal.s5p-pal.com/products/no2.html.

[ER19] M. J. Brodzik and J. S. Stewart; Near Real-Time SSM/I EASE–Grid Daily Global Ice Concentration and Snow Extent. Boulder, Colorado USA. NASA National Snow and Ice Data Center (2016); 10.5067/3KB2JPLFPK3R. Updated daily; URL http://nsidc.org/data/NISE.

[ER20] EUMETSAT Ocean & Sea Ice Satellite Application Facility. Updated daily; URL http://osisaf.met.no/.

[ER21] TROPOMI Mission Performance Centre. URL http://www.tropomi.eu/data-products/mission-performance-centre.

[ER22] Sentinel-5P MPC validation server. URL https://mpc-vdaf-server.tropomi.eu/.

[ER23] In-service Aircraft for a Global Observing System (IAGOS). URL https://www.iagos.org/.

[ER24] What are outliers in the data? URL https://www.itl.nist.gov/div898/handbook/prc/section1/prc16.htm.

[ER25] Important z-scores. URL http://www.cs.uni.edu/~campbell/stat/normfact.html.

[ER26] The Standard Normal Distribution. URL http://sphweb.bumc.bu.edu/otlt/MPH-Modules/BS/BS704_Probability/BS704_Probability9.html.

3 Terms, definitions and abbreviated terms

Terms, definitions and abbreviated terms that are used in development program for the TROPOMI L0-1b data processor are described in [RD2]. Terms, definitions and abbreviated terms that are used in development program for the TROPOMI L2 data processors are described in [RD3]. Terms, definitions and abbreviated terms that are specific for this document can be found below.

3.1 Terms and definitions

The most important symbols related to the data product described in this document – some of which are not in [RD3] – are the following; see also the data product overview list in Table 12.

M	total air-mass factor
M_{cld}	cloudy air-mass factor
M_{clr}	clear-sky air-mass factor
M^{trop}	tropospheric air-mass factor
M^{strat}	stratospheric air-mass factor
N_{s}	total slant column density
$N_{\mathrm{s}}^{\mathrm{trop}}$	tropospheric slant column density
$N_{\mathrm{s}}^{\mathrm{strat}}$	stratospheric slant column density
$N_{\mathrm{v}}^{\mathrm{geo}}$	geometric column density
N_{v}	total vertical column density
$N_{\mathrm{v}}^{\mathrm{trop}}$	tropospheric vertical column density
$N_{\mathrm{v}}^{\mathrm{strat}}$	stratospheric vertical column density
$N_{\mathrm{v}}^{\mathrm{sum}}$	sum of tropospheric and stratospheric vertical column density

3.2 Acronyms and abbreviations

AAI	Absorbing Aerosol Index
ACE	Atmospheric Chemistry Experiment
AMF	Air-mass factor
CAMS	Copernicus Atmosphere Monitoring Service
CTM	Chemistry Transport Model
DAK	Doubling-Adding KNMI
DLER	Directionally dependent Lambertian equivalent reflectivity
DEM	Digital Elevation Map
DOAS	Differential Optical Absorption Spectroscopy
DOMINO	Dutch OMI NO_2 data products of KNMI for OMI
ECMWF	European Centre for Medium-Range Weather Forecast
ENVISAT	Environmental Satellite
EOS-Aura	Earth Observing System (Chemistry & Climate Mission)
ERBS	Earth Radiation Budget Satellite
ERS	European Remote Sensing satellite
FRESCO	Fast Retrieval Scheme for Clouds from the Oxygen A band
GOME	Global Ozone Monitoring Experiment
HALOE	Halogen Occultation Experiment
IDAF-L2	Instrument Data Analysis Facility, Level 2 (at KNMI)
IPA	Independent pixel approximation
ISRF	Instrument Spectral Response Function (*aka* slit funtion)

LER	Lambertian equivalent reflectivity
LUT	Look-up table
MAX-DOAS	Multi-axis DOAS
MERIS	Medium Resolution Imaging Spectrometer
MetOp	Meteorological Operational Satellite
MPC	S5P Mission Performance Centre
NISE	Near-real time Ice and Snow Extent
NRT	near-real time (i.e. processing within 3 hours of measurement)
OMI	Ozone Monitoring Instrument
OMNO2A	OMI NO2 slant column data product (at NASA)
OSIRIS	Optical Spectrograph and Infrared Imager System
OSISAF	Ocean & Sea Ice Satellite Application Facility
PANDORA	not an acronym; direct-sun UV-visible spectrometer
PDGS	Sentinel-5Precursor Payload Data Ground Segment (at DLR)
POAM	Polar Ozone and Aerosol Measurements
PRF	Product ReadMe File
PUM	Product User Manual
ROCVR	Routine Operations Consolidated Validation Report
QA4ECV	European "Quality Assurance for Essential Climate Variables" project
S5P	Sentinel-5 Precursor (satellite carrying TROPOMI)
SAGE	Stratospheric Gas and Aerosol Experiment
SAOZ	Systeme d'Analyse par Observations Zenithales instrument
SCIAMACHY	Scanning Imaging Absorption Spectrometer for Atmospheric Cartography
SME	Solar Mesosphere Explorer
SNR	Signal-to-Noise Ratio
SPOT	Système Pour l'Observation la Terre
STREAM	STRatospheric Estimation Algorithm from Mainz
TM4, TM5	Data assimilation / chemistry transport model (version 4 or 5)
TM4NO2A	NO_2 data products of KNMI for GOME, SCIAMACHY and GOME-2
TOA	Top-of-atmosphere
TROPOMI	Tropospheric Monitoring Instrument
UARS	Upper Atmosphere Research Satellite
VDAF	Validation Facility of the MPC

4 TROPOMI instrument description

A description of the TROPOMI instrument and performance, referred to from all ATBDs, can be found in [RD4]. See also the overview paper of Veefkind et al. [2012].

5 Introduction to the TROPOMI NO_2 data products

5.1 Nitrogen dioxide in troposphere and stratosphere

Nitrogen dioxide (NO_2) and nitrogen oxide (NO) – together usually referred to as nitrogen oxides (NO_x = NO + NO_2) – are important trace gases in the Earth's atmosphere, present in both the troposphere and the stratosphere. They enter the atmosphere as a result of anthropogenic activities (notably fossil fuel combustion and biomass burning) and natural processes (such as microbiological processes in soils, wildfires and lightning). Approximately 95% of the NO_x emissions is in the form of NO. During daytime, i.e. in the presence of sunlight, a photochemical cycle involving ozone (O_3) converts NO into NO_2 (and vice versa) on a timescale of minutes, so that NO_2 is a robust measure for concentrations of nitrogen oxides (Solomon [1999], Jacob [1999]).

In the troposphere NO_2 plays a key role in air quality issues, as it directly affects human health [World Health Organisation, 2003]. In addition nitrogen oxides are essential precursors for the formation of ozone in the troposphere (e.g. Sillman et al. [1990]) and they influence concentrations of OH and thereby (shorten) the lifetime of methane (CH_4) (e.g. Fuglestvedt et al. [1999]). Although NO_2 is a minor greenhouse gas in itself, the indirect effects of NO_2 on global climate change are probably larger, with a presumed net cooling effect mostly driven by a growth in aerosol concentrations through nitrate formation from nitrogen oxides and enhanced levels of oxidants (e.g. Shindell et al. [2009]). Deposition of nitrogen is of great importance for eutrification [Dentener et al., 2006], the response of the ecosystem to the addition of substances such as nitrates and phosphates – negative environmental effects include the depletion of oxygen in the water, which induces reductions in fish and other animal populations.

For typical levels of OH the lifetime of NO_x in the lower troposphere is less than a day. For Riyadh, for example, Beirle et al. [2011] find a lifetime of about 4.0 ± 0.4 hours, while at higher latitudes (e.g. Moscow) the lifetime can be considerably longer, up to 8 hour in winter, because of a slower photochemistry in that season. For Switzerland Schaub et al. [2007] report lifetimes of 3.6 ± 0.8 hours in summer and $13.1 \pm (3.8)$ hours in winter. With lifetimes in the troposphere of only a few hours, the NO_2 will remain relatively close to its source, making the NO_x sources well detectable from space. As an example, Fig. 1 shows distinct hotspots of NO_2 pollution over the highly industrialised and urbanised regions of London, Rotterdam and the Ruhr area in the monthly average tropospheric NO_2 for April 2018 over Europe derived from TROPOMI data.

Since July 2018, with the first public release of the TROPOMI datasets including NO_2, the number of TROPOMI users and publications has grown strongly. A review of these applications is beyond the scope of this ATBD. Topics addressed range from changes in global-scale NO_2 distributions and impacts on atmospheric

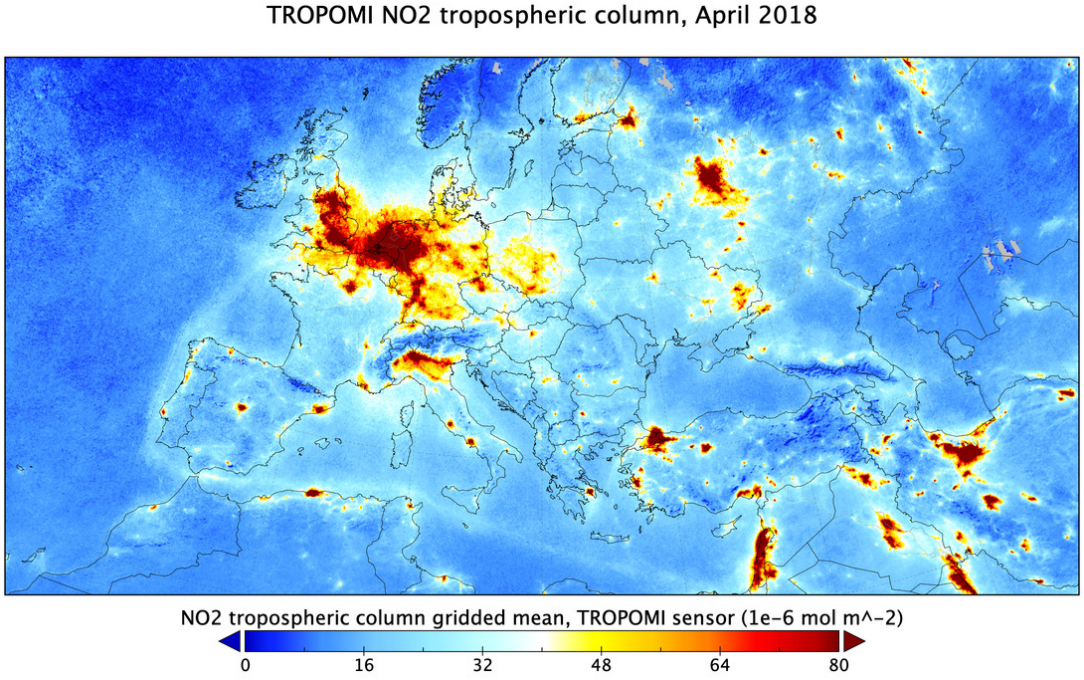

Figure 1: Monthly average distribution of tropospheric NO_2 columns for April 2018 over Europe based on TROPOMI data, derived with processor version 1.2.0.

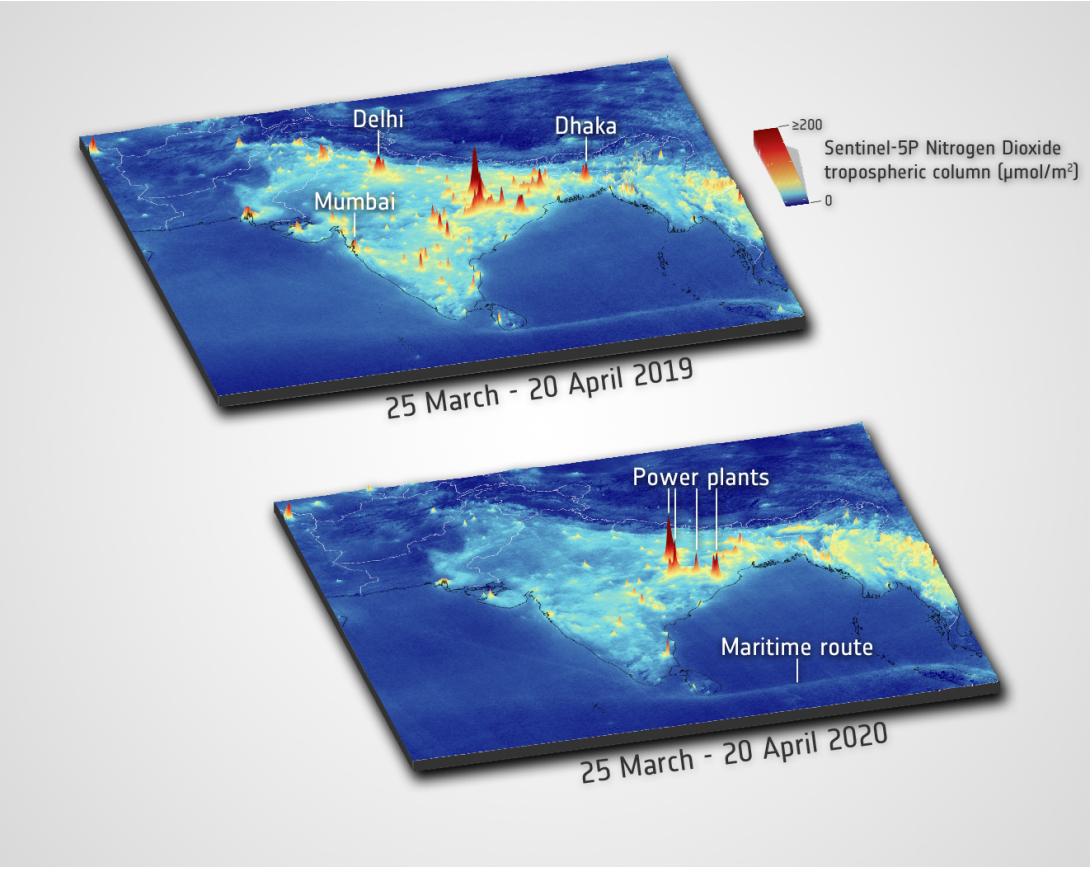

Figure 2: Strong reduction of NO_2 over India as a result of the COVID-19 lockdown in March-April 2020 (lower panel) compared to 2019 (top panel). Concentrations were reduced strongly in cities like Delhi, Mumbai, Dhaka. In contrast, some of the coal-fired power plants continued the electricity production with only minor reductions. Source: `https://www.esa.int/`, news story 24 April 2020.

chemistry, data assimilation applications, validation of regional air quality models and NOx emission inversion studies. In particular the combination of the high spatial resolution, the large signal-to-noise ratio and daily global coverage makes TROPOMI unique. This has been and will be further used for the analysis of emissions and concentrations at the local scale, for individual cities, power plants, industrial complexes, road traffic and shipping lanes. The power of TROPOMI is nicely demonstrated by the observation of pollution plumes from individual ships [Georgoulias et al., 2020].

In 2020 the number of publications and attention in the media for TROPOMI NO_2 observations has exploded. As a result of the COVID-19 related lockdowns pollution levels have dropped dramatically as observed in real-time by the TROPOMI instrument, largely consistent with surface observations [Gkatzelis et al., 2021]. This clearly demonstrates the value of real-time global monitoring of concentrations from space. Fig. 2 shows, as example, COVID-19 lockdown impact on NO_2 in India.

In the stratosphere NO_2 is involved in some photochemical reactions with ozone and thus affects the ozone layer (Crutzen [1970]; Seinfeld and Pandis [2006]). NO_2 in the stratosphere originates mainly from oxidation of N_2O in the middle stratosphere, which leads to NO_x, which in turn acts as a catalyst for ozone destruction (Crutzen [1970]; Hendrick et al. [2012]). But NO_x can also suppress ozone depletion by converting reactive chlorine and hydrogen compounds into unreactive reservoir species (such as $ClONO_2$ and HNO_3; Murphy et al. [1993]).

Fig. 3 shows, as an example, the stratospheric NO_2 distribution derived from TROPOMI measurements on 1 April 2018 at the 13:30 overpass local time. The image shows variability related to atmospheric transport and diurnal variability in the stratosphere. In a study into the record ozone loss, triggered by enhanced NO_x levels, in the exceptionally strong Arctic polar vortex in Spring 2011, Adams et al. [2013] showed the usefulness of such data when investigating the anomalous dynamics and chemistry in the stratosphere. With its high spatial resolution and signal-to-noise ratio, TROPOMI is clearly well-suited to help understand the stratospheric NO_2 content and its implications for the ozone distribution.

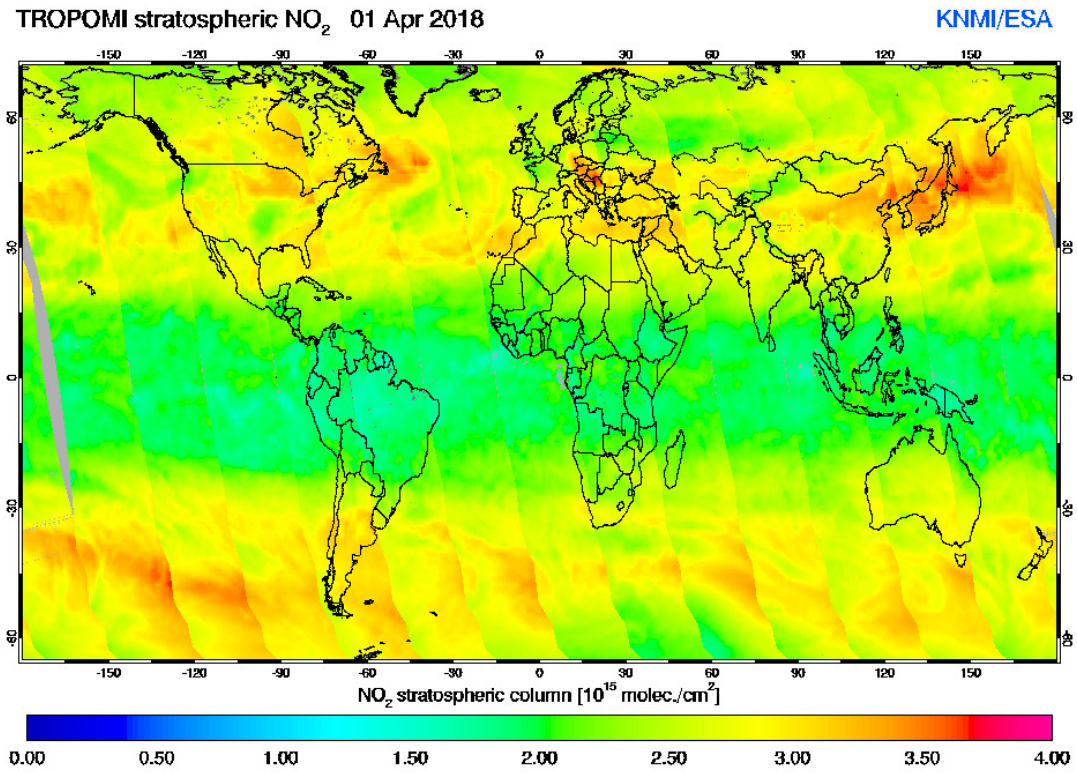

Figure 3: Distribution of stratospheric NO_2 on 1 April 2018 along the individual TROPOMI orbits, derived with processor version 1.2.0. The image shows that atmospheric dynamics creates variability in the stratospheric columns, mainly at mid-latitudes. Furthermore we can see the effect of the increase of NO_2 in the stratosphere during daytime leading to small jumps from one orbit to the next. Note that the colour scale range is different from the range in Fig. 1.

From observed trends in N_2O emissions one would expect a trend in stratospheric NO_2 with potential implications for persistent ozone depletion well into the 21st century [Ravishankara et al., 2009]. There have been some reports of such trends in stratospheric NO_2, for instance from New Zealand [Liley et al., 2000] and northern Russia [Gruzdev and Elokhov, 2009]. On the other hand, Hendrick et al. [2012] report that changes in the NO_x partitioning in favour of NO may well conceal the effect of trends in N_2O. TROPOMI continues the important record of stratospheric NO_2 observations that started with GOME in 1995, and improves the detectability of trends.

Over unpolluted regions most NO_2 is located in the stratosphere (typically more than 90%). For polluted regions 50–90% of the NO_2 is located in the troposphere, depending on the degree of pollution. Over polluted regions, most of the tropospheric NO_2 is found in the planetary boundary layer, as has been shown among others in campaigns using measurements made from aeroplanes, such as INTEX (e.g. Hains et al. [2010]). In areas with strong convection, enhanced NO_2 concentrations are observed at higher altitudes due to production of NO_x by lightning (e.g. Ott et al. [2010]; Allen et al. [2021]).

The important role of NO_2 in both troposphere and stratosphere implies that it is not only important to know the total column density of NO_2, but rather the tropospheric NO_2 and stratospheric NO_2 concentrations separately. A proper separation between the two is therefore important, in particular for areas with low pollution, where the stratospheric concentration forms a significant part of the total column.

5.2 NO_2 satellite retrieval heritage

Tropospheric concentrations of NO_2 are monitored all over the world by a variety of remote sensing instruments – ground-based, in-situ (balloon, aircraft) or satellite-based – each with its own specific advantages, and to some extent still under development.

Stratospheric NO_2 has been measured by a number of satellite instruments since the 1980s, such as the spectrometer aboard SME (1981-1989; Mount et al. [1984]), SAGE-II/III (ERBS/Meteor-3M, 1984-2005;

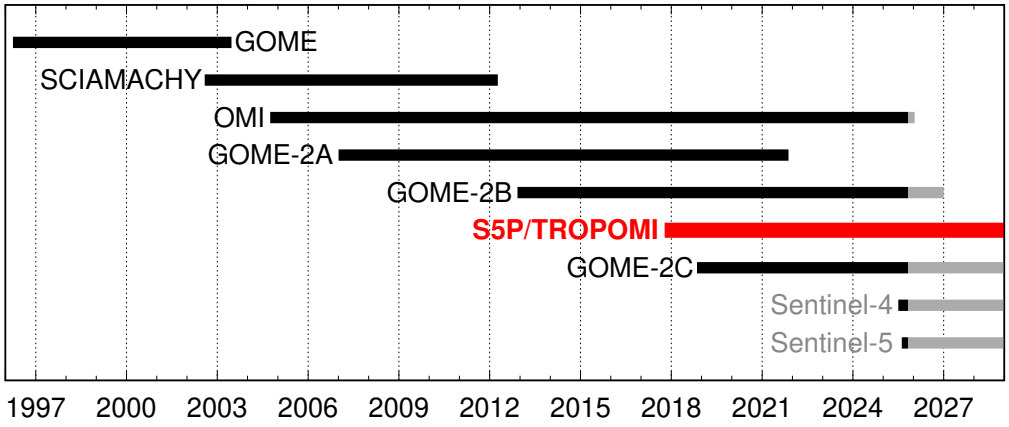

Figure 4: Overview of the European UV/Vis polar orbiting and geostationary backscatter satellite instruments capable of retrieving tropospheric and stratospheric NO_2 column data since the launch of GOME aboard ERS-2, including missions to be launched in the near future.

Chu and McCornick [1986]), HALOE (UARS, 1991-2005; Gordley et al. [1996]), POAM (SPOT-3, 1993-1996; Randall et al. [1998]), SCIAMACHY (ENVISAT, 2002–2012; Bovensmann et al. [1999], Sierk et al. [2006]), OSIRIS (Odin, 2001–present; Llewellyn et al. [2004], Adams et al. [2016]), and ACE (SCISAT-1, 2003–present; Bernath et al. [2005]).

Over the past 22 years tropospheric NO_2 has been measured from UV/Vis backscatter satellite instruments such as GOME (ERS-2, 1995–2011; Burrows et al. [1999]), SCIAMACHY (ENVISAT, 2002–2012; Bovensmann et al. [1999]), OMI (EOS-Aura, 2004–present; Levelt et al. [2006]), the GOME-2 instruments [Munro et al., 2006] aboard MetOp-A (2007–2021), MetOp-B (2012–present) and MetOp-C (2019–present), the OMPS instrument [Yang et al., 2014] on the Suomi NPP platform (2011–present) and the NOAA-20 satellite (2017–present). TROPOMI (see [RD4]; Veefkind et al. [2012]) extends the records of these observations, and in turn will be followed up by several forthcoming instruments including Sentinel 5 and the geostationary platforms GEMS (Bak [2013], Kim [2020]; launched in 2020), TEMPO [Zoogman et al., 2017] and Sentinel 4 [Ingmann et al., 2012], [RD5]. Fig. 4 shows the timelines of the NO_2 data records of some of these instruments. Note that TROPOMI, OMI, the GOME-2 instruments and Sentinel-5 provide (near-)global coverage in one day, and that Sentinel-4 is a geostationary instrument.

For the UV/Vis backscatter instruments that observe NO_2 down into the troposphere, KNMI has operated – in close collaboration with BIRA-IASB, NASA and DLR – a real-time data processing system, the results of which are freely available via the TEMIS website [ER6]. The data has been used for a variety of studies in areas like validation (see e.g. Boersma et al. [2009], Hains et al. [2010], Lamsal et al. [2010]), trends (see e.g. Van der A et al. [2008], Stavrakou et al. [2008], Dirksen et al. [2011], Castellanos and Boersma [2012], DeRuyter et al. [2012]), and NO_x emission and lifetime estimates (see e.g. Lin et al. [2010], Beirle et al. [2011], Mijling and Van der A [2012], Wang et al. [2012]).

The DOMINO approach for OMI (and the similar approach called TM4NO2A for GOME, SCIAMACHY and GOME-2) is based on a DOAS retrieval, a pre-calculated air-mass factor (AMF) look-up table and a data assimilation / chemistry transport model for the separation of the stratospheric and tropospheric contributions to the NO_2 column (see Sect. 6 for details). The differences between the processing systems for the different instruments are small and related to instrument issues, such as available spectral coverage and wavelength calibration, other absorbing trace gases fitted along, and details of the cloud cover data retrieval.

The European Quality Assurance for Essential Climate Variables (QA4ECV) project ([RD6], [ER7], Boersma et al. [2018]) has led to a homogeneous reprocessing dataset of NO_2 for the sensors GOME, SCIAMACHY, OMI and GOME-2A. This project has investigated and improved all the individual steps/modules in the NO_2 retrieval. The new NO_2 datasets are available via the QA4ECV project website at [ER8]. This new release replaces the DOMINO-v2 OMI NO_2 dataset and TM4NO2A datasets for the other sensors. Due to IT equipment issues the OMI/QA4ECV dataset ends on 29 March 2021; a follow-up dataset, based on new collection-4 OMI data, with reprocession of the full mission, is currently being set up.

The TROPOMI NO_2 processor includes many of the developments from the QA4ECV project, including improvements in the TM5-MP/DOMINO chemistry modelling-retrieval-assimilation approach, DOAS optimisations (cf. Van Geffen et al. [2020]) and air-mass factor lookup table. On top of that, several further improvements

have been implemented, notably in the TM5-MP/DOMINO system and the output data file

5.3 Separating stratospheric and tropospheric NO_2 with a data assimilation system

The NO_2 processing system starts with a DOAS retrieval step that determines the NO_2 slant column density, which represents the total amount of NO_2 along the line of sight, i.e. from sun via earth's atmosphere to satellite. To determine the tropospheric NO_2 slant column density, the stratospheric NO_2 slant column density is subtracted from the total slant column, after which the tropospheric sub-column is converted to the tropospheric vertical NO_2 column.

Several approaches to estimate the stratospheric NO_2 amount have been introduced in the past. The TM5-MP/DOMINO approach uses information from a chemistry transport model by way of data assimilation to simulate the instantaneous stratospheric NO_2 distribution and to force consistency between the stratospheric NO_2 column and the satellite measurement [Boersma et al., 2004]. Other methods applied elsewhere include the following (in arbitrary order).

a) The wave analysis method uses subsets of satellite measurements over unpolluted areas to remove known areas of pollution, i.e. areas with potentially large amounts of tropospheric NO_2, from a 24-hour composite of the satellite measured NO_2 and expands the remainder with a planetary wave analysis across the whole stratosphere, followed where necessary by a second step to mask pollution events (e.g. Bucsela et al. [2006]). This approach has been used between 2004 and 2012 for the OMI NO_2 Standard Product (SP) of NASA/KNMI.

b) The reference sector method method uses a north-to-south region over the Pacific Ocean that is assumed to be free of tropospheric NO_2, as there are no (surface) sources of NO_2, so that all NO_2 measured is assumed to be in the stratosphere (e.g. Richter and Burrows [2002], Martin et al. [2002]). This stratospheric NO_2 is then assumed to be valid in latitudinal bands for all longitudes. In some implementaions this method is extended with a spatial filtering to include other relatively clean areas across the world (e.g. Bucsela et al. [2006], Valks et al. [2011]).

c) Image processing techniques assume that the stratospheric NO_2 shows only smooth and low-amplitude latitudinal and longitudinal variations (e.g. Leue et al. [2001], Wenig et al. [2003]). This approach will probably miss the finer details in the stratospheric NO_2 distribution (as is the case for methods *a* and *b* above). The next version of NASA's OMI NO_2 SP will use a similar approach [Bucsela et al., 2013].

d) Independent stratospheric NO_2 data, such as collocated limb measurements (e.g. Beirle et al. [2010], Hilboll et al. [2013b]) or data taken from a chemistry transport model (e.g. Hilboll et al. [2013a]), can be subtracted from the total (slant) column measurements to find the tropospheric NO_2 concentrations. Unfortunately, limb collocated stratospheric measurements are not available for satellite retrievals from the GOME(-2), OMI, and TROPOMI sensors. Nevertheless this approach is potentially very useful for comparison and validation studies. Possible cross-calibration problems between the stratospheric and the total measurements would complicate the approach.

e) The STRatospheric Estimation Algorithm from Mainz (STREAM; Beirle et al. [2016]). The STREAM approach is based on the total column measurements over clean, remote regions as well as over clouded scenes where the tropospheric column is effectively shielded. STREAM is a flexible and robust interpolation algorithm and does not require input from chemical transport models. It was developed as a verification algorithm for the then upcoming satellite instrument TROPOMI, as a complement to the operational stratospheric correction based on data assimilation. STREAM was successfully applied to the UV/vis satellite instruments GOME 1/2, SCIAMACHY, and OMI. It overcomes some of the artifacts of previous algorithms, as it is capable of reproducing some of the gradients of stratospheric NO_2, e.g., related to the polar vortex, and reduces interpolation errors over continents.

f) The Standard Product 2 (SP2) includes a new stratospere-troposphere separation approach (Bucsela et al. [2013]). This approach has aspects in common with STREAM. It is based on the measurements only and uses tropospheric pollution masking and subsequent interpolation over the masked areas.

These ways of treating the stratospheric NO_2 field may not be accurate enough to capture the variability of the stratospheric NO_2 in latitudinal and longitudinal direction, as well as in time. At the same time it is not certain whether these methods do actually separate stratospheric NO_2: some of the NO_2 interpreted as "stratospheric" may be in the (upper) troposphere.

Also the assimilation approach suffers from these uncertainties, but in a different way since actual meteorological fields are used to model the dynamical and chemical variability of NO_x in the stratosphere and free troposphere. The assimilation analyses the retrieved total slant column with a strong forcing to the observations

Table 1: NO_2 data product requirements for the TROPOMI NO_2 data products, where accuraries are split in the systematic and random components. The numbers are taken from [RD11]; see also the Product ReadMe File (PRF; available via [ER3]). For convenience sake the random component is given in the same unit as in [RD11] and in the SI units used in the NO_2 data

NO_2 data product	Vertical resolution	Bias	Random
Stratospheric NO_2	Stratospheric column	$< 10\%$	0.5×10^{15} molec/cm^2 = $8.3\,\mu$mol/m^2
Tropospheric NO_2	Tropospheric column	$25-50\%$	0.7×10^{15} molec/cm^2 = $11.5\,\mu$mol/m^2

over clean regions (regions with small tropospheric column amounts). The data assimilation ensures that the model simulations of the stratospheric NO_2 column agrees closely with the satellite measurements. The modelled stratospheric NO_2 (slant column) amount is subtracted from the full column observation to derive the tropospheric column.

The use of a data assimilation system to provide stratospheric NO_2 concentrations has been shown to provide realistic results, as indicated by validation studies. For example, Hendrick et al. [2012] found very good agreement between satellite retrievals using data assimilation to estimate the stratospheric NO_2 column (GOME, SCIAMACHY and GOME-2) and ground-based measurements at the station of Jungfraujoch.

The advantages of the use of stratospheric chemistry transport modelling in combination with data assimilation are:

- The system models the chemistry (diurnal cycle) and dynamics of the stratosphere based on meteorological analyses.
- Data assimilation provides a realistic error estimate of the stratospheric NO_2 column [Dirksen et al., 2011].
- The height of the tropopause, obtained from the meteorological data, provides a point of separation of the stratospheric from the tropospheric NO_2 column.
- The result of the data assimilation is a comprehensive understanding of 3-D NO_2 distributions that covers the whole world, taking into account the spatial and temporal variability of the NO_2 profiles.

5.4 NO_2 data product requirements

S5P/TROPOMI mission requirements have been discussed in several documents, including the GMES Sentinels-4, -5 and -5Precursor Mission Requirements Document [RD5] and the Science Requirements Document for TROPOMI [RD7]. These requirements are based on the findings of the CAPACITY [RD8], CAMELOT [RD9] and TRAQ [RD10] studies. For the TROPOMI NO_2 column data products the set of requirements which are used as baseline in the routine validation work are the NO_2 data product requirement listed in Table 1; these are given in the "Sentinel-5P Calibration and Validation Plan for the Operational Phase" document [RD11] and also given in the NO_2 Product ReadMe File (PRF; available via [ER3])

The uncertainties stated in Table 1 include retrieval errors as well as instrument errors. Over polluted areas retrieval errors will dominate the uncertainties; these relate to the presence of clouds and aerosols and to the surface albedo. Over rural areas, with low NO_2 concentrations, errors in tropospheric NO_2 are mostly driven by random noise related to the instrument's Signal-to-Noise Ratio (SNR), to estimates of the stratospheric NO_2 column, and to uncertainties in the NO_2 profile.

5.5 NO_2 retrieval for TROPOMI

The TROPOMI retrieval of total and tropospheric NO_2 is based on the TM5-MP/DOMINO system (see Sect. 6.1), thus extending the long-term record of NO_2 data, produced using a reliable, well-established and well-described processing system (see Boersma et al. [2004], Boersma et al. [2007] and Boersma et al. [2011]). In particular, the inclusion of many of the retrieval developments of the QA4ECV project ([RD6], [ER7]) in the TROPOMI NO_2 retrieval will ensure a good continuity from the QA4ECV OMI and GOME-2 NO_2 records to TROPOMI. For the OMI NO_2 retrieval a number of improvements are related to spectral fitting [Van Geffen et al., 2015] and to the chemistry modelling, stratosphere-troposphere separation and the air-mass factor [Maasakkers et al., 2013]. The TROPOMI NO_2 processing chain is described in Sect. 6.5.

In order to comply with the SI unit definitions, the TROPOMI NO_2 data product file (described further in Sect. 6.6) provides the trace gas columns in mol/m^2, rather than in the commonly used unit molec/cm^2. For convenience sake, most of the text and figures of this document will remain in the latter unit or both units are given; the tables listing the input (Sect. 7.1) and output (Sect. 7.4) datasets use the SI based units.

Table 2: Overview of periods of operation of the operational NO_2 processor versions in the near-real time (NRTI) and the off-line (OFFL) data streams, as well as for officially reprocessed (RPRO) data as of the full mission reprocessing in 2022 using version 02.04.00; earlier versions are listed in App. G in Table 23 (see also the latest PRF [ER3]). Note that on 6 August 2019, as of orbit 9388, the nadir ground pixel dimensions reduced from approximately 7.0×3.5 km^2 to approximately 5.5×3.5 km^2 without a change in the processor.

Collection	Processor version	ATBD version	Data stream	In operation from		In operation until	
				orbit	date	orbit	date
03	02.04.00	2.4.0	NRTI OFFL † RPRO	24697 24655 ‡ 02832	2022-07-20 2022-07-17 ‡ 2018-05-01	28074 28030 24779 ‡	2023-03-15 2023-03-12 2022-07-25 ‡
	02.05.00	2.4.0	NRTI OFFL	28078 28031	2023-03-15 2023-03-12	31750 31704	2023-11-29 2023-11-26
	02.06.00	2.4.0	NRTI OFFL	31705 31750	2023-11-29 2023-11-26	35820 35777	2024-09-11 2024-09-08
	02.07.01	2.7.0	NRTI OFFL	35821 35778	2024-09-11 2024-09-08	36815 36756	2024-11-20 2024-11-16
	02.08.00	2.8.0	NRTI OFFL	36816 36757	2024-11-20 2024-11-16	42... 42...	2025-11-.. 2025-11-..
	02.09.01	2.9.0	NRTI OFFL	42... 42...	2025-11-.. 2025-11-..	[*current version*] [*current version*]	

† See the remark in the text regarding the switch to version 02.05.00.
‡ For the overlap period of v2.4.0 OFFL and RPRO, it is recommended to use the RPRO.

5.6 NO_2 data product: version history and access

The NO_2 processing has started directly after "first light", providing data for initial checks and validations. The near-real time (NRTI) data product is released from 4 July 2018 onwards; the reprocessed (RPRO) and off-line (OFFL) datasets contains data starting from 30 April 2018. TROPOMI NO_2 data processed in near-real time (NRT) is available within 3 hours after measurement; this data stream uses a forecast of the TM5-MP data (see next sections). A few days later, the data is processed in off-line mode (OFFL), using TM5-MP analysis data.

Table 2provides an overview of the operational TROPOMI NO_2 data processor versions starting with version 2.4.0, which was used in 2022 for a full mission reprocessing (older versions are listed in App. G); see also the latest NO_2 PRF [ER3]. The table also lists for each processor version the version number of the ATBD that describes the data product. It is important to realise that a change of processor version may imply significant changes in NO_2 and as general rule different version cannot be used together for time-series and trend studies.

Two remarks regarding the v2.4.0 full mission reprocessing (RPRO). (1) The RPRO was started with 30 April 2018, the first day of the operational phase, but in view of the spin-up of the TM5-MP data assimilation system the publicly released data starts on 01 May 2018. (2) The RPRO ended with 25 July 2022, i.e. overlapping the OFFL data by several days, and for this overlap period it is recommended to use the RPRO data.

The change to version 02.05.00 was a small bug fix in the OFFL code, which only affected the `qa_value` field in the datafiles over snow or ice covered regions. This update makes the OFFL consistent with NRTI and RPRO, as the update was made correctly in version 02.04.00 RPRO and NRTI, and is in agreement with Table 21 in App. E. In the corrected OFFL version there are more pixels with `qa_value` > 0.75 in case the scene pressure over snow/ice matches the surface pressure to within 4% (was 2% in previous versions). Users of the v02.04.00 OFFL data can adjust the `qa_value` by following this recipe:

```
if ( 0.50 < qa_value_v240 < 0.75 ) then
  if ( 80 < snow_ice_flag < 104 ) then
    if ( 0.96 <= apparent_scene_pressure / surface_pressure <= 0.98 ) then
       qa_value_v250 = qa_value_v240 * 0.88 / 0.73
```

The switch to version 02.06.00 contains no algorithm changes, only the addition of the geometric column N_v^{geo} data variable in the output product; cf. Tables 6 and 12.

The switch to processor version 02.07.01 contains several improvements in the NO_2 data product. The largest impact, comes from the new surface albedo climatology: the TROPOMI DLER v2.1 (see Sect. 6.4.5.2), based on the collection 3 Level-1b spectra, which includes a full degradation correction; this surface albedo update effectively means there is a discontinuity in the NO_2 dataset. To better help the data user to evaluate the quality of the NO_2 retrieval, the Wald-Wolfowitz runs test has been added to evaluate the DOAS fit residual, which has led to the addition of two variables in the data product (see Sect. 6.2.3). A new digital elevation map (DEM) for the surface elevation, based on the Copernicus 90 m DEM [ER9], solves some issues with the surface elevation notably over Greenland and some mountainous areas; the impact on the NO_2 data is expected to be small. The `qa_value` recipe (App. E) has been updated. The two main aspects: (1) `qa_value` reduction factors for the descending node were introduced and (2) the criterium for cloud-free snow-ice was relaxed from 4% to 6%, so that more pixels have a `qa_value` > 0.75 over snow-ice scenes. In version 02.07.01 the FRESCO cloud algorithm was updated to fix an issue with the definition of the reflectance errors, which was implemented in version 02.06.00 but which led to problems with the cloud pressure retrieval. With this fix the FRESCO algorithm is the same as in version 02.05.00.

The switch to processor version 02.08.00 contains some improvements in the NO_2 data product. The largest impact comes from an improvement in the FRESCO cloud algorithm, moving from three to two spectral windows and using the correct definition of reflectance errors (see Sect. 6.4.4.2 for details), leading to a much improved match between the scene pressure and surface pressure over cloud-free scenes. This especially improves the NO_2 retrieval over snow-covered cloud-free scenes, with more minor overall impacts for snow-free measurements in case of a small but non-zero cloud fraction. As a result of this improvement, the `qa_value` criterion (App. E) for cloud-free snow-ice scenes was tightened again from 6% to 3%. The DEM introduced in version 02.07.01 was therein used in the same manner as the previous DEM: as a static representative pixel-average surface altitude. As of version 02.08.00 the new DEM is used5 to compute the average surface altitude using the actual pixel geometry, making it now dynamic input (Table 8); the impact on the NO_2 data is expected to be minor. The Wald-Wolfowitz runs test (Sect. 6.2.3), introduced in the previous version, was updated to take missing or excluded spectral pixels into account correctly.

As of v2.9.1 the processor uses the new Level-1b v3.0 spectra – which features among others improvements in the degradation correction and in the flagging of transients ([RD12]) – as input; the impact of this on the NO_2 retrieval results is negligible. With this version the NO_2 DOAS SCD retrieval has been adapted to deal with an issue in the measured reflectance around 430 nm, details of which can be found in Sect. 6.2.4; the impact on the retrieval results is a small reduction of the SCD values in particular over remote areas, so that for most applications there will be little change in the NO_2 data, though a discontinuity in the data record may be visible.

All data (near-real time, offline and reprocessed) is freely accessible via the Copernicus Data Space Ecosystem [ER10]. Note that NRT data is available for the approximately the past 30 days; older NRT data is removed. See the TROPOMI website [ER11] for more information on data availability and dissemination.

6 Algorithm description

6.1 Overview of the NO_2 retrieval algorithm

The TROPOMI NO_2 processing system is based on the DOMINO and QA4ECV processing systems, with improvements related to specific TROPOMI aspects and new scientific insights. The basis for the processing is a retrieval-assimilation-modelling system which uses the 3-dimensional global TM5 chemistry transport model as an essential element. The retrieval consists of a three-step procedure, performed on each measured Level-1b spectrum:

1. the retrieval of a total NO_2 slant column density (N_s) from the Level-1b radiance and irradiance spectra measured by TROPOMI using a DOAS (Differential Optical Absorption Spectroscopy) method,
2. the separation of the N_s into a stratospheric ($N_s^{strat} = N_v^{strat} * M^{strat}$) and a tropospheric ($N_s^{trop}$) part on the basis of information coming from a data assimilation system, and
3. the conversion of the tropospheric slant column density into a tropospheric vertical column density ($N_v^{trop} = N_s^{trop}/M^{trop}$),

where M^{trop} and M^{strat} are the tropospheric and stratospheric air-mass factor (AMFs), which are derived from a look-up table of altitude-dependent AMFs and actual, daily information on the vertical distribution of NO_2 from the TM5-MP model on a $1^\circ \times 1^\circ$ grid; the altitude-dependent AMF depends on the satellite geometry, terrain height, cloud fraction and height and surface albedo.

The retrieval process is described in detail in the sections below.

6.2 Spectral fitting

The baseline method to determine NO_2 total slant columns is DOAS (see Platt [1994], Platt and Stutz [2008]). The DOAS fitting function for TROPOMI follows the current non-linear fitting approach for OMI (Boersma et al. [2011], Van Geffen et al. [2015], Van Geffen et al. [2020], [RD13]).

The reflectance spectrum observed by the satellite instrument, $R_{meas}(\lambda)$, is the ratio of the radiance at the top of the atmosphere, $I(\lambda)$, and the extraterrestrial solar irradiance, $E_0(\lambda)$ (where I also depends on the viewing geometry, but those arguments are left out for brevity):

$$R_{meas}(\lambda) = \frac{\pi I(\lambda)}{\mu_0 E_0(\lambda)} \tag{1}$$

where E_0 and I are recorded at the same detector row and given on the same wavelength grid (see Sect. 6.2.1), and $\mu_0 = \cos(\theta_0)$ is the cosine of the solar zenith angle. The E_0 is measured once a day, when TROPOMI crosses the terminator along a given orbit, and the TROPOMI data processing uses E_0 measured closest in time to I.

In space-borne DOAS, R_{meas} is related to the extinction of light by scattering and absorbing species along the average photon path between sun and satellite instrument. The effective, integrated absorption of NO_2 along the average photon path is represented by the total NO_2 slant column density (N_s). The DOAS spectral fitting is performed for all satellite ground pixels with $\theta_0 < 88^\circ$, so that there is no potential danger from the division by μ_0 in Eq. (1). The FRESCO cloud data product (Sect. 6.4.4) uses this θ_0 cut-off as well.

The DOAS spectral fitting attempts to find the optimal modelled reflectance spectrum, $R_{mod}(\lambda)$, by minimising the chi-squared merit function (cf. Sect. 6.2.2), i.e. the smallest possible differences between the observed and modelled reflectance spectrum:

$$\chi^2 = \sum_{i=1}^{n_\lambda} \left(\frac{R_{meas}(\lambda_i) - R_{mod}(\lambda_i)}{\Delta R_{meas}(\lambda_i)} \right)^2 \tag{2}$$

with n_λ the number of wavelengths in the fit window and $\Delta R_{meas}(\lambda_i)$ the noise on the reflectance, which depends on the radiance and irradiance noise given in the Level-1b product:

$$\Delta R_{meas}(\lambda_i) = \frac{1}{E_0(\lambda_i)} \sqrt{\left(\Delta I(\lambda_i)\right)^2 + \left(\Delta E_0(\lambda_i)\right)^2 \cdot \left(R_{meas}(\lambda_i)\right)^2} \tag{3}$$

i.e. on the signal-to-noise (SNR) of the measurements, where ΔI and ΔE_0 are the radiance and irradiance noise, respectively. For numerical reasons a maximum of 2500 is set to the SNR on the reflectance and ΔR_{meas}

is adjusted upwards when this SNR limit is exceeded. In the NO_2 wavelength range the SNR is typically 1500, but it may be larger over very bright scenes (notably clouds), potentially leading to saturation effects in the spectra, hence limiting the SNR does not pose a significant limit on the lowest SCD error estimates (the lower ΔR_{meas} the lower the SCD error is).

The magnitude of χ^2 is a measure for how good the fit is. Another measure for the goodness of the fit is the so-called root-mean-square (RMS) error, which is defined as follows:

$$R_{\text{RMS}} = \sqrt{\frac{1}{n_\lambda}\sum_{i=1}^{n_\lambda}\Big(R_{\text{meas}}(\lambda_i) - R_{\text{mod}}(\lambda_i)\Big)^2} \tag{4}$$

where the difference $R_{\text{meas}}(\lambda) - R_{\text{mod}}(\lambda)$ is usually referred to as the residual of the fit; see Sect. 6.2.3 for further analysis of the DOAS fit residual.

Radiance spectral pixels that are flagged in the Level-1b data as bad or as suffering from saturation, or that are flagged by the outlier removal (see below) are filtered out before doing any further processing step. It is also possible to manually define one or more wavelength bands that need to be excluded from the DOAS fit; in the default configuration of the NO_2 retrieval this option is not used. In the processor excluding spectral pixels is done by setting the error on the reflectance of the spectral pixels that are flagged or to be excluded to 10^4 times the measurement: $\Delta R_{\text{meas}}(\lambda_i) = 10^4 \times R_{\text{meas}}(\lambda_i)$, as a result of which spectral pixel i does not contribute to the DOAS minimisation of the χ^2 in Eq. (2). In the computation of the RMS error in Eq. (4), these flagged or excluded pixels are skipped.

The baseline model function for TROPOMI follows the approach for OMI and reads as follows:

$$R_{\text{mod}}(\lambda) = P(\lambda)\cdot\exp\Big[-\sum_{k=1}^{n_k}\sigma_k(\lambda)\cdot N_{\text{s},k}\Big]\cdot\Big(1 + C_{\text{ring}}\frac{I_{\text{ring}}(\lambda)}{E_0(\lambda)}\Big) \tag{5}$$

with $\sigma_k(\lambda)$ the absolute cross section and $N_{\text{s},k}$ the slant column amount of molecule $k = 1,\ldots,n_k$ taken into account in the fit (NO_2, O_3, etc.), C_{ring} the Ring fitting coefficient and $I_{\text{ring}}(\lambda)$ the synthetic Ring spectrum (generated from an $E_{\text{ref}}(\lambda)$ reference irradiance) and $E_0(\lambda)$ the measured irradiance. The Ring spectrum describes the differential spectral signature arising from inelastic Raman scattering of incoming sunlight by N_2 and O_2 molecules. The last term in Eq. (5) describes both the contribution of elastic scattering to the differential absorption signatures (i.e. the 1), and the modification of these differential structures by inelastic scattering (the $+C_{\text{ring}}\cdot I_{\text{ring}}(\lambda)/E_0(\lambda)$ term) to the reflectance spectrum. The sources of the reference spectra used are discussed in Sect. 6.2.5.

In the modelled spectrum of Eq. (5) a polynomial of order n_p with coefficients a_m:

$$P(\lambda) = \sum_{m=0}^{n_p} a_m\lambda^m \tag{6}$$

is introduced to account for spectrally smooth structures resulting from molecular (single and multiple) scattering and absorption, aerosol scattering and absorption, and surface albedo effects. Because of the polynomial term, only the highly structured differential absorption features contribute to the fit of the slant column densities. In order to prevent the numerical value of the polynomial components in Eq. (6) to become very large or very small (for the $405-465$ nm fit window, for example, usually $n_p = 5$), the wavelengths are scaled to the range $[-1:+1]$ over the fit window in the processor.

Fig. 5 shows an example of a reflectance spectrum observed by TROPOMI on 4 July 2018 during orbit 03747, along with the modelled spectrum obtained from the DOAS fit using Eq. (5). The (almost cloud-free) ground pixels lies over the industrial area of Rotterdam (scanline 2012, row 323, $\theta_0 = 27.82^\circ$, $\theta = 31.47^\circ$). Fit results: $N_{\text{s,NO}_2} = 2.73\times10^{16}$ molec/cm^2, $N_{\text{v,NO}_2} = 1.60\times10^{16}$ molec/cm^2, $N^{\text{trop}}_{\text{v,NO}_2} = 1.52\times10^{16}$ molec/cm^2, RMS $= 1.59\times10^{-4}$. The residual (shown in the bottom panel of Fig. 5) is of the order of 10^{-4}, corresponding to an unexplained residual reflectance (which is about equal to the differential optical depth times the average reflectrance in the fit window; Van Geffen et al. [2020]) of that magnitude.

In order to remove strong outliers in the DOAS fit residual (caused by, e.g., high-energy particles hitting the CCD detector, variations in the dark current, or bad pixels not correctly flagged in the Level-1b data), a "spike removal" algorithm was implemented in v2.2.0 of the DOAS processor to detect outliers in the fit residual. Spectral pixels identified as outliers are treated in the same way as pixels that are flagged in the Level-1b data; see below Eq. (4). After removal of the spectral pixels of such outliers from the measured reflectance, the NO_2 DOAS fit is redone to provide the final fit parameters. See App. F and Van Geffen et al. [2022] for a description and examples of the spike removal.

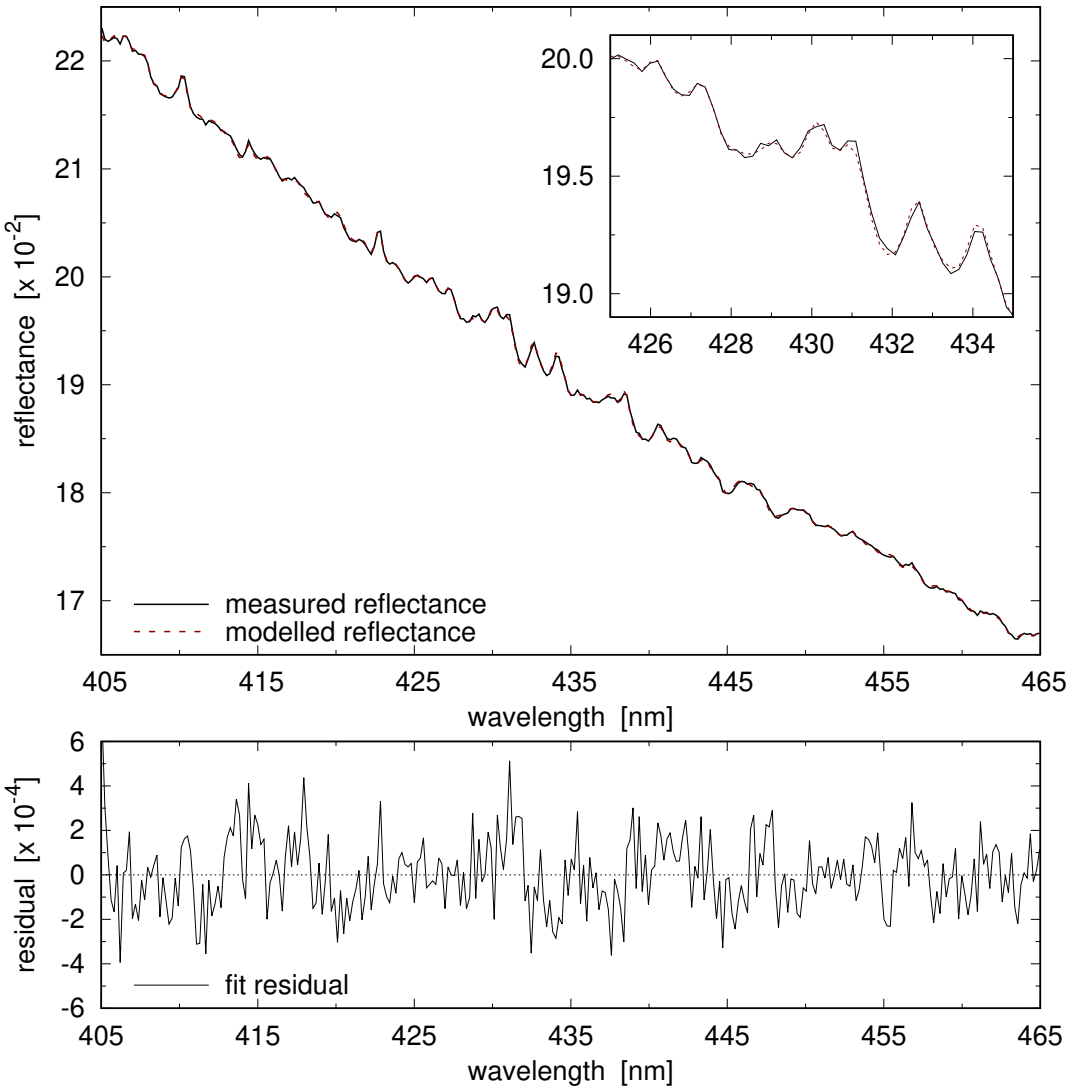

Figure 5: The *top panel* shows an example of a reflectance spectrum (black solid line) obtained by TROPOMI on 4 July 2018 during orbit 03747 and the spectrum modelled in the DOAS fit procedure (dashed red line); the inset shows an enlargement of a 10 nm wide part of the fit window. The *bottom panel* shows the residual of the DOAS fit, i.e. the measured minus the modelled reflectance spectrum; note that the vertical scale is a factor of 100 smaller than the scale in the top panel.

Table 3 provides an overview of the operational DOAS fit settings used in the TROPOMI processor and those used for some current and past UV/Vis backscatter satellite instruments: the fit window, the reference spectra used in the fit (see Sect. 6.2.5) and the degree of the DOAS polynomial. Note that for the processing of GOME(-1) data it was necessary to include a correction for the undersampling of the spectra, i.e. the fact that the spectral sampling is of the same order as the FWHM of the instrument slit function. For the instruments listed in Table 3 this correction is not necessary: their spectral resolution, i.e. the FWHM of the slit function, is 2–3 times as large as their spectral sampling. For TROPOMI, for example, the spectral sampling is about 0.2 nm and the FWHM is about 0.55 nm [RD4].

6.2.1 Wavelength calibration & common wavelength grid

Both the irradiance and radiance spectra are wavelength calibrated prior to the DOAS fit, using the same wavelength calibration approach, in the $[\lambda_b : \lambda_e]$ wavelength window. Prior to NO_2 data version v2.2.0 this window equalled the NO_2 fit window, with $\lambda_b = 405$nm and $\lambda_e = 465$nm. As of v2.2.0 the NO_2 processor includes the O_2–O_2 slant column retrieval for cloud properties (see Sect. 6.4.4.3) and to accommodate this fit

Table 3: Main settings of the operational DOAS retrieval of NO_2 for TROPOMI, and for the current and previous satellite instruments in the operational processing of KNMI, which converts the NO_2 slant column data products into tropospheric and stratospheric vertical column data. For OMI the settings used for the QA4ECV v1.1 processing ([RD6], [ER7]) are given; these are an extention of the settings used for the DOMINO v2 processing (see Sect. 6.2.6 for a brief discussion).

	TROPOMI	OMI (QA4ECV v1.1)	GOME-2 (TM4NO2A v2.3)	SCIAMACHY (TM4NO2A v2.3)
wavelength range [nm]	$405-465$	$405-465$	$425-450$	$426.5-451.5$
omitted range [nm]	$428-433$ †	—	—	—
secondary trace gases	O_3, H_2O_{vap}, O_2–O_2, H_2O_{liq}	O_3, H_2O_{vap}, O_2–O_2, H_2O_{liq}	O_3, H_2O_{vap}, O_2–O_2	O_3, H_2O_{vap}, O_2–O_2
pseudo-absorbers	Ring	Ring	Ring	Ring
fitting method	non-linear	non-linear	linear	linear
degree of polynomial	5	5	3	2
polarisation correction	no	no	no	yes
slant column processing	PDGS (@ DLR)	NASA / KNMI	DLR / BIRA-IASB	BIRA-IASB
references	[VanGeffen et al., 2020] [VanGeffen et al., 2026]	[Boersma et al., 2011] [Van Geffen et al., 2015]	[Valks et al., 2011] [Liu et al., 2019]	[Van Roozendael et al., 2006]

† See Sect. 6.2.4

the wavelength calibration windows is extended to $\lambda_e = 495$nm.

Using the subscripts 'nom' and 'cal' to denote nominal (i.e. from the Level-1b data product [RD12]) and calibrated wavelengths, respectively, the calibrated irradiance and radiance to be used in Eq. (1) are then given by:

$$E_0(\lambda_{\text{cal}}^{E0}) = E_0(\lambda_{\text{nom}}^{E0} + w_s^{E0})$$
$$I(\lambda_{\text{cal}}) = I(\lambda_{\text{nom}} + w_s + w_q(\lambda_{\text{nom}} - \lambda_0)) \quad (7)$$

where w_s represents a wavelength shift and w_q a wavelength stretch ($w_q > 0$) or squeeze ($w_q < 0$), with w_q defined w.r.t. the central wavelength of the fit window λ_0. Since in view of numerical stability, the wavelengths are scaled to the range $[-1:+1]$ over the fit window, computationally $\lambda_0 = 0$. Each wavelength calibration of Eq. (7) comes with its own χ^2_w as a goodness-of-fit. Turning on the w_q fit parameter in the calibration of the radiance of a given TROPOMI orbit resulted in a very small stretch with a precision larger than the stretch itself, and the effect on the retrieval results is negligible [Van Geffen et al., 2020], and hence the w_q fit parameter will remain turned off. Note that for the irradiance calibration we only consider a shift.

In order to avoid possible extrapolations, both these steps are performed on a wavelength range that is 1 nm wider than the fit window, i.e. the measured reflectance is formed on the common wavelength grid and then cut to the fit window. Up to v1.4.0 of the NO_2 processor the spectal pixel index selection is based on the first pixel after λ_b and the last before λ_a. As of v2.2.0 the selection is based on nearest neighbours, providing a more consistent pixel index selection along-track.

The wavelength calibration of Eq. (7) is performed on the irradiance at the start of the processing of a given granule, and per radiance spectrum prior to forming the measured reflectance of Eq. (1). In order to form this reflectance, both (calibrated) spectra $I(\lambda)$ and $E_0(\lambda)$ need to be given on the same wavelength grid. In our approach $E_0(\lambda)$ is converted to the radiance wavelength grid by way of a high-sampling interpolation, taking advantage of the fact that we have additional information from a high-resolution solar reference spectrum $E_{\text{ref}}(\lambda)$. Details of the wavelength calibration and the high-sampling interpolation implemented for TROPOMI are given in Appendices A and B, respectively.

6.2.2 Minimising the chi-squared merit function

Slant column densities $N_{s,k}$, the Ring coefficent C_{ring}, and the polynomial coefficients a_m are obtained from a minimisation of the χ^2 of Eq. (2), i.e. the differences between the observed and modelled reflectances. In the initial TROPOMI NO_2 DOAS, we implented a version of the OMI NO_2 DOAS processor, called OMNO2A, which uses a non-linear least squares fitting based on routines available in the SLATEC mathematical library

[Vandevender and Haskell, 1982]. During the commissioning phase, however, we discovered that this implementation suffered from some issues (in particular the χ^2 and/or the slant column error estimates were scaled incorrectly) that could not be solved due to inflexibility of the OMNO2A code. To solve this issue, we chose to use the optimal estimation (OE) routine based on Rodgers [2000] already available in the processor, since it was implemented for the wavelength calibration; see App. A.

For the χ^2-minimisation using the OE solver suitable a-priori values of the fit parameters were selected and the a-priori errors are set very large, so as not to limit the solution of the fit, while for numerical stability reasons a pre-whitening of the data is performed. (Whitening transforms a vector of random variables with a known covariance matrix into a set of new variables whose covariance is the identity matrix, meaning that they are uncorrelated and each have variance 1; cf. Rodgers [2000], Ch. 2.)

A number of fitting diagnostics is provided by the fitting procedure. Estimated slant column and fitting coefficient uncertainties are obtained from the covariance matrix of the standard errors, which is given as a standard output of the OE procedure. The estimates of the SCD error (ΔN_s) are scaled with the square-root of the normalised χ^2, where χ^2 is normalised by $(n_\lambda - D)$, with n_λ the number of wavelengths in the fit window and D the degrees of freedom of the fit, which is almost equal to the number of fit parameters. All fitting coefficients are provided in the NO_2 output data file as diagnostic data.

For quality control reasons two limits are set on the retrieved NO_2 slant column: if $|N_{s,NO_2}| < \Delta N_{s,NO_2}$ and/or if $N_{s,NO_2} < (N_s)^{min} = -20.0\times10^{-6}$ mol/m^2 ($= -1.2\times10^{15}$ molec/cm^2) then the retrieval results are considered to be unreliable and the `generic_range_error` flag of the `processing_quality_flags` is raised, indicating that a fatal error has occurred, which sets the `qa_value` to zero. And if the NO_2 slant column error is too large, i.e. if $\Delta N_{s,NO_2} > (\Delta N_{s,NO_2})^{max} = 33.0\times10^{-6}$ mol/m^2 ($= 2\times10^{15}$ molec/cm^2), then the `qa_value` is reduced to 0.15 (App. E, Table 21). The thresholds are configuration parameters; the values given here are the default values and these are currently in use.

6.2.3 The DOAS fit residual and the Wald-Wolfowitz runs test

In the minimisation of the χ^2 of Eq. (2), DOAS tries to find the optimal combination of the fit parameters it has available in the modelled reflectance of Eq. (5). The difference between the measured and modelled reflectance, $R_{meas}(\lambda) - R_{mod}(\lambda)$, that is left after this minimisation is the fit residual. The modelled reflectance is set up to describe atmospheric processes as best as possible for most circumstances worldwide. Ideally the fit residual will be close to zero and more or less evenly fluctuating around zero over the full fit window, as in the bottom panel of Fig. 5. If, however, at a certain location a species that absorbs, emits and/or scatters light is present in the light path, but which is not included in $R_{mod}(\lambda)$ by way of a reference spectrum, then DOAS cannot use it as a relevant fit parameter in the χ^2 minimisation. The combination of fit parameters DOAS then comes up with may be incorrect, resulting in an inaccurate NO_2 slant column, even though this may not have led to an unusually value for the χ^2 and/or the R_{RMS}.

An example of this effect was found when investigating fit residuals of retrievals over Tibetan lakes, after Kong et al. [2023] pointed to unusually high NO_2 tropospheric columns over these lakes compared to their immediate surroundings. The top row of Fig. 6 shows the fit residual for two ground pixels, one over Lake Siling and one over land just outside that lake. The fit residual of the land pixel (Fig. 6a) shows no clear structures and fluctuates as expected around zero, while in the fit residual of the water pixel (Fig. 6b) there is a clear low frequency structure visible around 430 nm and above. Some kind of absorber present in the water is clearly not accounted for in the modelled refectance, but what absorber that may be – organic matter, chlorophyll, sediment, ... – is unkown. Though χ^2, R_{RMS} and the NO_2 SCD error estimate $\Delta N_{s,NO_2}$ for the lake pixel are higher than for the land pixel (cf. Table 4), they are not worryingly large and the water pixel is not flagged as unreliable.

If there are no sources of NO_2 in the lake, one expects the troposheric VCD to be more or less the same for the two pixels. Given that the lake has a lower albedo than the surrounding land, one thus expects the tropospheric SCD to be a little lower over the lake than over land (as the AMF decreases with decreasing albedo). Since over the short distance between the two pixels, some 75 km, the stratospheric VCD may be considered constant, the total NO_2 SCD is thus expected to be a little lower over the lake than over the land. Instead, the lake pixel appears to have a higher SCD than the land pixel (cf. Table 4), leading to a considerably higher troposheric VCD over the lake, attributed by Kong et al. [2023] to NO_2 emissions in the Tibetan lakes.

With the large structure left in the water pixel fit residual, however, it seems likely that the NO_2 SCD value determined by DOAS is not reliable, as argued by Labzovskii et al. [2024]. A tell-tale sign of problems with the fit in this case is that the water vapour coefficients is very large negative over the water, while it is small positive over land. Though, obviously, the fit is not optimised for retrieving water vapour coefficients and the right values for this are unknown, but a large negative value seems unlikely. On the other hand, a large negative vapour

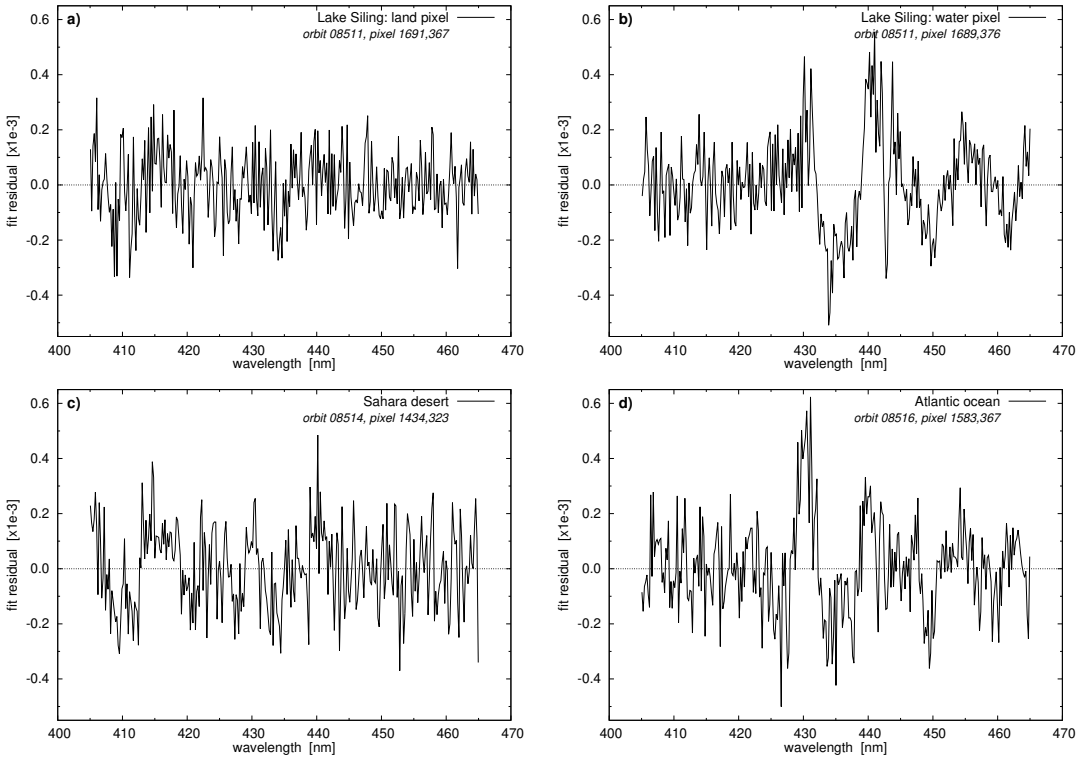

Figure 6: Examples of DOAS fit residuals for orbits on 5 June 2019 (orbit and ground pixel numbers are given in the legends). Panels a) and b) are for ground pixels next to and over the Tibetan lake Siling, respectively; these are used in Labzovskii et al. [2024]. Panels c) and d) are over the Sahara desert and over the Atlantic Ocean, respectively.

Table 4: Some results from the DOAS fit for the examples shown in Fig. 6; the geometric column density (GCD) is defined in Eq. (20).

		Lake Siling		Saraha	Atlantic	
	symbol	land	water	desert	ocean	unit
Fig. 6 panel		a	b	c	d	
NO_2 SCD	N_{s,NO_2}	170.19	187.41	128.97	146.12	μ mol/m^2
NO_2 SCD error	$\Delta N_{s,NO_2}$	8.08	13.07	6.93	9.52	μ mol/m^2
NO_2 GCD	N^{geo}_{v,NO_2}	70.55	75.67	58.01	60.65	μ mol/m^2
NO_2 GCD error	$\Delta N^{geo}_{v,NO_2}$	3.35	5.28	3.12	3.95	μ mol/m^2
RMS of the fit	R_{RMS}	1.21	1.63	1.45	1.66	$\times 10^{-4}$
χ^2 of the fit	χ^2	3.60	6.55	4.06	5.32	$\times 10^{+2}$
no. of spectral points	n_λ	305	305	305	305	
no. of positive values	k_p	155	152	152	144	
no. of negative values	k_n	150	153	153	161	
no. of observed runs	k_r^{obs}	138	110	100	98	
no. of expected runs	k_r^{exp}	153.46	153.50	153.50	153.03	
sigma of that	σ_r^{exp}	8.72	8.72	8.72	8.69	
deviation from expected	R_D	-1.77	-4.99	-6.14	-6.33	sigma
longest observed run	R_L	10	35	33	33	

coefficient does not automatically imply an unreliable NO_2 SCD value; it could also signal other retrieval issues, e.g. at large SZA.

The discovery of the structures in the fit residual over the Tibetan lakes has prompted us to implement

a statistical test after the DOAS retrieval, in order to try to signal for remaining low frequency structures in the fit residual: the Wald-Wolfowitz runs test, or 'runs test' for short (Barlow [1989], Sect. 8.3.2; [ER12]). This test checks a randomness hypothesis based on the number of positive (k_p) and negative (k_n) values in the fit residual, where a sequence of same-signed values is called a "run", and $n_\lambda = k_p + k_n$ the number of spectral points in the fit window. The number of expected runs, k_r^{exp}, the variance σ_r^2, and the deviation in terms of the standard deviation σ_r, R_D, are given by:

$$\begin{aligned} k_r^{\text{exp}} &= 1 + (2\,k_p\,k_n)\,/n_\lambda \\ V(k_r^{\text{exp}}) = \sigma_r^2 &= (2\,k_p\,k_n\,(2\,k_p\,k_n - n_\lambda))\,/\left(n_\lambda^2\,(n_\lambda - 1)\right) \\ R_D &= \left(k_r^{\text{fit}} - k_r^{\text{exp}}\right)/\sigma_r \end{aligned} \tag{8}$$

where k_r^{fit} is the number of runs in the fit residual.

The deviation R_D has been defined here with a sign in order to make a distiction between fewer-than-expected ($R_D < 0$) and more-than-expected ($R_D > 0$) runs, i.e. to identify between low-frequency and high-frequency structures, respectively, in the fit residual. An additional quantity that proves to be useful is the length of the longest run, R_L, in the fit residual. Table 4 provides some results for the DOAS fit and the runs test for the examples shown in Fig. 6. The Wald-Wolfowitz test also provides a probability to find k_r^{fit} runs, but investigation of that showed that this quantity does not provide useful additional information.

An R_D of, for example, ± 5 (in terms of standard deviation σ_r) means the number of runs in the fit residual is really in the tail of the distribution. And an R_L of, say, > 20 is a significant fraction of the fit window length (n_λ is around 304 for TROPOMI). But both R_D and R_L are continuous variables and it is not clear where to put a line between "good" and "bad" results and thus adjust the `qa_value`, just like is the case for the R_{RMS} and χ^2 of the fit. In addition, it is not certain that large R_D and R_L values actually mean that the retrieved NO_2 SCD value is incorrect. And, vice versa, it is not certain that problems with the fit will always be picked up in the from of large R_D and R_L values. If, for example, the noise on the reflectance is large – as is the case in the 22 rows on the west side and 20 rows on the east side of the swath – the pixel-to-pixel variation in the fit residual is large, potentially creating more sign changes and thus possibly hiding larger systematic structures in the random noise.

When investigating other areas with the runs test, several situations where both R_D and R_L are large where found, other than those showing up over the Tibetan lakes. Two examples are given in Fig. 6. A fit residual over the Saharan desert (Fig. 6c) shows a clear feature around 415 nm, the nature of which is unknown, as is the effect it may have on the retrieved NO_2 SCD. A fit residual over the Atlantic ocean (Fig. 6d) shows a large peak around 430 nm, which may be related to vibrational Raman scattering (VRS) in open ocean waters. It is known that tropospheric NO_2 columns over some parts of the oceans are a little higher than expected – the feature left in the residual of Fig. 6d may thus be an indication that the DOAS fit for these circumstances results in incorrect NO_2 SCD values. This issue is further discussed in Sect. 6.2.4.

As of NO_2 v2.7.1 both R_D and R_L are added to the data product as *additional independent* information for the data user. At the moment of writing (Spring 2024) the situations under which and locations where R_D and R_L are large are still under investigation. For now the advice to the data user, added also to the PUM of v2.7.1, is as follows: (1) if unexpected NO_2 tropospheric VCD values are found, and (2) the NO_2 SCD – or: the geometric column, GCD, defined in Eq. (20) – also shows unexpected values, the issue is in the measurement data itself (i.e. not in the AMF, troposphere/stratosphere separation, etc.), then (3) check the values of R_D and R_L: if these are large, there seems to be a problem with the DOAS fit, as a result of which the NO_2 SCD may be unreliable. If that is the case, a closer look at the fit residuals by the data product leads is required. As mentioned above, however, residual structures are not always picked up by the runs test. (In view of the large data volume this would require, it is simply not feasible to add the fit residuals to the data product, and in addition it would not be useful for most cases and most data users.)

Some specifics on calculating the number of runs

A "run" is a sequence of same-signed spectral pixels in the DOAS fit residual. Spectral pixels that are flagged (masked) – due to error flags e.g. from Level-1b, from the outlier removal (App. F), or from excluding certain wavelength bands from the fit – are not included in the runs counts (just as they are not included in χ^2 and R_{RMS}; cf. below Eq. (4)): n_λ is the number of non-flagged spectral pixels). Hence:

- The first run starts at the first non-flagged spectral pixel in the residual.
- Each sign change in the fit residual value means the start of a new run.
- A sequence of one or more flagged spectral pixels constitutes one sign change, irrespective of (a) the sign of the residual before and after the sequence, and (b) the length of the sequence.

- The last run ends at the last non-flagged spectral pixel in the residual.

6.2.4 Dealing with the Fraunhofer lines related issue at 430 nm

As mentioned above in relation to the fit residual shown in Fig. 6d, clear-sky pixels over open water often show a systematic feature around 430 nm that result in less accurate NO_2 retrieval results for those pixels. This issue is investigated in detail by Van Geffen et al. [2026], who show that fit residuals of clear-sky pixels over land may also show a clear structure around 430 nm, such as pixels over Western Australian shrub land. Other fit residuals seem to have a similar feature but it only stands out clearly if the residual over the remainder of the fit window is close to zero; if there are clouds and/or other issues with the retrieval, the 430 nm peak is small compared to the noise in the residual.

The feature around 430 nm is related to Fraunhofer lines in the solar spectrum. The width and depth of the Fraunhofer lines in the measured radiance spectrum are affected by rotational Raman scattering (RRS), or the Ring-effect, throughout the atmosphere, which is accounted for in the DOAS retrieval by way of a single scalable fixed reference spectrum; cf. Eq. (5). As Western Australian land pixels show, the Ring correction does not fully deal with the 430 nm Fraunhofer structures, partly also because the depth of that structure varies over time with the solar activity cycle. Over open water, such as clear-sky Atlantic Ocean pixels like the one of Fig. 6d, the situation is worsened by vibrational Raman scattering (VRS) in the water. It is not possible to accounting for VRS with a single scalable reference spectrum, since VRS characteristics depend on several aspects, including the material dissolved in the water, such as chlorophyll.

The solution proposed by Van Geffen et al. [2026], which has been implemented in the TROPOMI NO_2 retrieval in version v2.9.1, is to omit the wavelength range $428-433$ nm from the DOAS fit. This "NO2-gap" approach appears to reduce the SCD and RMS errors for cases where the 430 nm peak stands out clearly, while not worsening the results elsewere; the decrease of these errors varies with the solar activity cycle. For the pixels that show this decrease, the SCD value itself may be reduced a little, though there is quite some scatter in the change of the SCD values. The overall effect of this is that the stratospheric VCD decreases on average a little, while over land there are small changes in the tropospheric VCD; these changes are too small to alter the general conclusions of the routine validation of TROPOMI data significantly. For further details and a discussion of related points, see Van Geffen et al. [2026]. Note that this approach does not solve the broad-band absorption features above 430 nm visible in Fig. 6b and 6d, which are likely to be related to material dissolved in the water.

To investigate the magnitude and occurence of the 430 nm peak in the fit residual, the ratio of the RMS of the peak – i.c. the wavelength range $[429:432]$ nm, which spans about 15 spectral pixels – and the RMS of the rest of the fit window:

$$Q^{430}_{\mathrm{RMS}} = \frac{R_{\mathrm{RMS}}(\lambda \in [429:432])}{R_{\mathrm{RMS}}(\lambda \notin [429:432])} \tag{9}$$

was added to the retrieval code: the higher the ratio, the more pronounced the 430 nm peak stands out against the noise in the fit residual. With the introduction of the "NO2-gap", the result of Eq. (9) is undefined; the calculation is left in the retrieval code for testing purposes. The ratio is not part of the nominal level-2 data files; like fit residuals it is part of the diagnostic (debug) output that can be activated during local (re)processing.

6.2.5 Reference spectra

The selection of the reference spectra for the trace gas cross sections in Eq. (5) is driven by whether a species shows substantial absorption in the wavelength range relevant for NO_2 retrieval, and exploits the best available sources prior to commissioning phase. Experience with OMI has shown that NO_2, ozone, water vapour, and Rotational Raman Scattering (RRS), i.e. the inelastic part of the Rayleigh scattering (the so-called "Ring effect"), are most relevant in the wavelength interval relevant to NO_2. Van Geffen et al. [2015] (cf. Sect. 6.2.6) showed that including also absorption in liquid water and by the O_2–O_2 collision complex improves the fit, hence these are included for TROPOMI.

High-resolution laboratory measured absorption cross sections are convolved with the TROPOMI slit function (or: instrument spectral response function, ISRF; available via [ER13]), and sampled at a resolution of 0.01 nm to create the necessary reference spectra in the data files used by the processor. Since the ISRF is (slightly) different for different detector rows, the convolved reference spectra are determined per detector row. Given the relative smoothness of these convolved cross sections, interpolation to the radiance wavelength grid in Eq. (5) is performed by way of a 4th degree spline interpolation. The final set of reference spectra (see also [RD14] and Fig. 7) is:

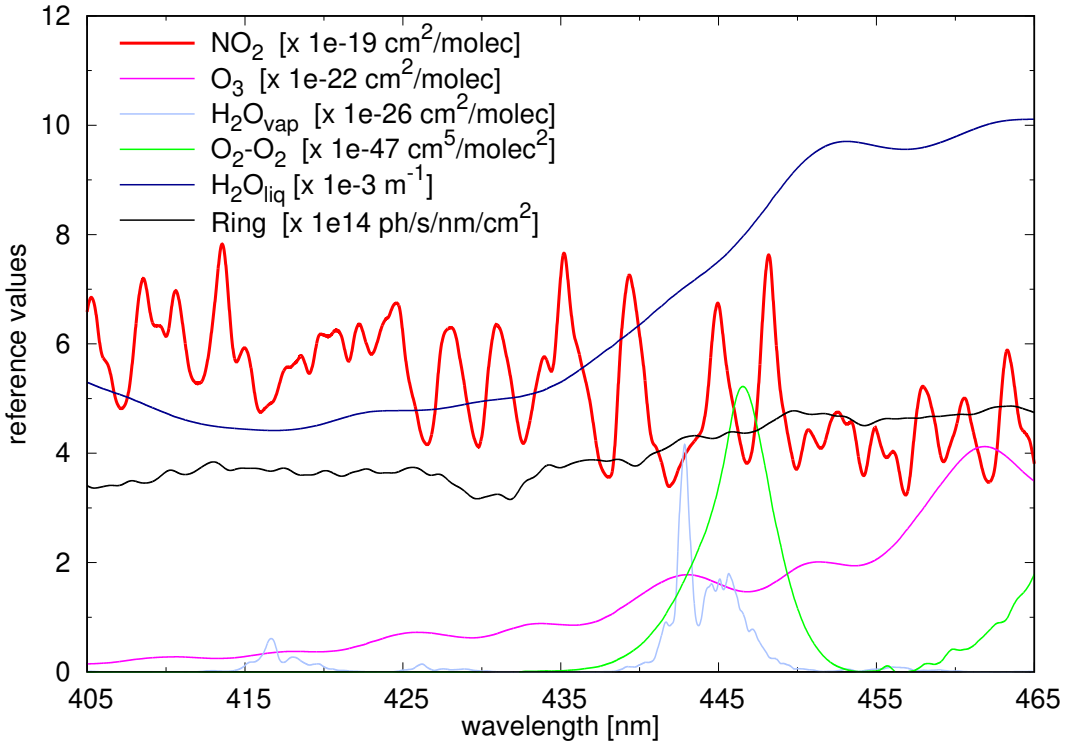

Figure 7: Absorption cross sections $\sigma_k(\lambda)$ for NO_2, O_3, water vapour, O_2–O_2 and liquid water, as well as the Ring spectrum $I_{\text{ring}}(\lambda)$, the pseudo-absorber which accounts for the Ring effect, in Eq. (5) for the $405-465$ nm wavelength range used in the TROPOMI data processor. The reference spectra have been multiplied by the factors given in the plot legend to make the spectral signatures visible in one plot.

- trace gas cross sections $\sigma_k(\lambda)$ in Eq. (5):
  - NO_2 from Vandaele et al. [1998] at 220 K; see [ER14]
  - O_3 from Gorshelev et al. [2014] and Serdyuchenko et al. [2014] at 243 K
  - Water vapour (H_2O_{vap}) based on HITRAN 2012 data
    (see Van Geffen et al. [2015] and Sect. 4.1 of [RD14])
  - O_2–O_2 from Thalman and Volkamer [2013] at 293 K
  - Liquid water (H_2O_{liq}) from Pope and Frey [1997],
    resampled at 0.01 nm with a cubic spline interpolation
- an effective Ring spectrum $I_{\text{ring}}(\lambda)$ following Chance and Spurr [1997]
  (see Van Geffen et al. [2015] and Sect. 4.2 of [RD14])
- a high-resolution solar reference spectrum $E_{\text{ref}}(\lambda)$ from Chance and Kurucz [2010]
  (see also Dobber et al. [2008])

The inclusion of absorption by soil (as discussed by e.g. Richter et al. [2011]; Merlaud et al. [2012]) is not considered for TROPOMI, as its potential absorption signal lies well above 465 nm, the upper limit of the NO_2 fit window. Also currently not being considered for inclusion in the fit is the vibrational Raman scattering (VRS) in clear ocean waters (e.g. Vasilkov et al. [2002], Vountas et al. [2003]), as its potential effect on the fit is currently poorly understood, while it is clear that compensation for VRS by way of a single scalable reference spectrum is not feasible, since VRS characteristics depend on several aspects, including the material dissolved in the water, such as chlorophyll, cf. Sect. 6.2.4 and 6.2.7.

The temperature for the O_3, H_2O_{vap} and O_2–O_2 cross section spectra is fixed. Variation of these cross section temperatures has little effect on the fit residual in the retrieval of NO_2 slant columns, since the shape of the differential NO_2 cross section is in good approximation invariant of temperature. In the case of TROPOMI, the baseline is to use an NO_2 cross section that has been measured for 220 K.

Note that the amplitude of the differential cross section features has a significant temperature dependence which is important to account for. The resulting NO_2 slant column are corrected for deviations from 220 K at later retrieval steps, as described in Sect. 6.4.2.

6.2.6 DOAS fit details for OMI and TROPOMI

Comparisons of OMI NO_2 data from the DOMINO v2 processing system to independent data from other instruments have shown that OMI slant NO_2 columns are higher than columns derived from GOME-2 and SCIAMACHY (as first stated by N. Krotkov at the OMI Science Meeting in Sept. 2012), as well as columns derived from ground-based measurements. Due to the separation between stratospheric and tropospheric NO_2, which proceeds in the same way for the three satellite instruments, the high bias in the NO_2 slant columns is propagated to the stratospheric column [Belmonte Rivas et al., 2014].

Van Geffen et al. [2015] showed that improving the OMI wavelength calibration of the Level-1b spectra in the OMNO2A data processing of the NO_2 slant columns used by DOMINO v2 reduces both the total NO_2 slant column values and the RMS of the DOAS fit. Van Geffen et al. [2015] further showed that including both O_2–O_2 and H_2O_{liq} (discussed by e.g. Richter et al. [2011], Lerot et al. [2010]) in the fit improves the OMI NO_2 fit results and ensures that fit coefficients for O_3 and O_2–O_2 have realistic values. Criteria for establishing what are the best settings for the fit can be summarised as follows: (a) a low error on the NO_2 slant column, (b) a low RMS error value, (c) inclusion of secondary trace gases that clearly improve the fit, e.g. by removing specific features in the fit residual, (d) physically realistic values for the slant column values of these secondary trace gases.

The improvements described by Van Geffen et al. [2015] for OMNO2A have been used for the processing of OMI NO_2 data within the QA4ECV-project ([RD6], [ER7]), which demonstrated that the different spectral fitting approaches lead to consistent results, but with better precision for the QA4ECV spectral fitting algorithm [Zara et al., 2018]. The improvements are incorporated in the TROPOMI NO_2 slant column processing. For comparisons between TROPOMI and OMI slant column retrieval results, see Van Geffen et al. [2020].

6.2.7 Some notes regarding other DOAS implementations

Many implementations of DOAS deploy a linearised version of Eq. (5), with the Ring effect included as a pseudo-absorber, giving the equation in terms of optical depth rather than in terms of reflectances:

$$ln[R_{\text{mod}}(\lambda)] = P^*(\lambda) - \sum_{k=1}^{n_k} \sigma_k(\lambda) \cdot N_{\text{s},k} - \sigma_{\text{ring}}(\lambda) \cdot C^*_{\text{ring}} \tag{10}$$

where the Ring coefficient C^*_{ring} and the polynomial $P^*(\lambda)$ are essentially different from C_{ring} and $P(\lambda)$ in Eq. (5). In this approach the Ring cross section $\sigma_{\text{ring}}(\lambda)$ is constructed from the Ring radiance spectrum $I_{\text{ring}}(\lambda)$ divided by a reference solar spectrum minus a low-order polynomial (so that $\sigma_{\text{ring}}(\lambda)$ varies around zero). The relation between C_{ring} and C^*_{ring} is discussed briefly by Van Geffen et al. [2020]. Note that because the formulation in Eq. (10) uses $ln[R(\lambda)]$ – rather than $R(\lambda)$ as in Eq. (5) – both the χ^2 and RMS error R_{RMS} are also formulated using this $ln[R(\lambda)]$ and can therefore not be compared directly to the results of Eqs. (2) and (4), respectively; cf. Van Geffen et al. [2020].

The linearisation leading to Eq. (10) allows then for the use of a linear least squares fitting routine, which is computationally faster than a non-linear solver needed when using Eq. (5). We feel, however, that the Ring effect is physically described better by the non-linear approach of Eq. (5) and we therefore use that in the NO_2 data processing for TROPOMI. Apart from dropping the physical description of the Ring effect, a disadvantage of the linearised approach is that error propagation is no longer straightforward, because taking the logarithm of the observed spectra implies that the error no longer has a Gaussian distribution.

Several DOAS applications include an intensity offset correction, a constant or linear in wavelength, to improve the retrievals in some spectral ranges. The precise physical origin of such an intensity offset is not known, but it is thought to be related to instrumental issues (e.g. incomplete removal of stray light or dark current in Level-1b spectra) and/or atmospheric issues (e.g. incomplete removal of Ring spectrum structures, vibrational Raman scattering (VRS) in clear ocean waters); see, for example, Platt and Stutz [2008], Richter et al. [2011], Lampel et al. [2015], [RD15].

In Eq. (5) such an intensity offset correction would be represented by an additional term on the right hand side:

$$\ldots + \frac{S_{\text{off}}}{E_0(\lambda)} \cdot \sum_{m=0}^{n_{\text{off}}} c_m \lambda^m \tag{11}$$

with fit parameters c_m and S_{off} a suitable scaling factor which has the unit of the irradiance E_0; in most applications $n_{\text{off}} = 0$ or 1 in case an intensity offset is included. (Note that the NO_2 slant column retrieval algorithm of OMI (OMNO2A) is not able to handle such an intensity offset correction.)

The possibility of an intensity offset correction has been implemented in the TROPOMI NO_2 slant column processor, but this option is currently turned off as (i) it has not been fully tested yet, (ii) we would first like to understand the physical meaning and implications of such a correction term, and (iii) we need to investigate whether it might be relevant for TROPOMI NO_2 retrievals. For a first discussion see Van Geffen et al. [2020], based on which an intensity offset correction will not be included in the regular TROPOMI NO_2, also because instrumental effects such as straylight and dark current are corrected for in the spectral calibration in the Level 0-to-1b processor (Kleipool et al. [2018]; Ludewig et al. [2020]).

6.3 Separation of stratospheric and tropospheric NO_2

The baseline method for the TROPOMI NO_2 algorithm to separate the stratospheric and tropospheric contribution to the NO_2 total slant columns is by data assimilation of slant columns in the TM5-MP CTM [Williams et al., 2017]. KNMI has considerable experience with this method [Dirksen et al., 2011], and in the absence of collocated independent (e.g. limb) information on stratospheric NO_2, we consider this to be the most viable method to distinguish stratospheric from tropospheric NO_2. This approach explicitly accounts for chemistry and dynamics in the stratosphere.

The central idea of the data assimilation is to regularly update a CTM simulation of the three-dimensional, coupled troposphere-stratosphere NO_2 distribution with available measurement data in such a way that the CTM simulation of the stratospheric NO_2 column achieves close agreement with the TROPOMI slant columns over areas known to have little or no tropospheric NO_2. The assimilation effectively relies on slant columns observed over regions where the model predicts the NO_2 column to be dominated by stratospheric NO_2 (e.g. over the remote oceans). For those regions and times, the modeled slant column, i.e. the inner product of the observation operator **H** and the simulated vertical distribution $\vec{x}$, is effectively forced to the observed state. For regions and times where the model predicts large tropospheric contributions, the slant column is not a good proxy for stratospheric NO_2, and the analysis adjustment is only very small. Because total reactive nitrogen (NO_y) is a well-conserved quantity in the stratosphere, with relatively small source and sink contributions, the information from the observations can be stored in the model over long time periods. The stratospheric wind will transport the stratospheric analysis results from the oceans and remote regions to the polluted areas.

The assimilation scheme is based on the Kalman filter technique, with a prescribed parameterisation of the horizontal correlations between forecast errors. The assimilation time step in the model is 30 minutes. A full orbit of TROPOMI observations is analysed simultaneously by the Kalman filter. This is done in order to avoid discontinuities in the analysis that may occur at the location where the orbit is divided. The mid-time of the orbit is used to determine the model time step of the analysis. The analysed profile field $\vec{x}_a$ is the 3D model field of NO_2 including both troposphere and stratosphere, and is calculated from the forecast $\vec{x}_f$ and the satellite superobservations $\vec{y}$ by:

$$\vec{x}_a = \vec{x}_f + \mathbf{P}\mathbf{H}^T(\mathbf{H}\mathbf{P}\mathbf{H}^T + \mathbf{R})^{-1}(\vec{y} - \vec{y}_f) \tag{12}$$

with matrix **H** the observation operator, **P** the forecast error covariance matrix, and **R** the combined observation and representativeness error covariance (Eskes et al. [2003]; Dirksen et al. [2011]). The superobservations are constructed by averaging the observations and averaging kernels over each $1^\circ \times 1^\circ$ model grid cell [Boersma et al., 2016]. The term $\mathbf{P}\mathbf{H}^T(\mathbf{H}\mathbf{P}\mathbf{H}^T + \mathbf{R})^{-1}$ determines the weight given to the observations depending on the uncertainty of the observation versus the uncertainty of the model forecast. The departure $(\vec{y} - \vec{y}_f)$ is the difference between observed and forecasted model column (observation minus forecast). The ratio between analysis and forcast following from the Kalman equation is also applied to species that are chemically closely related to NO_2 in the stratosphere, i.e. NO, NO_3, N_2O_5 and HNO_4 [Dirksen et al., 2011].

A simplified modelling of the observation error is introduced [Dirksen et al., 2011], with a fixed small error attached to the stratospheric part of the slant column (where the AMF is well known) and a large error attached to the tropospheric contribution to the slant column (where the AMF is uncertain). These uncertainties (0.2 and 6.0×10^{15} molec/cm^2 for the stratosphere and troposphere, respectively; both numbers refer to the total slant column divided by the geometric AMF, defined by Eq. (19)) are fixed and have been optimised with sensitivity runs in such a way that the impact of major source regions on the analysis is minimal, and the forcing over clean regions is strong and consistent with observation-minus-forecast statistics.

The observation operator **H** is a combination of a horizontal interpolation and the application of the averaging kernel [Eskes and Boersma, 2003], an n_l-element vector that contains the sensitivity of TROPOMI to NO_2 in each model layer. The scalar product of the observation operator vector and the model NO_2 profile at the location of the individual TROPOMI observations yields the slant column that would be observed by TROPOMI. To further speed up the analysis step by about a factor of 8, we assimilate only half of the superobservations,

those grid cells with $i+j=$ even, where i and j are the longitude and latitude indices of the TM5-MP grid (the "checkerboard" approach). $\vec{y}_f$ is the model forecast of the superobservations, given by $\mathbf{H}\vec{x}_f$.

We use the TM5-MP CTM (Williams et al. [2017]; see also Huijnen et al. [2010a]; Huijnen et al. [2010b]; [ER15]) for the assimilation of TROPOMI NO_2 slant columns. This is a major improvement over the DOMINO v2 data assimilation systems operated at KNMI for GOME, SCIAMACHY, OMI, and GOME-2, which use an older version of the TM CTM (TM4; e.g. Dentener et al. [2003]). The main advantage of the transition to TM5-MP is the better spatial resolution ($1^\circ \times 1^\circ$), updated information on (NO_x) emissions, and an improved description of relevant physical (photolysis rate constants) and chemical (reaction rate constants) processes in that model [Williams et al., 2017]. The assimilation system operates at a resolution of $1^\circ \times 1^\circ$ (longitude $\times$ latitude), with n_l sigma pressure layers up to 0.1 hPa in the vertical direction. TM5-MP uses forecast and analysed 3-hourly meteorological fields from the European Centre for Medium Range Weather Forecast (ECMWF) operational model. These fields include global distributions of wind, temperature, surface pressure, humidity, (liquid and ice) water content, precipitation and surface parameters.

Once the TROPOMI slant columns have been assimilated, the integral from the layer above the tropopause to the upper TM5-MP layer provides the stratospheric slant column that can be isolated from the total slant column, giving the tropospheric slant column (cf. Sect. 6.4):

$$N_{\mathrm{s}}^{\mathrm{trop}} = N_{\mathrm{s}} - N_{\mathrm{s}}^{\mathrm{strat}} \tag{13}$$

For the tropopause definition the WMO-1985 temperature gradient criterion is followed, but other definitions would not lead to significantly different results (e.g. Bucsela et al. [2013]). NO_x has a C-shape profile and the air around the tropopause has only a small contribution to the total column. Compared to the QA4ECV processing of OMI a new routine has been introduced for TROPOMI as of data version 1.2.0 which reduces the fine-scale jumps in tropopause level.

The TM5-MP model provides the following information, necessary for the subsequent processing in the calculation of the AMF (see Sect. 6.4) needed for the conversion of the tropospheric slant column to the tropospheric vertical column and the final NO_2 data product (see Sect. 6.6):

- the stratospheric slant and vertical columns: $N_{\mathrm{s}}^{\mathrm{strat}}$ and $N_{\mathrm{v}}^{\mathrm{strat}}$
- an estimate of the error on the stratospheric vertical column: $\Delta N_{\mathrm{v}}^{\mathrm{strat}}$
- the NO_2 profile: $v_{l,\mathrm{NO_2}}$, with l the index for layer number $1,2,\ldots,n_l$ – this is represented by $\vec{x}_f$ in Eq. (12)
- the temperature profile at the layers: T_l^{TM5}, for $l=1,2,\ldots,n_l$
- the pressure level coefficients: A_l^{TM5}, B_l^{TM5}, for $l=0,1,\ldots,n_l$
- the index of the pressure level of the tropopause: $l_{\mathrm{tp}}^{\mathrm{TM5}}$
- the surface elevation and pressure: $z_{\mathrm{s}}^{\mathrm{TM5}}$ and $p_{\mathrm{s}}^{\mathrm{TM5}}$, at the $1^\circ \times 1^\circ$ model resolution

Note that the model divides the atmosphere in n_l layers. The pressure level coefficients determine the pressure at the n_l+1 levels separating the layers: $p_l = A_l^{\mathrm{TM5}} + B_l^{\mathrm{TM5}} \cdot p_{\mathrm{s}}$, for $l=0,1,\ldots,n_l$, with p_{s} the surface pressure for the given TROPOMI ground pixel. The pressure for the layer l, for which the concentration (volume mixing ratio) $v_{l,\mathrm{NO_2}}$ and the temperature T_l^{TM5} are given, is then midway between the level pressures p_{l-1}^{TM5} and p_l^{TM5}. The layer with index $l_{\mathrm{tp}}^{\mathrm{TM5}}$ contains the tropopause.

6.3.1 Stratospheric chemistry in the TM5-MP model

TM5-MP is primarily a tropospheric chemistry model [Williams et al., 2017]. NO_x-O_x-HO_y chemical processes are implemented according to the Carbon Bond 05 (CB05) chemistry scheme, which includes non-methane hydrocarbons to account for loss by reactions with OH [Williams et al., 2017]. Because the chemistry version of TM5-MP does not simulate N_2O, the actual source of NO_x to the stratosphere, NO_x is derived from simulated HNO_3 concentrations, which follow climatological HNO_3:O_3 ratios observed by ODIN between 2 hPa and 60 hPa [Maasakkers et al., 2013] and the multi-sensor reanalysis of stratospheric O_3 columns [Van der A et al., 2015] with climatological ozone profile shapes. In this way the model partly compensates for the biases that occur due to the missing N_2O source globally, and the missing reactions involving halogens which are important in the polar vortex. During the QA4ECV project, the representation of stratospheric NO_y in the model has been improved by nudging ODIN HNO3:O3 ratios, leading to more realistic NO_2 concentrations in the free-running mode. These improvements are applied to TROPOMI as well.

Processes included in the TM5-MP tracer evolution are advection, convection, diffusion, photolysis and deposition. Rapid changes in stratospheric NO_2 due to e.g. sudden stratospheric warmings or changes in the vortex edge location are largely accounted for through the use of the ECMWF analysis. Solar proton events are not included in the model, but the related biases are largely removed by the assimilation. NO_x emissions are

based on the RETRO-REAS emission inventories for 2006. For more details, the reader is referred to Dirksen et al. [2011].

For QA4ECV and for TROPOMI the original implementation of the stratospheric climatologies has been improved by a better interpolation to the TM5-MP vertical levels and by adding an extra nudging to NOx observations from HALOE in the upper stratosphere above 1 hPa which is not well constrained by HNO_3 [Grooß and Russell, 2005].

The data assimilation provides a regular update of the TM5-MP simulation, with a time step of 30 minutes, of the NO_2 distribution in the atmosphere on the basis of available observations: if NO_2 slant columns are available with a measurement time within 15 minutes of the model time, the model field is updated, i.e. the forecast TM5-MP state is adjusted towards the observations. The stratospheric error estimate is based on "observation minus forecast" statistics (over relatively unpolluted areas) in the assimilation. Our experience with NO_2 data assimilation using GOME, SCIAMACHY, OMI, and GOME-2 in TM has shown that the model chemistry responds smoothly to the updates forced by the satellite measurements.

Fig. 8 provides an example of the "observation minus forecast" (O–F) and the model forcing ("analysis minus forcast", A–F) for TROPOMI data of 1 April 2018. The difference between the two panels of Fig. 8 illustrates the effect of the assimilation: considerable O–F differences, resulting mostly from (anthropogenic) tropospheric NO_2 sources, have only a minor influence on the analysis. On the other hand, synoptic-scale structures in O–F persist in the A–F differences. That the A–F differences are much smaller (generally less than $\pm 0.15\times10^{15}$ molec/cm^2) than the O–F differences (up to $\pm 1.0\times10^{15}$ molec/cm^2) in particular over polluted regions like China, Europe and the USA, demonstrates that most tropospheric contributions are effectively discounted by the assimilation procedure.

As of TROPOMI NO_2 product v1.2.0 several improvements have been included. The TM5-MP model was upgraded to the latest version, including some bug fixes. In the TM5-MP model the photolysis for SZA $> 85^\circ$ was improved, impacting in particular the stratospheric NO_2 columns at high latitudes. Furthermore the assimilation of NO_2 observations is now restricted to the ascending part of the orbit, which is especially important during the spring-summer months (June-July). These changes have improved the retrieval for high SZA and in the polar regions (see Fig. 9).

6.4 Air-mass factor and vertical column calculations

The TROPOMI NO_2 algorithm uses as default pre-calculated air-mass factor look-up tables to convert the slant columns into meaningful vertical columns [Lorente et al., 2017]. The AMF, denoted by the symbol M, is the ratio of the slant column density of the absorbing trace gas along the (slant) optical path from sun to satellite, and the vertical column density above the point at the surface area the satellite is viewing. The total vertical column density then follows from the retrieved total slant column density:

$$N_\mathrm{v} = N_\mathrm{s}/M \tag{14}$$

The AMF depends on the vertical profile shape of the trace gas and can be written as (Palmer et al. [2001]; Eskes and Boersma [2003]):

$$M = \frac{\sum_l m_l\, v_l\, c_l}{\sum_l v_l}\,, \qquad m_l \equiv \delta N_\mathrm{s}/\delta v_l \tag{15}$$

with m_l the altitude-dependent AMFs or box AMF (see Sect. 6.4.1) that describe the vertically resolved sensitivity to NO_2, v_l the column density in layer l, and c_l the temperature correction term discussed below (see Sect. 6.4.2) for layer $l = 1, 2, \ldots, n_l$ [Boersma et al., 2004]. The altitude-dependent AMFs depend on retrieval (forward model) parameters, including the satellite viewing geometry, as well as surface albedo and surface pressure, cloud fraction, and cloud pressure.

The TM5-MP assimilation of the total slant columns (N_s) leads to an estimate for the stratospheric vertical profile shape with a stratospheric column amount ($N_\mathrm{v}^\mathrm{strat}$) in close agreement to TROPOMI as shown in Fig. 8. Summation over the layers above the tropopause level ($l > l_\mathrm{tp}^\mathrm{TM5}$) to top-of-atmosphere ($l = n_l$) and multiplication with the box AMF provides the stratospheric AMF, from which the stratospheric slant column ($N_\mathrm{s}^\mathrm{strat}$) can then be calculated:

$$N_\mathrm{s}^\mathrm{strat} = N_\mathrm{v}^\mathrm{strat} * M^\mathrm{strat} = \sum_{l=l_\mathrm{tp}^\mathrm{TM5}+1}^{n_l} m_l\, v_l\, c_l \tag{16}$$

Note that there is a fundamental difference between N_v and $N_\mathrm{v}^\mathrm{strat}$. The total column N_v is a satellite-observed quantity, related to the true profile shapes through the averaging kernel. In contrast, the stratospheric column $N_\mathrm{v}^\mathrm{strat}$ is a model quantity, the direct sum of the model layer subcolumns from the tropopause to the top of the

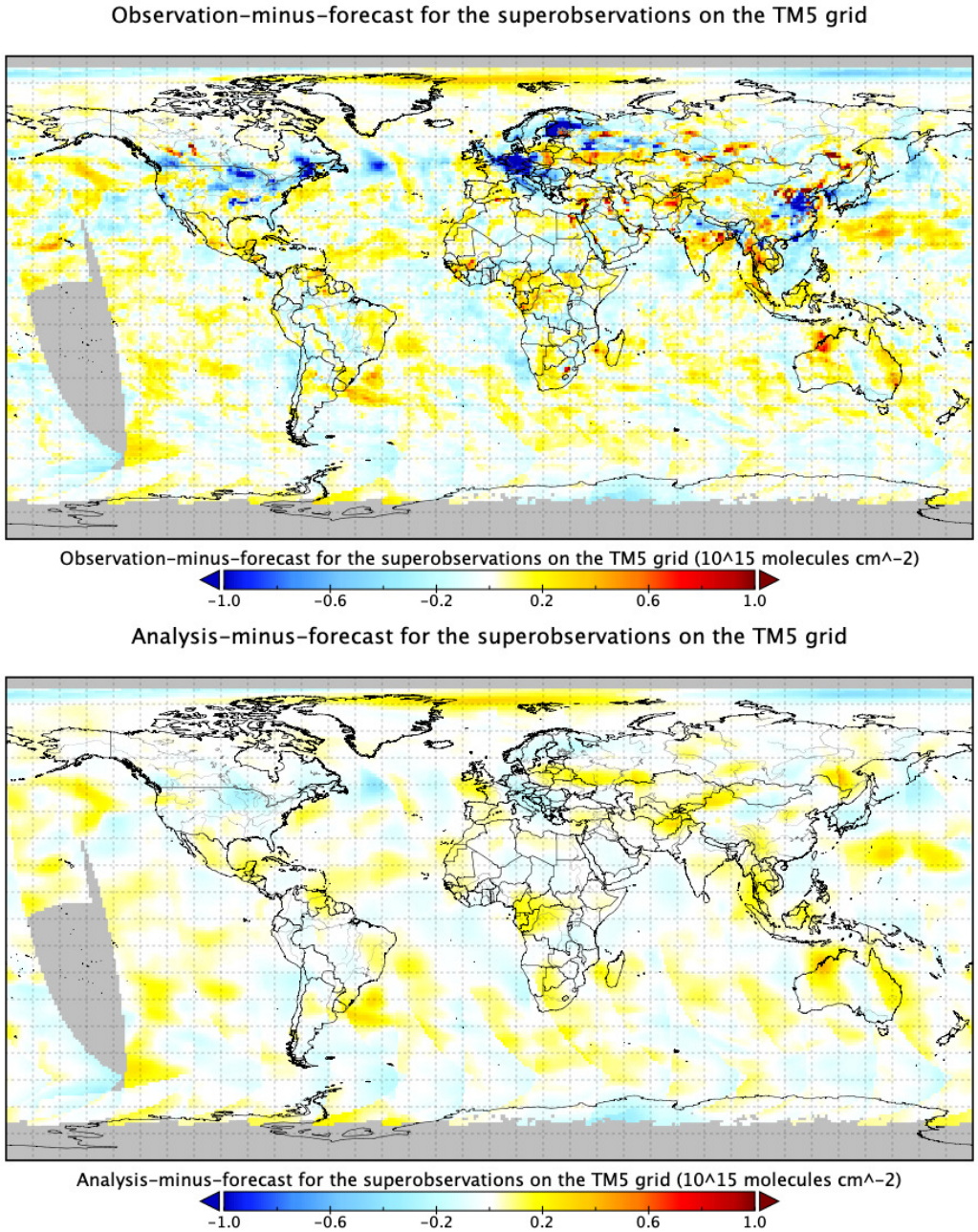

Figure 8: Observation-minus-forecast (O–F, *top panel*) and analysis-minus-forecast (A–F, *bottom panel*) differences in NO_2 slant columns divided by the geometric AMF (Eq. (19)), for 1 April 2018 processed with version 1.2.0. The observations are averaged to "superobservations" on the $1^\circ \times 1^\circ$ grid of the TM5-MP model. The model forecast is simulating the observations using the kernels and air-mass factors. The O–F demonstrates clear differences (dark-blue and bright-red spots) between the model forcast and TROPOMI concerning the fine-scale distribution of tropospheric pollution. The A–F plot shows that the assimilation hardly changes the tropospheric distribution, but efficiently updates the stratospheric fields over the more unpolluted regions like the oceans.

atmosphere. A comparisons of $N_{\mathrm{v}}^{\mathrm{strat}}$ with an other model or a profile measurement should therefore *not* make use of the averaging kernels!

Subtracting $N_{\mathrm{s}}^{\mathrm{strat}}$ from the total slant column and using the tropospheric AMF, determined by adding up the layers from the surface ($l = 1$) up to and including the tropopause level ($l = l_{\mathrm{tp}}^{\mathrm{TM5}}$) in Eq. (15), then gives the tropospheric vertical column:

$$N_{\mathrm{s}}^{\mathrm{trop}} = N_{\mathrm{s}} - N_{\mathrm{s}}^{\mathrm{strat}} \qquad \Rightarrow \qquad N_{\mathrm{v}}^{\mathrm{trop}} = N_{\mathrm{s}}^{\mathrm{trop}} / M^{\mathrm{trop}} \tag{17}$$

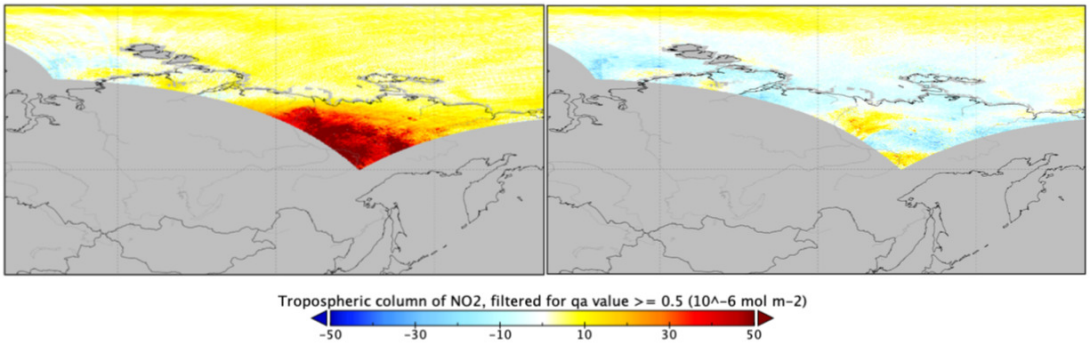

Figure 9: NO_2 tropospheric column retrievals for the descending part of TROPOMI orbit 3623, 25 June 2018, 19h UTC, over Siberia. Version 1.0.2 is shown on the left, and version 1.2.0 on the right. Prominent unrealistic positive biases are observed in v1.0.2 and v1.1.0 for the highest solar zenith angles on the left side of the orbit, while v1.2.0 has much more realistic values close to zero with a tendency towards a weak negative bias.

Over clean areas like the oceans, the retrieved (small) tropospheric column is the result of the subtraction of two large numbers, the total and stratospheric column, both with their own uncertainty. A large number of negative column values are therefore expected in those regions, reflecting the retrieval uncertainties in the total and stratospheric column. For space or time averaging and for comparisons with models (including data assimilation) it is essential that the negative values are included. Removing them, or putting them to zero will lead to a positive bias in the tropospheric column over clean regions.

Note that the total vertical column N_v in Eq. (14) is *not* the same as sum of the partial vertical columns:

$$N_\mathrm{v}^\mathrm{sum} \equiv N_\mathrm{v}^\mathrm{trop} + N_\mathrm{v}^\mathrm{strat} \neq N_\mathrm{v} \tag{18}$$

Our best physical estimate of the NO_2 vertical column at any given place is the sum $N_\mathrm{v}^\mathrm{sum}$. Users who, for example, wish to assimilate NO_2 total columns should, however, use the total column N_v for this. The total column N_v depends strongly on the modelled ratio of the stratospheric and tropospheric sub-columns, a dependency which is partly removed in the summed product. For data assimilation use is made of the averaging kernels, and in this way the resulting analyses are not dependent on the a-priori (including the ratio of the model tropospheric and stratospheric column).

In the absence of atmospheric scattering and in a plane-parallel atmosphere, a so-called geometric AMF, denoted by M^geo, can be defined by way of a simple function of the solar zenith angle θ_0 and of the viewing zenith angle θ:

$$M^\mathrm{geo} = \frac{1}{\cos\theta_0} + \frac{1}{\cos\theta} \tag{19}$$

This quantity is used in the criteria for the `qa_value` (see App. E) but not written to the output data product. The ratio

$$N_\mathrm{v}^\mathrm{geo} = \frac{N_\mathrm{s}}{M^\mathrm{geo}} \tag{20}$$

is the geometric column density (GCD), to distinguish it from the vertical column densities computed using AMFs that contain model information [Van Geffen et al., 2020]. As of v2.6.0 the NO_2 $N_\mathrm{v}^\mathrm{geo}$ is available in the output data product, where the precision of $N_\mathrm{v}^\mathrm{geo}$ simply is the precision of the N_s divided by the M^geo (cf. Table 6).

6.4.1 Altitude dependent AMFs

The altitude-dependent AMFs, or vertical sensitivities, have been calculated with a radiative transfer model by adding a small, optically thin amount of NO_2 to the model atmosphere layer l for an atmosphere that is otherwise devoid of NO_2, and subsequently ratioing the excess NO_2 slant column (simulated with a radiative transfer model) to the vertical column added to that layer ($m_l = \delta N_\mathrm{s}/\delta v_l$) [Lorente et al., 2017]. The model atmosphere does not include aerosols and describes the Earth's surface as a Lambertian reflector.

As radiative transfer model we use the Doubling-Adding KNMI (DAK) radiative transfer model (De Haan et al. [1987]; Stammes [2001]), version 3.2, which has the possibility to include a pseudo-sphericity correction. The radiative transfer calculations takes the sphericity of the atmosphere into account, with Rayleigh scattering (including multiple scattering effects) and polarisation correction included (see Boersma et al. [2011] and

references therein); this includes a simple sphericity correction based on detailed comparisons between DAK and McArtim as described in Lorente et al. [2017]. The DAK model atmosphere consists of a Lambertian surface albedo, and an adjustable number of atmospheric layers. Atmospheric data are from the standard AFGL midlatitude summer profile. We calculate the AMF at 437.5 nm, near the middle of the spectral fitting window, for the corresponding TROPOMI NO_2 slant column retrievals; this is a suitable choice for both the small ($425-450$ nm) and wide ($405-465$ nm) fit windows, as demonstrated in the QA4ECV-project ([RD6], [ER7], see document [RD15]).

The altitude-dependent AMFs are stored in a look-up table (LUT) as a function of solar zenith angle (θ_0), viewing zenith angle (θ), relative azimuth angle (ϕ_{rel}), Lambertian surface albedo (A_s), surface pressure (p_s), and (mid-level) atmospheric pressure (p_l). This 6-dimensional LUT is extended with more reference points compared to earlier versions in order to respect the increase in variability of TROPOMI retrieval parameters (coarser OMI pixels have less variability in spatially smeared surface albedo and surface pressure values than TROPOMI) and to minimise interpolation errors when looking up the appropriate altitude-dependent AMF. Pixel-specific altitude-dependent AMFs are obtained by using the best estimates for forward model parameters and a 6-D linear interpolation scheme.

Table 5 gives an overview of the reference points for the quantities that make up the 6 dimensions. The dimensions for the LUT are chosen to balance sufficiently accurate 6-dimensional linear interpolation with computational efficiency and resource economy. For out-of-bounds values (there is a slight chance that this occurs for surface pressure or atmospheric pressure) we use the point nearest to the LUT reference point. In the current OMI NO_2 data product only ground pixels with $\theta_0 < 80^\circ$ ($\cos(\theta_0) = 0.174$) are used in the conversion to vertical columns. For TROPOMI and future OMI NO_2 data products the slant to vertical column conversion will not be limited in terms of θ_0; in practice this means the range will be the same as for the FRESCO cloud retrieval: $\theta_0 < 88^\circ$ (i.e. $\cos(\theta_0) = 0.035$), hence the lower limit of $\cos(\theta_0)$ of 0.03 in Table 5. (For practical implementation purposes the LUT contains the altitude-dependent air-mass factor scaled with the geometric AMF, v_l/M^{geo}, rather than v_l directly.)

The TROPOMI `qa_value` (see App. E) indicates that observations with $\theta_0 > 81.2$ should not be used. Experience has shown that observation-minus-forecast differences increase rapidly above this point.

6.4.2 Temperature correction

For the TROPOMI NO_2 retrieval, a temperature correction is applied in the air-mass factor step (see Eq. (15)). The NO_2 cross-sections used in the DOAS retrieval, taken from Vandaele et al. [1998] [ER14], are valid for NO_2 at a temperature of 220 K. The temperature at which the NO_2 cross-section is evaluated does significantly influence the fit: amplitudes of the differential NO_2 absorption features decrease with increasing temperature, while the overall shape of the differential cross-section is in good approximation independent of temperature.

To account for the temperature sensitivity, a correction factor has been determined for the difference between the effective temperature of the NO_2 (which is derived from the ECMWF temperature profile and the modelled profiles in the data assimilation system) and the temperature of the cross-section, where the temperature dependence is assumed to be linear. For layer l of the NO_2 profile the correction factor c_l is

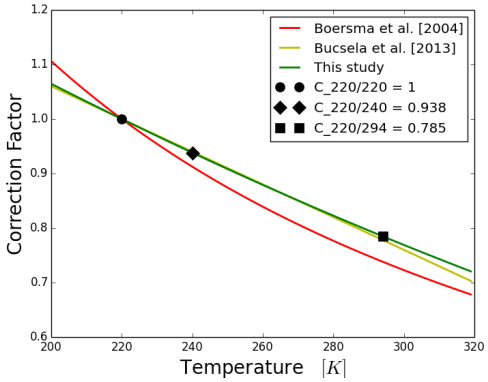

Figure 10: Temperature correction factors used in OMI NO_2 algorithms from [RD16] (green line), Bucsela et al. [2013] (yellow line), and from Boersma et al. [2004] (red line) as a function of temperature. Source: [RD16].

Table 5: Quantities and their reference points in the AMF look-up table to be used in the TROPOMI NO_2 data processing to convert the tropospheric slant column into the tropospheric vertical column. The lower limit of $\cos(\theta)$ in the list is related to the maximum value of θ for TROPOMI, which is 72° (as for OMI).

Quantity	Number of reference points	Values at reference points
Solar zenith angle $\cos(\theta_0)$	17	1.00, 0.95, 0.90, 0.80, 0.70, 0.60, 0.50, 0.45, 0.40, 0.35, 0.30, 0.25, 0.20, 0.15, 0.10, 0.05, 0.03
Viewing zenith angle $\cos(\theta)$	11	1.00, 0.95, 0.90, 0.80, 0.70, 0.60, 0.50, 0.45, 0.40, 0.35, 0.30
Relative azimuth angle $180^\circ - \lvert\phi - \phi_0\rvert$	10	0°, 20°, 40°, 60°, 80°, 100°, 120°, 140°, 160°, 180°
Surface albedo A_s	26	0.00, 0.01, 0.02, 0.03, 0.04, 0.05, 0.06, 0.07, 0.08, 0.09, 0.10, 0.12, 0.14, 0.16, 0.18, 0.20, 0.25, 0.30, 0.35, 0.40, 0.50, 0.60, 0.70, 0.80, 0.90, 1.00
Surface pressure p_s [hPa]	14	1048, 1036, 1024, 1013, 978, 923, 840, 754, 667, 554, 455, 372, 281, 130
Atmospheric pressure p_l [hPa]	174	1054.995, 1042.82, 1030.78, 1018.89, 1007.13, 995.51, 984.0309, 972.67, 961.45, 950.35, 939.39, 928.55, 917.84, 907.24, 896.71, 886.24, 875.88, 865.65, 855.54, 845.54, 835.67, 825.90, 816.26, 806.72, 797.12, 787.47, 777.93, 768.51, 759.21, 750.01, 740.93, 731.96, 723.09, 714.33, 705.65, 697.04, 688.54, 680.14, 671.85, 663.65, 655.56, 647.56, 639.66, 631.86, 624.07, 616.30, 608.62, 601.03, 593.54, 586.15, 578.85, 571.63, 564.51, 557.48, 550.44, 543.39, 536.43, 529.56, 522.77, 516.08, 509.47, 502.9492, 496.50, 490.14, 483.75, 477.32, 470.97, 464.71, 458.53, 452.44, 446.42, 440.49, 434.63, 428.86, 423.12, 417.42, 411.80, 406.26, 400.79, 395.39, 390.07, 384.82, 379.64, 374.52, 369.43, 364.37, 359.37, 354.44, 349.57, 344.78, 340.05, 335.38, 330.78, 326.24, 321.70, 317.15, 312.66, 308.24, 303.89, 299.59, 295.35, 291.18, 287.06, 283.00, 261.31, 225.35, 193.41, 165.49, 141.03, 120.12, 102.68, 87.82, 75.12, 64.30, 55.08, 47.20, 40.535, 34.79, 29.86, 25.70, 22.14, 19.08, 16.46, 14.20, 12.30, 10.69, 9.29, 8.06, 6.70, 6.11, 5.37, 4.70, 4.10, 3.57, 3.12, 2.74, 2.41, 2.12, 1.87, 1.65, 1.46, 1.29, 1.141, 1.01, 0.89, 0.79, 0.69, 0.61, 0.54, 0.48, 0.42, 0.37, 0.33, 0.29, 0.23, 0.18, 0.13, 0.10, 0.07, 0.05, 0.04, 0.030, 0.020, 0.014, 0.0099, 0.0066, 0.004471, 0.002997, 0.002005, 0.001352, 0.0009193, 0.0006300, 0.0004387, 0.000307

[RD16]:

$$c_l = 1 - 0.00316(T_l - T_\sigma) + 3.39\times10^{-6}(T_l - T_\sigma)^2 \tag{21}$$

with T_l and T_σ the temperature of the profile layer and cross-section, respectively. The function in Eq. (21) is an update w.r.t. the correction used for the OMI NO_2 data in DOMINO v2 (Boersma et al. [2002], Boersma et al. [2004], Bucsela et al. [2013]) – see Fig. 10. Note that the temperature sensitivity given in the above equation is determined for the default wavelength window $405-465$ nm used for the fit; depending on the fit window and on TROPOMI's spectral resolution details, the function may need to be adapted.

6.4.3 Correction for cloud cover

The AMF formulation accounts for cloud-contaminated pixels. Following Martin et al. [2002] and Boersma et al. [2002], the independent pixel approximation (IPA) is used to express the AMF as a linear combination of a cloudy AMF (M_{cld}) and a clear-sky AMF (M_{clr}), both for the total column and the tropospheric column:

$$M = w_{\text{NO}_2} M_{\text{cld}} + (1 - w_{\text{NO}_2}) M_{\text{clr}} \ , \qquad M^{\text{trop}} = w_{\text{NO}_2} M_{\text{cld}}^{\text{trop}} + (1 - w_{\text{NO}_2}) M_{\text{clr}}^{\text{trop}} \tag{22}$$

with w_{NO_2} the radiance weighted cloud fraction (or: cloud radiance fraction), which depends on the effective cloud fraction (f_{eff}):

$$w_{\text{NO}_2} = \frac{f_{\text{eff}} I_{\text{cld}}}{R_{\text{TOA}}} = \frac{f_{\text{eff}} I_{\text{cld}}}{f_{\text{eff}} I_{\text{cld}} + (1 - f_{\text{eff}}) I_{\text{clr}}} \tag{23}$$

where I_{cld} is the radiance from the cloudy part of the pixel, I_{clr} the radiance from the clear part of the pixel, and R_{TOA} the total scene radiance at top-of-atmosphere. The NO_2 column below the clouds, i.e. the TM5-MP NO_2 profile integrated from the surface to the cloud pressure level, is called the ghost column ($N_{\text{v}}^{\text{ghost}}$). Both I_{cld} and I_{clr} depend on the viewing geometry, the assumed (cloud) albedo, the surface pressure and the cloud pressure, following from the FRESCO algorithm (Sect. 6.4.4). In the DOMINO v2 and TM4NO2A processing of data from OMI, GOME-2 and their predecessors, these radiances were calculated following the analytical approach of Vermote and Tanré [1992], using f_{eff} from the cloud retrieval process for the same instrument. For TROPOMI, the cloud (radiance) fraction is determined from the radiance in the NO_2 fit window using LUTs, as detailed below (Sect. 6.4.4; see also App. C).

6.4.4 Cloud cover and cloud pressure data

The large spectral range covered by TROPOMI offers multiple wavelength windows where information on the cloud height may be derived, including the O_2 A-band [Wang et al., 2008], the O_2 B-band [Desmons et al., 2019] and the O_2–O_2 absorption feature at 477 nm [Veefkind et al., 2016]. The OMI spectral range does not cover the A- and B-band, and most retrievals make use of the O_2–O_2 absorption. Because of the strong absorption with enhanced sensitivity for high clouds, and long experience with cloud retrievals for the SCIAMACHY and GOME-2 instruments, it was decided to use the O_2 A-band as default for the cloud pressure retrieval for TROPOMI, using the FRESCO algorithm. This choice is a major difference between OMI and TROPOMI and has a significant impact on the retrieved NO_2 tropospheric columns. The FRESCO+ algorithm (Wang et al. [2008]; [RD17]) retrieves cloud information from the O_2 A-band around 758 nm: the cloud fraction and the cloud pressure, for all satellite ground pixels with solar zenith angle $\theta_0 < 88^\circ$.

Due to the high spectral resolution of TROPOMI compared to GOME-2, the FRESCO+ algorithm needed to be re-written and the corresponding lookup tables have been generated once more. The result, called FRESCO-S (short for FRESCO-Sentinel), is used for the TROPOMI NO_2 product and will be used for other Sentinels as well. FRESCO-S is described in the Sentinel-5 ATBD [RD18], which is not yet publicly available.

The FRESCO-S algorithm was used up to processor version 1.3.x. As of version 1.4.0 a first improvement, nicknamed FRESCO-wide, was implemented, and a further major improvement ("two-band FRESCO") was implemented in version 2.8.0; these improvements are desribed in Sect. 6.4.4.2. The general name "FRESCO" is used below, unless a specific version is referred to.

The surface albedo database that is used by the FRESCO algorithm is based on GOME-2 observations [Tilstra et al., 2017] at 758 and 772 nm up to version 2.3.1 and since version 2.4.0 on the TROPOMI-based DLER climatology [Tilstra et al., 2021]; see Sect. 6.4.5

6.4.4.1 The FRESCO-S cloud pressure & NO_2 cloud fraction

FRESCO does not provide the geometric cloud fraction but rather a radiometric equivalent cloud fraction: an effective cloud fraction, f_{eff}, that results in the same top-of-atmosphere (TOA) radiance as the real cloud, assuming an optically thick Lambertian cloud with a fixed albedo of $A_{\text{c}} = 0.8$ (which may be adapted in case of very bright scenes) at the cloud pressure level, p_{c}. This approach has proven to be useful for trace gas retrievals; see Wang et al. [2008], who evaluated this for ozone and NO_2.

Because of the large difference in wavelength between the O_2 A-band and the NO_2 retrieval window, the cloud fraction retrieved by FRESCO in the O_2 A-band may not be exactly representative for the cloud fraction in the NO_2 window, although Van Diedenhoven et al. [2007] found that cloud parameters retrieved from UV and O_2 A-band measurements showed good consistency for cloud fractions > 0.2; for mostly clear skies, FRESCO provides somewhat higher cloud fractions than UV-based retrievals. For small cloud fractions

the O_2 A-band retrieval becomes sensitive to errors in the surface albedo climatology used, especially over the bright vegetation. In addition, a misalignment between ground pixel field-of-view of the VIS and NIR bands [RD4], containing the NO_2 retrieval window and the O_2 A-band, respectively, exists for the TROPOMI measurements.

For these reasons, the baseline option for the TROPOMI NO_2 retrieval is to (i) use the cloud pressure p_c from FRESCO and (ii) retrieve the cloud fraction and cloud radiance fraction from the NO_2 spectral window itself at 440 nm. The latter is done by fitting the continuum reflectance at 440 nm to a simulated reflectance constructed with the independent pixel approximation and radiative transfer calculations for the clear-sky and cloudy-sky part of the pixel, using the appropriate surface albedo in that spectral window, $A_{s,NOtwo}$, as forward model parameter. Here $A_{s,NOtwo}$ is taken from the albedo climatology (cf. Sect. 6.4.5) at 440 nm, interpolated linearly in time, and using nearest neighbour sampling in latitude and longitude.

The continuum reflectance at 440 nm could be determined from the observed spectrum, averaged over a small wavelength interval, but that may lead to unexpected values, e.g. in case of spikes in the measurement or missing wavelength pixels. Instead, as of v1.4.0 [Van Geffen et al., 2022], the modelled reflectance of Eq. (5) is evaluated at $\lambda_{c,NO_2} = 440$ nm, without taking the absorbing trace gases into account: $R_{TOA}(\lambda) = P(\lambda) \cdot (1 + C_{ring})$, where the C_{ring} term is included because Rayleigh scattering is a combination of elastic Cabannes scattering and inelastic Raman scattering without the spectral structures of the latter. The trace gas absorption is not taken into account here because the reflectance LUT used for the determination of the cloud fraction does not include trace gas absorption either. This reflectance-based approach to determine the cloud fraction in the NO_2 window is very similar to FRESCO and explicitly accounts for Rayleigh scattering and involves the calculation of LUTs with the TOA reflectance at 440 nm as a function of viewing geometry, surface/cloud albedo, and surface/cloud pressure. See App. C for details on the cloud fraction retrieval.

With processor version 1.3.0 some improvements were made in the FRESCO-S algorithm and in the way the FRESCO results are treated in the NO_2 algorithm. Previously in FRESCO the surface albedo from the database was used without modifications other than snow or ice at the surface (see Sect. 6.4.5 and App. D). In the updated version the surface albedo is reduced to match the top-of-atmosphere reflectance in case the top of atmosphere reflectance is lower than expected for the climatological surface albedo (see Sect. 6.4.5 and App. C.1). Before the update these cases would lead to negative cloud fractions and unrealistic cloud pressures. Another change in FRESCO is the treatment of very high cloud fractions. If the scene albedo indicates an elevated scene height and a scene albedo higher than 0.8, the parameters from the scene retrieval are used: the cloud fraction is set to 1, the cloud albedo is set to the scene albedo and the cloud pressure is set to the scene pressure. This prevents odd behaviour for scenes with cloud fraction $f_{eff} > 1$. Care has been taken to not use this for snow scenes.

6.4.4.2 Cloud pressure: the FRESCO-wide and two-band FRESCO updates

Early studies of the TROPOMI NO_2 retrieval indicated that the cloud pressures produced by FRESCO-S show a positive bias (of order 50 hPa) in cases where either low clouds are expected (e.g. low clouds and fog over ocean near the coast) or locations with thick aerosol layers, like often observed over Eastern China. The NO_2 retrieval is very sensitive to a positive bias in the cloud pressure in combination with cloud radiance fractions close to 0.5. This will result in large AMF values and thus in underestimations of the tropospheric column. Comparisons between TROPOMI and OMI-QA4ECV NO_2 tropospheric columns have shown that NO_2 data versions 1.2.x and 1.3.x are substantially lower than OMI-QA4ECV, while the slant columns are in good agreement. The main difference between these retrievals is the cloud pressure retrieval.

For processor version 1.4.0 an update of FRESCO-S was introduced [Van Geffen et al., 2022]. The new scheme, called FRESCO-wide, makes use of the longer wavelength part of the O_2 A-band. The wavelength ranges in FRESCO-wide are $758 - 759$ nm, $760 - 761$ nm and $765 - 770$ nm. The inclusion of the weaker absorption lines in the latter window mainly impacts the lower clouds, generally increasing the cloud height, i.e. decreasing the cloud pressure. In those cases the differences are typically in the order of 50 hPa. For high clouds both FRESCO versions deliver very similar cloud heights on average.

A close inspection of the FRESCO-wide algorithm as part of the Sentinel-5 project revealed that the spectral noise provided to the OE inversion code was incorrect: instead of the *absolute* noise, the *relative* noise was provided. Using the correct noise calculation was implemented in version 2.6.0, which led to significantly higher cloud pressures, i.e. clouds closer to the surface. This change, however, had a significant adverse impact on the NO_2 product and in version 2.7.1 the change was rolled back.

In order to correctly handle the noise without disturbing the NO_2 retrieval, further improvements in the FRESCO-wide algorithm were necessary. The basis for this step is the notion that the scene model in the algorithm, which retrieves the scene pressure p_{sc} and the scene albedo A_{sc}, should return a scene pressure

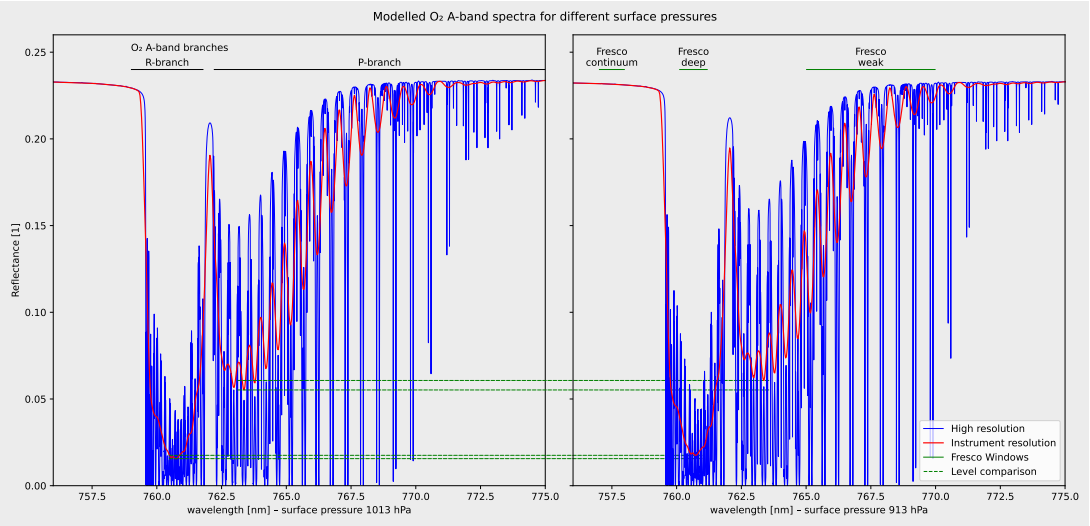

Figure 11: Simulated spectra of the O_2 A-band for two scenes: a cloud-free scene with surface pressure at 1013 hPa (*left panel*) and surface pressure at 913 hPa (*right panel*). The so-called R- and P-branch of the O_2 A-band are indicated in the left panel, while the three FRESCO-wide retrieval bands are indicated at the top in the right panel. The widening of the FRESCO-weak band to $765-770$ nm was introduced in version 1.4.0 to make better use of the weaker absorption lines. In the two-band FRESCO retrieval the FRESCO-deep band at $760-761$ nm is omitted. In the R-branch, the difference between the two scenes is very small because the scene is quite dark (low reflectance) and therefore a small error in the R-branch will have a significant impact on the retrieved scene pressure. The difference between the two scenes is large enough in the P-branch for a reliable retrieval.

which approaches within error bars the surface pressure p_s in case of cloud-free observations and small cloud fractions, which consitute the most important use cases for NO_2 retrievals.

Various settings were tested, including the use of a noise floor (if the SNR is higher than a configurable threshold, the noise is calculated using the noise floor value). Rather than the original three-band approach, a two-band retrieval turned out to give the best results: the R-branch of the O_2 A-band is skipped, because small errors in the measured reflectance give rise to large errors in the retrieved scene pressure, as is shown in Fig. 11.

In the operational processor both the cloud pressure p_c and scene pressure p_{sc} are clipped to physical values, i.e. that both are not larger than the surface pressure p_s. For the investigation discussed here this check and clipping of the results has been disabled.

The top panel of Fig. 12 shows that even for a strick cloud filtering the "old" (v2.4.0) noise calculation in combination with the original three-band retrieval gives scene pressures that can be up to 400 hPa from the surface for sea/ocean pixels, about 11% of the retrievals the scene pressure lies below the surface, and the mean pressure difference is 92 ± 107 hPa.

The middle panel of Fig. 12 shows that using the correct noise calculation in combination with the original three-band retrieval results in the scene pressure falling below the surface for almost half of the retrievals. This is what one expects if the surface is actually detected, but the distribution is still rather wide, a-symmetric, and differs between land, sea and glint pixels. The long positive tail for ocean/sea pixels has improved, linked to the radiance noise correction. The mean pressure difference is 20 ± 79 hPa and for about half of the retrievals the scene pressure lies below the surface. (Presented is the case without a noise floor; introducing a noise floor does not significantly change the results.)

The bottom panel of Fig. 12 shows that the distribution becomes much more peaked, with about a third of the retrieved scene pressures ending up below the surface and a mean scene pressure of 17 ± 51 hPa, when the the R-branch of the O_2 A-band is omitted from the retrieval, i.e. when only two bands in the "continuum" and the "weak bands" in the P-branch are used.

Fig. 13 shows an example of $p_s - p_{sc}$ pressure difference over snow/ice scenes in winter. The average pressure difference of about 50 hPa in v2.4.0 (left panel) is reduced to about 20 hPa in v2.8.0 (right panel). Due to the large apparent difference between these pressures in the versions before v2.8.0, the `qa_value` threshold to identify cloud-free scenes over snow/ice (App. E, Table 21, rule 12) was set to $(p_s - p_{sc})/p_s > 0.96$ (v2.4.0) and 0.94 (v2.7.1). Given the large improvement due to the two-band FRESCO retrieval in the surface

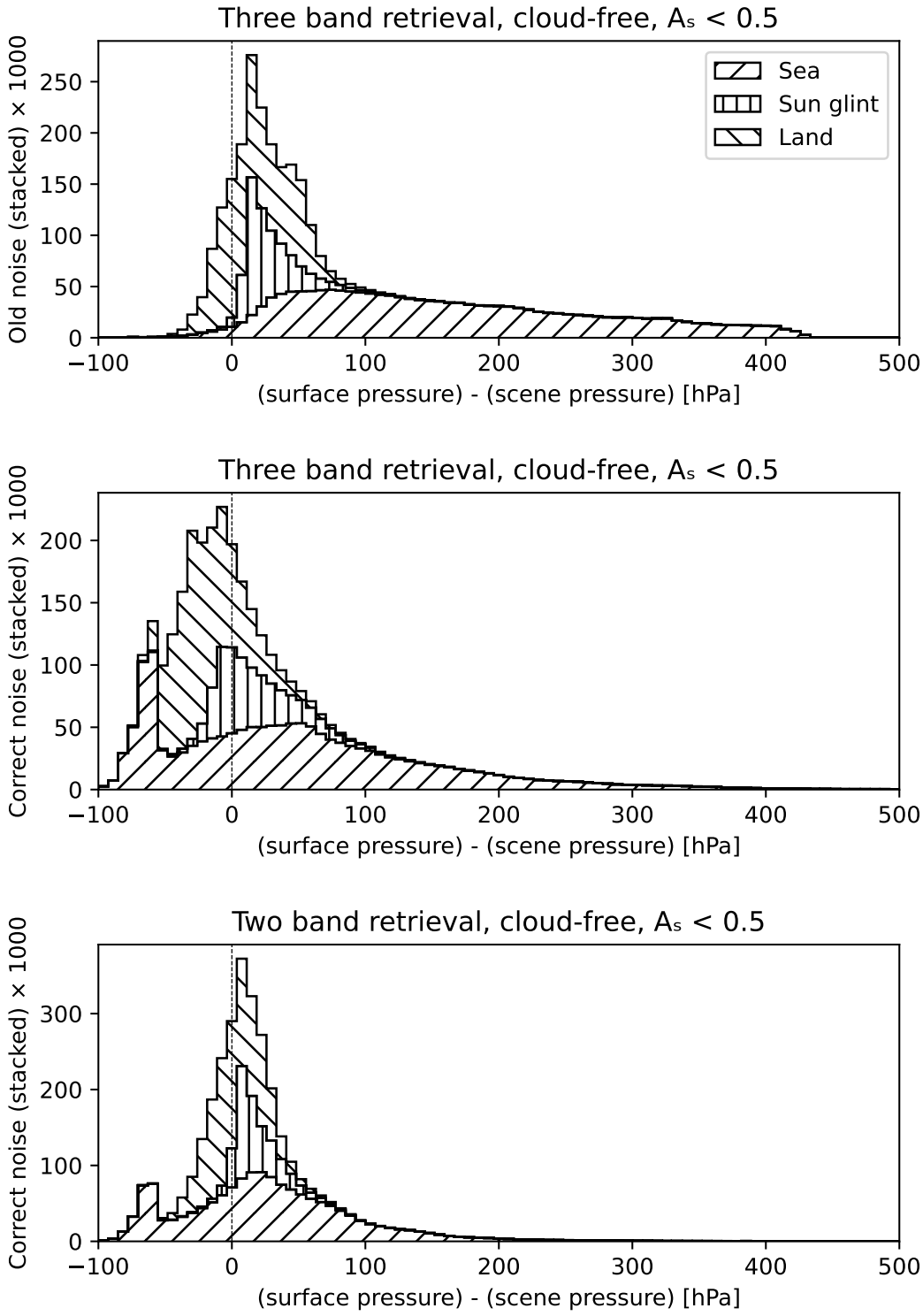

Figure 12: Stacked histograms of the retrieved cloud-free scene pressures over sea, sun glint and land for the "old" (v2.4.0) noise calculations and the three-band retrieval (*top panel*), for the correct noise calculations and the three-band retrieval (*middle panel*), and for the correct noise calculations and the new two-band retrieval (*bottom panel*). A strict cloud filtering was applied based on VIIRS colocated observations, keeping only fully cloud-free pixels with cloud fraction $< 0.05\%$; the Suomi NPP-VIIRS instrument provides measurements about 3–5 minutes ahead of TROPOMI. Data are from 16 consecutive orbits (22992–23007) of 22 March 2022; the number of observations used is 3.3 million.

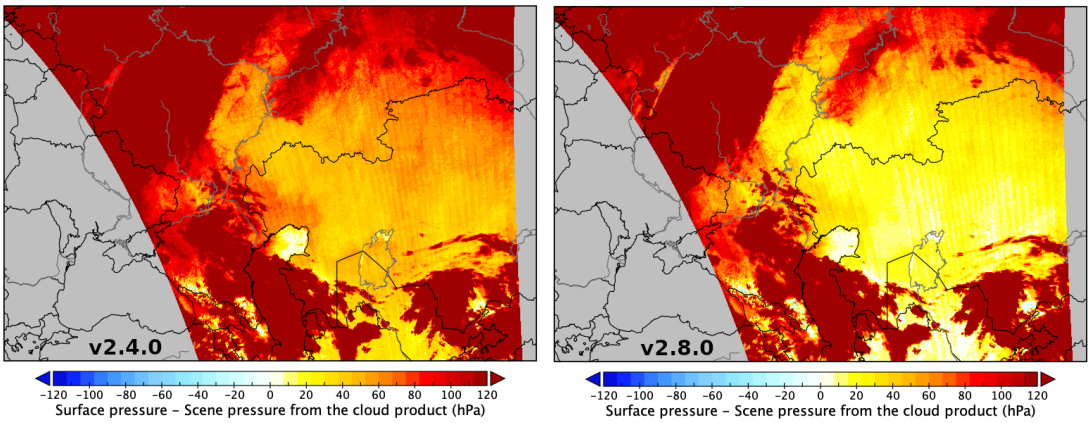

Figure 13: Difference between the surface pressure and the scene pressure in the FRESCO cloud product of v2.4.0 (*left panel*) and of v2.8.0 (*right panel*). Data is from orbit 16244 of 1 Dec. 2020, an orbit covering Western Asia and Russia. Central Kazakhstan is covered with snow on this day, while the area north-west and east of the Caspian Sea is snow-free. The cloud-free snow-covered region in Kazakhstan shows an average pressure difference of about 50 hPa for v2.4.0, improved to about 20 hPa in v2.8.0.

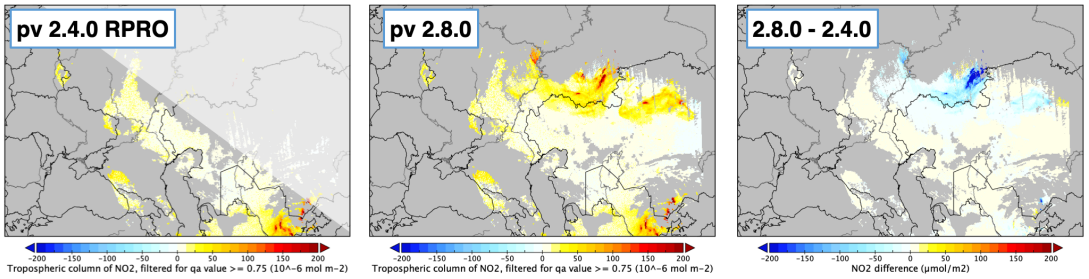

Figure 14: Tropospheric NO_2 values (in μmol/m^2) filtered for a `qa_value` > 0.75 for the same overpass as Fig. 13 over Western Asia on 1 Dec. 2020. The snow-covered area is roughly indicated by the white-transparent triangle in the left panel. The conservative filtering in v2.4.0 (*left panel*) removes most of these snow pixels, while v2.8.0 (*middle panel*) labels many of these pixels as good quality (cloud-free). The difference in tropospheric column between the two versions (*right panel*) shows a reduction of about 50% for emission areas (red spots in middle panel) for this overpass.

and scene pressure differences, the threshold is tightened to 0.97 for v2.8.0. The new FRESCO retrieval and threshold lead to many more pixels to be accepted over snow/ice, as shown in Fig. 14. Importantly, the smaller pressure difference results in larger air-mass factors and reductions of the tropospheric NO_2 column of about 50% over pollution hotspots with snow/ice. In other months, for snow-free areas over industrialised areas, small positive and negative differences are observed for pixels with a small positive cloud fraction (`qa_value` > 0.75).

In summary, the FRESCO two-band retrieval in v2.8.0 shows an improved consistency with the surface pressure. Since the NO_2 retrieval is especially sensitive to the pressure of low (boundary layer) clouds, we anticipate that the two-band approach potentially also improves NO_2. But the changes are subtle and more detailed studies are needed to prove this.

The R-branch of the O_2 A-band shows a very strong absorption by oxygen and is therefore sensitive to calibration issues (e.g. straylight) as well as the representation of the saturated lines in the FRESCO retrieval. This may explain the benefit of removing this branch. But also the simple FRESCO cloud model may play a role in the sensitivity to including the R-branch. Further improvements may be obtained by finetuning the wavelength range of the FRESCO-weak band. The impact on the high clouds should be studied as well.

6.4.4.3 The O_2–O_2 cloud pressure

The O_2–O_2 cloud pressure retrieval used for the OMI NO_2 retrievals [Veefkind et al., 2016] has been ported to TROPOMI and is included in the operational software since version 2.2.0. The Level-2 NO_2 product files

are extended with two separate groups for the cloud retrievals, one containing the FRESCO results taken from the seprate FRESCO support product files, and one containing the O_2–O_2 retrieval datasets. The cloud data is derived from the O_2–O_2 slant column density retrieved in the wavelength window $460 - 490$ nm with a DOAS approach similar to the NO_2 retrieval (Sect. 6.2), with the model function formulated in Eq. (5) and using cross-sections $\sigma_k(\lambda)$ for O_2–O_2, NO_2 and ozone.

The air mass factors in version 2.2.0 are computed solely using the FRESCO-wide cloud pressures (Sect 6.4.4.2). For a later NO_2 data release we will study the quality of both cloud products and rules will be developed to use one or the other cloud product depending on under which circumstances they work best, which will be then described in a future update of this ATBD.

6.4.4.4 Other cloud data products

Apart from the FRESCO and O_2–O_2 support cloud products, TROPOMI cloud parameters are provided by an algorithm developed at DLR ([RD19], available via [ER1]). Once the validity and reliability of this cloud data product is established, its cloud parameters will be tested in the NO_2 processor and the results will be compared to the results found with FRESCO, O_2–O_2 and other cloud data.

Cloud parameter retrieval similar to FRESCO in the O_2 A-band [Wang et al., 2008] can also be done in the the O_2 B-band [Desmons et al., 2019], which has the advantage of a smaller albedo over vegetation. We plan to also test whether these cloud products may be useful for the NO_2 retrieval.

6.4.5 Surface albedo

6.4.5.1 Processor versions v1.0.2 up to v2.3.1

The baseline surface albedo climatology for TROPOMI NO_2 retrievals for processor versions v1.0.2 up to v2.3.1 is the OMI database, aggregated to a grid of $0.5^\circ \times 0.5^\circ$; see Kleipool et al. [2008], which describes a climatology made from 3 years of OMI data. Meanwhile the climatology has been improved by using 5 years of data, based on the the same method [ER16]. This 5 years based climatology (version 3) has been used for the DOMINO v2 and QA4ECV OMI NO_2 retrievals, and is also used for the TROPOMI NO_2 retrievals, where the "mode LER" is used. For the surface albedo in the NO_2 window, A_{s,NO_2}, the 440 nm data is used. The climatological value of the surface albedo are adapted in case the snow/ice flag (cf. Sect. 6.4.6) indicates there may be substantial differences in albedo; see App. D for some details on this correction.

The OMI albedo climatology was chosen because of its spectral coverage in the NO_2 fit region, its relatively high spatial resolution, and the seamless transition between land and sea. The OMI albedo guarantees a consistency between TROPOMI and OMI NO_2, since it is also used in the QA4ECV data product Boersma et al. [2018]. An additional advantage is that the OMI climatology has been derived from observations taken at similar local times and under similar viewing conditions as for the TROPOMI observations.

The Kleipool surface albedo climatology is based on OMI data, which does not cover the near-infrared wavelengths in use by the FRESCO algorithm to derive cloud properties (Sect. 6.4.4). Instead, the surface albedo database that is used by the FRESCO algorithm up to version 2.3.1 is based on GOME-2 observations [Tilstra et al., 2017] at 758 and 772 nm, given at $0.25^\circ \times 0.25^\circ$ resolution. The relatively coarse spatial resolution of GOME-2 measurements underlying the climatology and the fact that the overpass time of the OMI measurements used for the Kleipool climatology is quite similar to the overpass times of TROPOMI (i.e. the measurements are taken under similar viewing geometries), while the overpass time of GOME-2 is several hours earlier, are in favour of our choice for the Kleipool surface albedo climatology for the NO_2 retrieval, and for our choice to determine the cloud fraction in the NO_2 window.

Taking the anisotropic properties of the surface reflectance (so-called BRDF effects) into account was not implemented in the TROPOMI NO_2 retrieval algorithm up to version 2.3.1. Accounting for BRDF in OMI NO_2 retrievals has a generally small effect ($< 5\%$) with substantial effects only occurring at extreme viewing angles at high solar zenith angles [Zhou et al., 2010]. Developments in generating improved surface albedo data are described for instance from the ADAM ([RD14], Sect. 6.1) and QA4ECV ([RD6], [ER7]) projects, and the recent work by Vasilkov et al. [2017].

An alternative approach is to make use of the MODIS geometry-dependent surface Lambertian equivalent reflectivity. This was used to generate version V4.0 of the NASA standard NO_2 product from OMI [Lamsal et al., 2021]. Recently, it was shown by Loyola et al. [2020] how an effective geometry-dependent Lambertian equivalent reflectivity may be derived from the TROPOMI data.

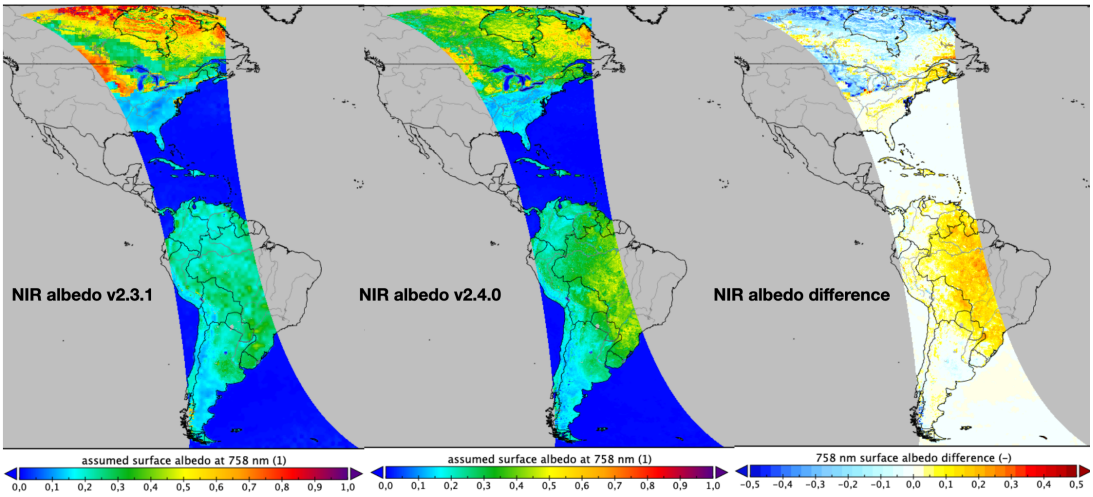

Figure 15: An example of the TROPOMI DLER v1.0 computed for January (orbit 21896, 3 Jan. 2022) at 758 nm in the near infrared, relevant for the FRESCO cloud retrieval. The central panel shows the TROPOMI DLER used in v2.4.0, and is compared to the GOME-2 LER used in v2.3.1 and older versions of the NO_2 retrieval. The difference is shown in the right panel. The TROPOMI DLER v2.1 is very similar to v1.0 in the NIR spectral range.

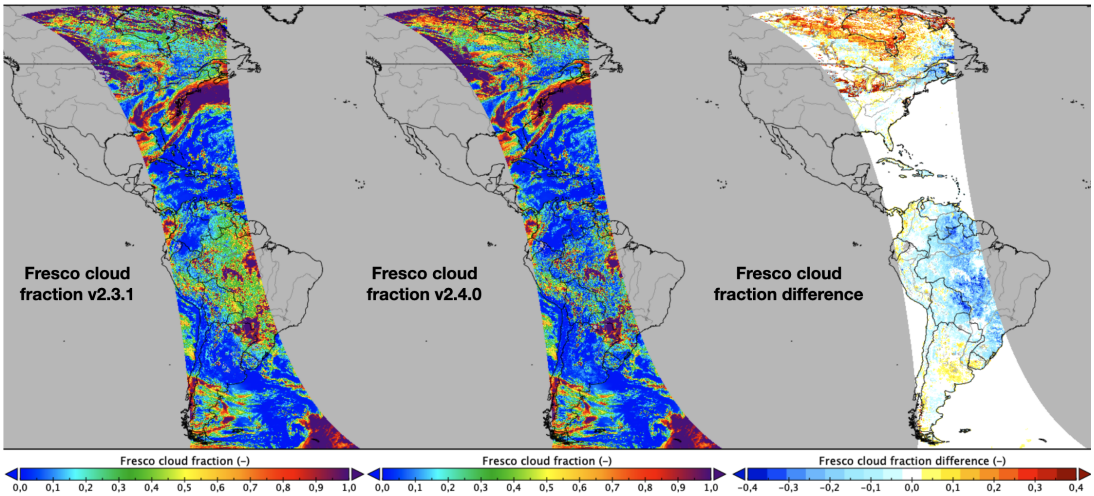

Figure 16: FRESCO-wide cloud fraction for processor version 2.3.1 (*left panel*) with the GOME-2 LER and version 2.4.0 (*middle panel*) with the TROPOMI DLER. The difference is shown in the right panel. Data is shown for orbit 21896 of 3 January 2022, passing over South America.

6.4.5.2 Processor version v2.4.0 and following

A directional surface albedo climatology, also referred to as a directional LER or DLER, for GOME-2 was developed by Tilstra et al. [2021]. Following the same approach, the author developed first a DLER v1.0 [RD20] based on 3 years TROPOMI Level-1b v1.0 measurements, which was followed by a DLER v2.1 (Tilstra et al. [2024]; [RD21]) based on 5 years TROPOMI collection 3 Level-1b measurements (which includes an improved radiance and irradiance product with degradation correction) and has better defined flagging for snow/ice cases (Sect. 6.4.6). The most recent TROPOMI DLER dataset, along with documentation and validation report, is available from the TEMIS website at [ER17].

NO_2 processor versions 2.4.0-2.6.0, operational since mid July 2022, made use of DLER v1.0 and that version was also used for a full mission reprocessing with processor version 2.4.0. Processor version 2.7.1, operational since mid June 2024, makes use of DLER v2.1.

The DLER is available for 21 selected wavelength bands in the full data range $328 - 2314$ nm and can therefore be applied consistently to both the FRESCO cloud retrieval and the NO_2 retrieval in the $405 - 465$ nm window. The resolution of the DLER dataset is $0.125^\circ \times 0.125^\circ$ globally, which is a major improvement compared

to the previously used LER products for OMI or GOME-2 (Sect. 6.4.5.1). The viewing-angle dependence is parameterised using a third order polynomial, and the four coefficients, together with the mean LER determine the DLER (see [RD21]).

An example of the implemented DLER is shown in Fig. 15. Most striking are the high albedo values at the East side over the Amazon region in Brazil. This East-West asymmetry reflects a real property of the vegetation and is missing in the GOME-2 LER. Fig. 16 shows the impact of the replacement of the GOME-2 LER by the TROPOMI DLER. Especially over vegetation/forest we expect major scattering angle (viewing-angle) dependencies of the LER. This was not accounted for in the GOME-2 LER used previously, leading to uniform high biases in the cloud fraction in especially the East part of the TROPOMI swath. In the figure we observe an offset in the cloud fractions of around $0.2 - 0.3$ over Brazil for v2.3.1. With the new TROPOMI viewing-angle dependent DLER we find also a realistic fraction of cloud-free footprints, as expected. Due to the small pixel size and short revisit time of TROPOMI we can see that over Canada and the USA the albedo map is less influenced by snow at the surface. The big improvement in spatial resolution is also clearly demonstrated by these maps, for instance over mountain ranges.

The impact of replacing the OMI and GOME-2 LER by the TROPOMI DLER is shown in Fig. 17. For September 2020 we find relatively minor differences over Europe and the US. More major changes are found over the rain forests in Brazil and Central Africa, as well as in the South of China. These are regions where the directionality of the LER is large in the NIR spectral range. Especially in Brazil we observe major increases in the column up to 10^{15} molec/cm^2 related to changes in the FRESCO cloud pressure. Note that changes in albedo are partly compensated for in the NO_2 retrieval though the cloud (fraction) retrieval and by applying albedo adjustments (see below), which may explain the smaller impacts over Europe and the US.

The TROPOMI DLER v2.1 is introduced in processor version 2.7.1. In the NO_2 fitting window the v2.1 DLER is systematically lower than the v1.0 DLER by roughly 0.01, see Fig. 18. This systematic lowering of the albedo affects the tropospheric NO_2 column over polluted regions, which are now systematically higher by about 10%.

One more major change in processor version 2.x.y compared to version 1.x.y is in the albedo treatment. As mentioned above, the cloud fraction and cloud radiance fraction are retrieved from the NO_2 fit window. In version 1.x the cloud fractions are clipped to the $[0, 1]$ interval before the AMF is computed.

As of version 2.x the albedo is adjusted if the cloud retrieval would give a cloud fraction outside the $[0, 1]$ interval to ensure radiative closure [Van Geffen et al., 2022], which implies that the cloud radiance fraction w_{NO_2}, defined in Eq. (23), lies within $[0, 1]$ as well. In v2.4.0-v2.6.0 w_{NO_2} values larger than 1 where sometimes encountered; in v2.7.1 this coding issue is repaired.

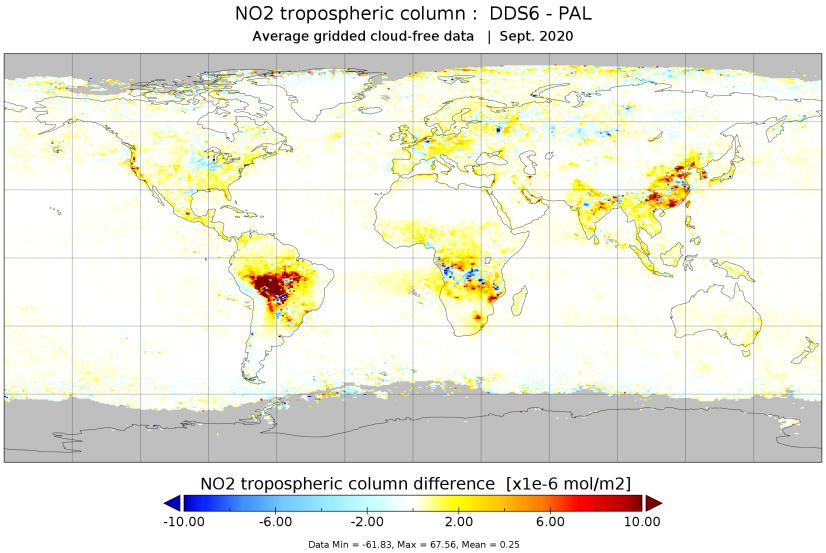

Figure 17: The difference in tropospheric NO_2 column between the test dataset (named DDS6) for processor version 2.4.0, which uses the TROPOMI DLER v1.0 database, and the S5P-PAL reprocessed datasets [ER18] based on version 2.3.1, which uses the OMI LER in the NO_2 fit window and the GOME-2 LER for the FRESCO cloud retrieval in the NIR. Note that 10^{15} molec/cm^2 corresponds to about 16 μmol/m^2. Data is gridded and averaged for September 2020.

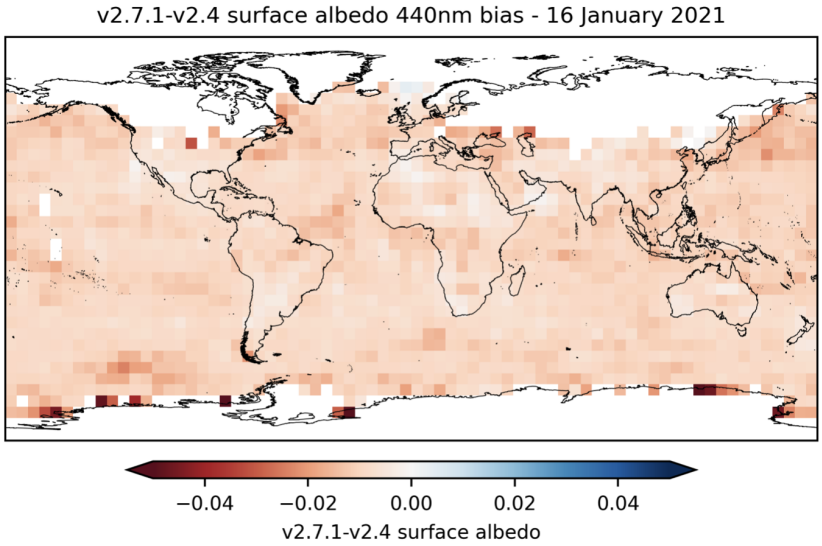

Figure 18: Difference in surface albedo for TROPOMI DLER v2.1 and v1.0, sampled at the TROPOMI pixels on 16 January 2021, and gridded to 5x5 degree averages. The new v2.1 albedo is systematically lower than v1.0 by about 0.01 for all seasons.

The process is the following: when the reflectivity is lower than expected based on the surface albedo climatology, then the albedo is adjusted to match the observations, see App. C.1. The adjusted albedo is written to the Level-2 output file, replacing the climatology. This albedo is subsequently used to compute the (tropospheric) AMF. Because the albedo is lowered by this process, the AMF is lower and the approach leads to increased tropospheric NO_2 columns.

The same approach is also applied for very bright scenes, but now the cloud albedo is adjusted. In the cloud fraction retrieval the cloud albedo is fixed to 0.8. When the reflectivity is larger than expected for a fully clouded scene, the cloud albedo is increased to match the observation. The new cloud albedo is reported in the Level-2 NO_2 file.

Fig. 19 shows the impact of this procedure for one overpass over Europe. Note that pixels with a cloud cover > 0 are not affected (white parts in the figure). A lowering of the albedo is observed over most of the cloud-free pixels (white areas correspond largely to cloud fractions > 0). A lowering of the albedo by 1% may already have a significant impact on the retrieved tropospheric NO_2 column.

6.4.6 Snow and ice cover

Substantial errors are introduced if the real albedo differs considerably from what is expected from the albedo climatology, for example in the case of the sudden snowfall or ice cover. Correcting the surface albedo from the climatology (which contains a climatological snow cover) using knowledge of actual snow/ice cover will therefore improve the final data product, in terms of the retrieval itself and for flagging such cases.

In processor versions up to 2.6.0, the correction of A_{s,NO_2} followed the approach included in the OMI cloud data product OMCLDO2 [Veefkind et al., 2016] to adapt the surface albedo in the O_2–O_2 fit window (i.e. at 477 nm). As of processor version 2.7.1, the albedo correction is based on the presence of improved flagging in the v2.1 DLER albedo climatology for snow/ice cases. App. D provides some details on this correction of the surface albedo; the corrected albedo is reported in the Level-2 file.

The baseline for snow/ice cover information as of processor version v2.2.0 is the daily data provided by the ECMWF [Van Geffen et al., 2022]; up to v1.4.0 the NISE snow/ice data [ER19] was used (see also [RD1]). A feature of the NISE data is that the flag is set to 252 when the scene contains both land and water ("mixed pixels at coastlines"), which occurs frequently. In these cases there is no information on snow or ice, and (for high latitudes) the `qa_value` is set to a small value to reflect this additional uncertainty. The snow/ice information from ECMWF does not have this coastline problem. In addition, the spatial resolution of the ECMWF data is higher than that of NISE. The ECMWF snow data [DeRosnay et al., 2015] is derived from synoptic data and from the Interactive Multi-sensor Snow and Ice Mapping System (IMS); Cooper et al. [2018] show that IMS has better agreement with in situ observations over North America and that NISE misses a significant number of snow-covered pixels. An alternative for the snow/ice cover might come from OSISAF [ER20], but

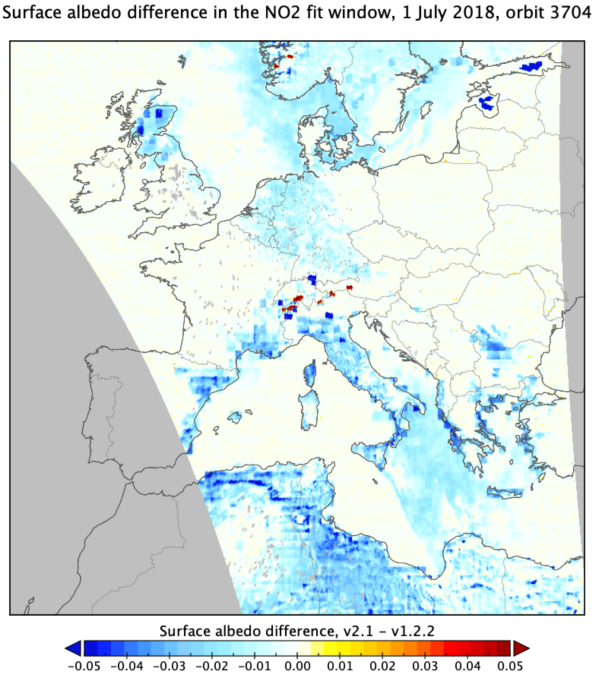

Figure 19: Difference in the surface albedo in the NO_2 fit window between v1.2.2 and v2.1.0 for orbit 3704 on 1 July 2018 over Europe. Blue colors indicate smaller albedo values in v2.1.0. The white parts correspond largely with retrieved cloud fractions > 0. The red spots over the Alps correspond to snow- or cloud-covered pixels where the albedo was increased.

implementation is not straightforward as this are currently separate products for land and for sea.

The FRESCO algorithm (Sect. 6.4.4) provides two sets of data (Wang et al. [2008]; [RD17]): (i) the effective cloud fraction f_{eff} and cloud pressure p_{c} using a cloud albedo $A_{\text{c}} = 0.8$ (this cloud albedo may adapted by FRESCO over bright scenes), and (ii) the scene albedo A_{sc} and the scene pressure p_{sc} assuming a cloud fraction $f_{\text{eff}} = 0.0$. With the snow/ice flag the NO_2 processing will select which of these two sets is used for the determination of the AMFs and subsequent vertical NO_2 columns. When the snow/ice flag indicates that there is more than a 1% snow/ice coverage, the retrieval will move to scene mode by setting the cloud radiance fraction Eq. (23) equal to 1.0. The A_{sc} and p_{sc} from FRESCO are then used to determine the effective albedo and pressure of this (ficticious) cloud. Which mode is used can be found via the selection criteria of the `qa_value` definition, listed in App. E; see also the NO_2 Product User Manual (PUM; available via [ER2]).

6.4.7 Surface pressure

The (altitude-dependent) AMFs in Eq. (15) depend on the surface pressure, p_{s}. For the TROPOMI NO_2 retrieval this information is obtained from the TM5-MP model ($1^\circ \times 1^\circ$) driven by ECMWF meteorological data. Because the TM5-MP information is representative for spatially coarse pressures, the TM5-MP results are corrected based on the method described in Zhou et al. [2009] and Boersma et al. [2011]. This correction computes a new surface pressure based on the difference between the corresponding spatially coarse terrain height and the actual, pixel-averaged terrain height based on a 3-km resolution digital elevation map (DEM) [Maasakkers et al., 2013].

6.4.8 A-priori vertical NO_2 profiles

A CTM is considered to be the best source of information for a-priori NO_2 vertical profiles. The baseline for the TROPOMI NO_2 retrieval algorithm is to use TM5-MP [Williams et al., 2017] vertical NO_2 profile shape simulated at a $1^\circ \times 1^\circ$ (longitude $\times$ latitude) spatial resolution for $n_l = 34$ layers covering troposphere and stratosphere. In future updates this layer choice may be further optimised. The a-priori profile shapes are calculated at the centre of the TROPOMI ground pixel via weighted linear interpolation based on the four nearest neighbour TM5-MP cell centres. Using TM5-MP instead of TM4 constitutes a significant improvement in itself: TM5 v3 is a benchmarked recent model version (Huijnen et al. [2010a]; Huijnen et al. [2010b]; [ER15];

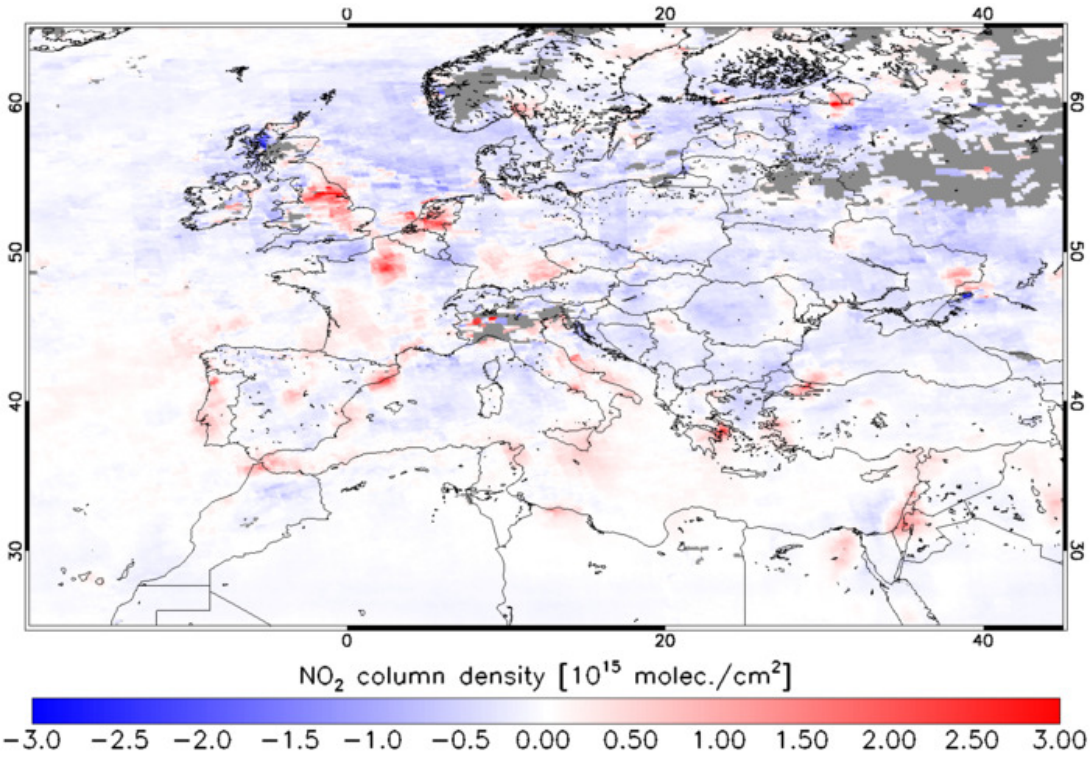

Figure 20: Tropospheric NO_2 from OMI retrieved with TM5-MP at a resolution of $1^\circ \times 1^\circ$ minus retrieved with TM5-MP at a resolution of $3^\circ \times 2^\circ$ for 20–30 October 2004 over Europe.

Williams et al. [2017]), with more up-to-date NO_x emissions (from the MACCity inventory), chemistry, and ongoing improvements of ship, soil and lightning NO_x emission descriptions.

Using TM5-MP with a global $1^\circ \times 1^\circ$ resolution is an important improvement over previous global satellite NO_2 retrievals that used vertical profile shape computed at spatial resolutions of $2^\circ \times 2.5^\circ$ or $3^\circ \times 2^\circ$ (e.g. Lamsal et al. [2010], Boersma et al. [2011]). Obviously, there are spatial gradients in NO_2 concentrations over scales smaller than a degree, but a resolution of $1^\circ \times 1^\circ$ should capture the most relevant gradients much better than a resolution of $3^\circ \times 2^\circ$. Using higher resolution models in combination with the TROPOMI averaging kernels will in effect further improve the spatial resolution in the a-priori NO_2 fields for advanced users interested in regionally focused investigations (e.g. Huijnen et al. [2010b]).

The effect of the improved spatial resolution is illustrated by Fig. 20, which shows the difference between averaged tropospheric NO_2 columns from the OMI sensor from 20–30 October 2004 retrieved with TM5 at $3^\circ \times 2^\circ$ and at $1^\circ \times 1^\circ$. The retrieval with the higher resolution profile shape leads to more pronounced contrasts between the sources of pollution and background (ventilated) pollution. To better capture the sources of air pollution is an important target of the TROPOMI mission.

6.4.9 Averaging kernels

For each ground pixel, the TROPOMI data product provides the corresponding total NO_2 column averaging kernel. The averaging kernel for DOAS retrievals is equal to the altitude-dependent AMF ratioed by the total air-mass factor [Eskes and Boersma, 2003]. Furthermore, the height-dependent air-mass factors include a term that corrects for the difference between the temperature of the cross section used in the DOAS fit and the actual temperature in a given layer [RD16] (cf. Sect. 6.4.2).

The averaging kernel as provided in the file is linked to the total column NO_2 product. The tropospheric averaging kernel is obtained by scaling the total-column kernel by M/M^{trop} (see [RD22]) and setting all elements of the kernel to zero above the tropopause layer, i.e. for $l > l_{\text{tp}}^{\text{TM5}}$. This step is explained in the Product User Manual (PUM; available via [ER2]) and has to be implemented by the user. Note that the stratospheric NO_2 column reported in the product is derived from the model after assimilation of the TROPOMI measurements. Therefore this quantity does not have a corresponding averaging kernel.

Using the averaging kernel is important for data users who wish to minimise the discrepancies between the assumptions in the TROPOMI retrieval and their application of interest, for example for validation, data assimil-

ation, or comparison to a model (e.g. Silver et al. [2013]; Boersma et al. [2016]). In particular, comparisons that make use of the averaging kernel are no longer depending on the a-priori TM5-MP profile shape [Eskes and Boersma, 2003].

The averaging kernel should be used in validation exercises, model evaluations, and assimilation or inversion attempts with TROPOMI NO_2 columns whenever possible (i.e. whenever independent profile information is available). The recipe for using the averaging kernel **A** for the purpose of obtaining a model estimate of the tropospheric NO_2 column (N_v^{trop}) that can be compared to TROPOMI is as follows:

$$N_v^{\text{trop}} = \mathbf{A}\vec{x}_m = \sum_{l=1}^{n_l} A_l S_l x_{m,l} \tag{24}$$

where S_l are the components at the l-th vertical layer of an operator that executes a mass-conserving vertical interpolation, followed by a conversion to sub-columns (molec/cm^2) in case the model vertical distribution $x_{m,l}$ is not given in those units.

Alternatively, the kernels may be used to replace the global TM5-MP a-priori profile used in the retrieval by an alternative modelled NO_2 profile shape, e.g. from a high-resolution regional chemistry-transport model (Griffin et al. [2019], Lin et al. [2014]). The recipe for this replacement is provided in the PUM [ER2].

6.4.10 De-striping the NO_2 data product

The OMI measurements show across-track biases (stripes) in NO_2 resulting from viewing zenith angle dependent calibration errors in the OMI backscatter reflectances. For the DOMINO v2 NO_2 data product, Boersma et al. [2011] developed an empirical post-hoc de-striping correction based on the daily mean across-track dependency of the NO_2 slant columns. This correction is applied in the final step of the NO_2 processing, i.e. after the conversion to vertical columns. A new de-striping approach was developed within the QA4ECV project, which is now fully integrated in the retrieval approach, avoiding the extra post-processing step.

Given that TROPOMI is measuring with a CCD detector similar to the one used by OMI, calibration related across-track biases are likely also present in the TROPOMI NO_2 data. For this reason an option has been included in the Level-2 processor that allows for a de-striping correction on the NO_2 slant column data, similar to the approach implemented for QA4ECV.

Because the striping amplitude was found to be much smaller than for OMI, the stripe correction was switched off in the first release of the TROPOMI NO_2 product, v1.0.2 and v1.1.0, of July 2018. In the first update to v1.2.0 (24 October 2018) it was however decided to turn on the de-striping to remove small but systematic across-track features and further improve the product quality in this way.

The de-striping is determined from on orbits over the Pacific Ocean (longitude between $150^\circ\text{W} - 180^\circ\text{W}$), in order to avoid interference by tropospheric pollution hotspots. Observations are averaged over a 30° latitude range in the tropical belt, which moves north-south with the seasons.

A slant column stripe amplitude is determined for each viewing angle. The row-dependent slant column difference $N_{\text{s,NO}_2}^{\text{diff}}$ is defined as the difference between the measured total slant columns ($N_{\text{s,NO}_2}$) and total slant columns derived from the model profiles ($N_{\text{s,NO}_2}^{\text{mod}}$) and the averaging kernels (**A**), averaged along-track over the 30° latitude range. The stripe amplitude ($N_{\text{s,NO}_2}^{\text{str}}$) is then computed as $N_{\text{s,NO}_2}^{\text{diff}}$ – mean($N_{\text{s,NO}_2}^{\text{diff}}$), where the mean is taken over the across-track rows. The slant columns are stripe corrected by subtracting this stripe amplitude from the individual slant column observations: $N_{\text{s,NO}_2}^{\text{corr}} = N_{\text{s,NO}_2} - N_{\text{s,NO}_2}^{\text{str}}$. The NO_2 data product file contains $N_{\text{s,NO}_2}$ and $N_{\text{s,NO}_2}^{\text{str}}$, so that a user of the slant column data can/must apply the stripe correction.

In order to retain only features which are slowly varying over time, and in order to reduce the sensitivity to features observed during a single overpass, the stripe correction factors are averaged over a time period of 7 days, or about 7 Pacific Ocean orbits. Note that at the beginning of a (re)processing, the very first $N_{\text{s,NO}_2}^{\text{str}}$ value equal zero. And in case the Pacific Ocean orbit of a given day is missing, the $N_{\text{s,NO}_2}^{\text{str}}$ remains unchanged.

The slant column stripe amplitudes, one for each viewing angle, are stored in three places:

- For off-line (OFFL) processing, in a separate daily data file which contains the stripe amplitudes determined on the previous day. This file is read during every restart of the TM5-MP/DOMINO system in order to initialise the stripe correction. These files are written during the TM5-MP/DOMINO run after every update of the stripe amplitudes, when processing a Pacific orbit.
- The stripe amplitudes are written to the NO_2 Level-2 datafiles.
- The stripe amplitudes are written to the TM5-MP output files, which are used by the near-real time (NRT) NO_2 Level-2 processor.

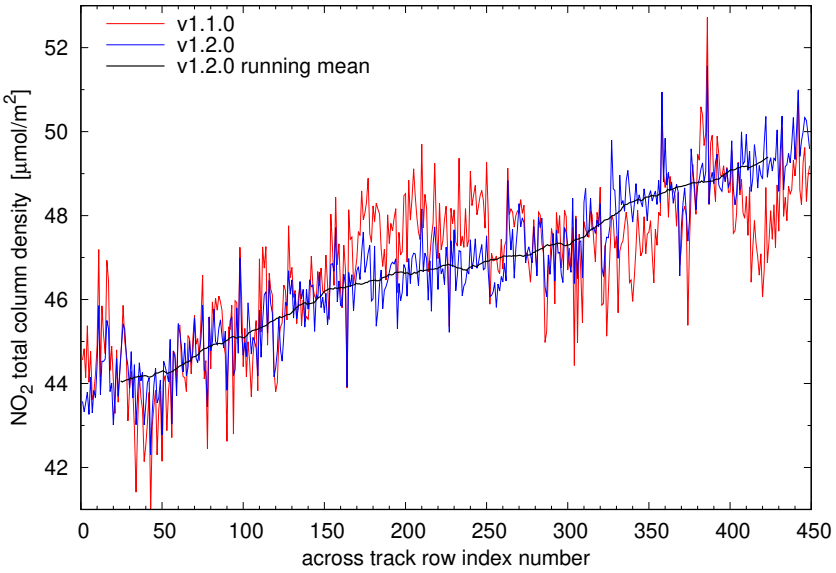

Figure 21: Comparison of the total column (i.e. stratosphere plus troposphere), averaged over the tropical Pacific Ocean on 15 July 2018 (orbit 03747) as a function of row index. The red curve is the v1.1.0 results without de-striping, the blue curve is the v1.2.0 result with the de-striping (the stripe correction is averaged over a week), and the black curve shows a 50-row running mean of the blue curve. See the text for a discussion

Fig. 21 shows an example for TROPOMI of the impact of the de-striping of the total NO_2 column (i.e. stratosphere plus troposphere), averaged over the tropical Pacific Ocean on 15 July 2018 (orbit 03747) as a function of the row index. The red curve is the v1.1.0 result without de-striping, the blue curve is the v1.2.0 result with the de-striping (the stripe correction is averaged over a week), and the black shows a 50-row running mean of the blue curve. The red curve shows single-row spikes, as well as correlated structures, such as the high values around row 200 and the low values around rows 40, 320 or 420. These correlated features are partly removed with the update of the Level 0-to-1b data to v2.0.0, in use as of NO_2 v2.2.0, but part of the structures remain unexplained. The plot shows that the stripe filtering removes the major part of both the high and low frequency variability. Note that the amplitude of the structures in the red curve is small, generally within 5% of the column over the clean Pacific Ocean. Also note that we expect an increase of the total column in the stratosphere from left to right, as indicated by the black curve, due to the diurnal cycle of stratospheric NO_x chemistry.

Fig. 22 shows a direct comparison of the NO_2 retrieval – in the form of the "geometric" vertical columns, defined as N_s/M^{geo} – of OMI and TROPOMI as reported by the DOAS fits on actual observations from both instruments. The figure demonstrates that TROPOMI and OMI retrieve roughly the same absolute retrieved NO_2 slant columns, but that TROPOMI has a much smaller across-track variation ("stripiness"). A more detailed comparison of TROPOMI and OMI slant column retrieval results is presented by Van Geffen et al. [2020].

6.5 Processing chain elements

6.5.1 Off-line (re)processing

The off-line (re)processing of the TROPOMI NO_2 retrieval algorithm, schematically displayed in Fig. 23, takes place at two locations (for more details, see [RD1]):

(1) The first step of the NO_2 processing system, illustrated in the top left part of Fig. 23, the DOAS retrieval, ingests the Level-1b spectra and is running in the PDGS TROPOMI processing system at DLR. Also performed in the PDGS, in a separate processing chain (not shown), is the FRESCO cloud retrieval (Sect. 6.4.4), needed by several Level-2 data products. The processor uses the slant column and cloud cover data to assemble a "backup" NO_2 vertical column product, based on the TM5-MP NO_2 vertical profile forecast produced for the NRT processing at the observation date (cf. Sect. 6.5.2).

(2) The NO_2 backup data product is then transferred to the IDAF at KNMI, where once a day the data of all orbits is ingested in the data assimilation / chemistry transport model TM5-MP, as illustrated in the right

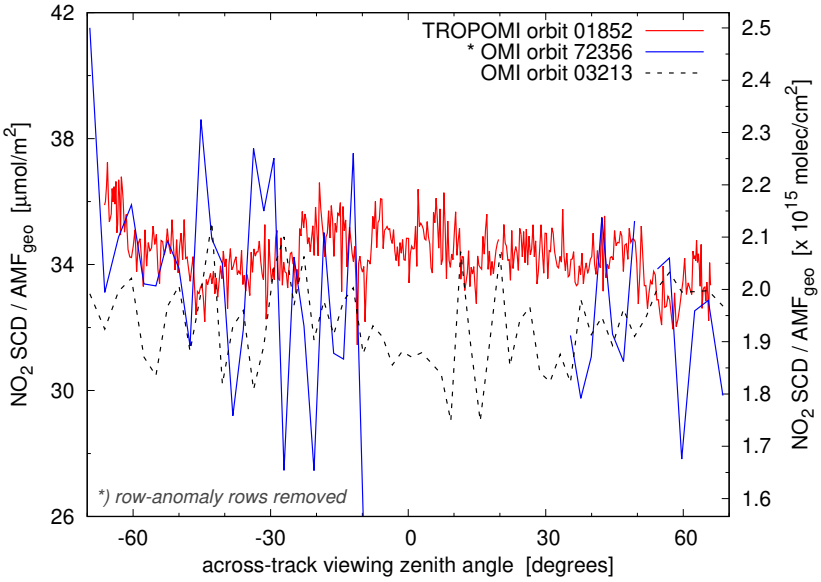

Figure 22: NO_2 "geometric" vertical column densities, defined as N_s/M^{geo}, for the Pacific Ocean orbit on 20 Feb. 2018 of TROPOMI are compared to those for the almost overlapping OMI orbit (with rows affected by the row anomaly removed) and to those of a similar OMI orbit from 20 Feb. 2005. Same data as in Fig. 27.

part of Fig. 23, to compute the off-line NO_2 product using the CTM model profiles computed with the latest ECMWF meteorological fields.

(3) The off-line or nominal NO_2 data product is then transferred back to the PDGS (bottom left part of Fig. 23), where it is made available for the users.

The motivation for this set-up is to take full advantage of the available processing elements at DLR and KNMI, and at the same time keep the number of data transfers limited. DLR will operate in the PDGS a suite of processors geared to handling large amounts of TROPOMI spectra, including the processing of NO_2 column data from TROPOMI spectra. The IDAF at KNMI hosts a complete data assimilation system based on the TM5-MP model, and has considerable experience in both the off-line and on-line retrieval of NO_2 from the GOME, SCIAMACHY, OMI, and GOME-2 instruments. The essential inputs for the processing of TROPOMI NO_2 data are (1) the Level-1b spectra measured by TROPOMI at the PDGS, and (2) the ECMWF meteo data at the IDAF.

As illustrated by Fig. 23, the data assimilation system not only provides vertical profiles for the processing of NO_2 data, but also for other TROPOMI data products: formaldehyde (HCHO) and sulphur dioxide (SO_2). Unlike NO_2, HCHO and SO_2 are not assimilated in the TM5-MP model: their profiles are output of the TM5-MP model, based on the chemistry involving these species.

6.5.2 Near-real time processing

The NRT processing of TROPOMI NO_2 is based on the same principles as the off-line processing, described in Sect. 6.5.1. The main difference between the NRT processing, depicted in Fig. 24, and the off-line processing (Fig. 23) is the timing of the data assimilation step and the use of ECMWF meteorological forecasts rather than analysed ECMWF meteorological fields. For the NRT processing of TROPOMI data, the TM5-MP model is run once per day in the IDAF at KNMI, and ingests the NO_2 slant columns from the orbits that have been observed thus far. Based on the assimilated "state" of day i, the TM5-MP model provides a forecast of the NO_2 vertical distribution for days $i+1$ until $i+4$. This information is then transferred to the PDGS, as illustrated in Fig. 24, for the NO_2 NRT data product.

This procedure ensures that as soon as new TROPOMI measurements are available in NRT, all necessary information from the TM5-MP model is ready to be processed in the PDGS to provide an NO_2 vertical column data product, without the need for a (time consuming) model run first. With NO_2 profile data available in a 5-day forecast, an interruption of the data stream from the IDAF system is not an immediate problem for the NRT processing system. In case the interruption lasts longer than 5 days, the PDGS processing system will use the latest available NO_2 profile as a fall-back to be able to continue providing NO_2 data in NRT. As fall-back

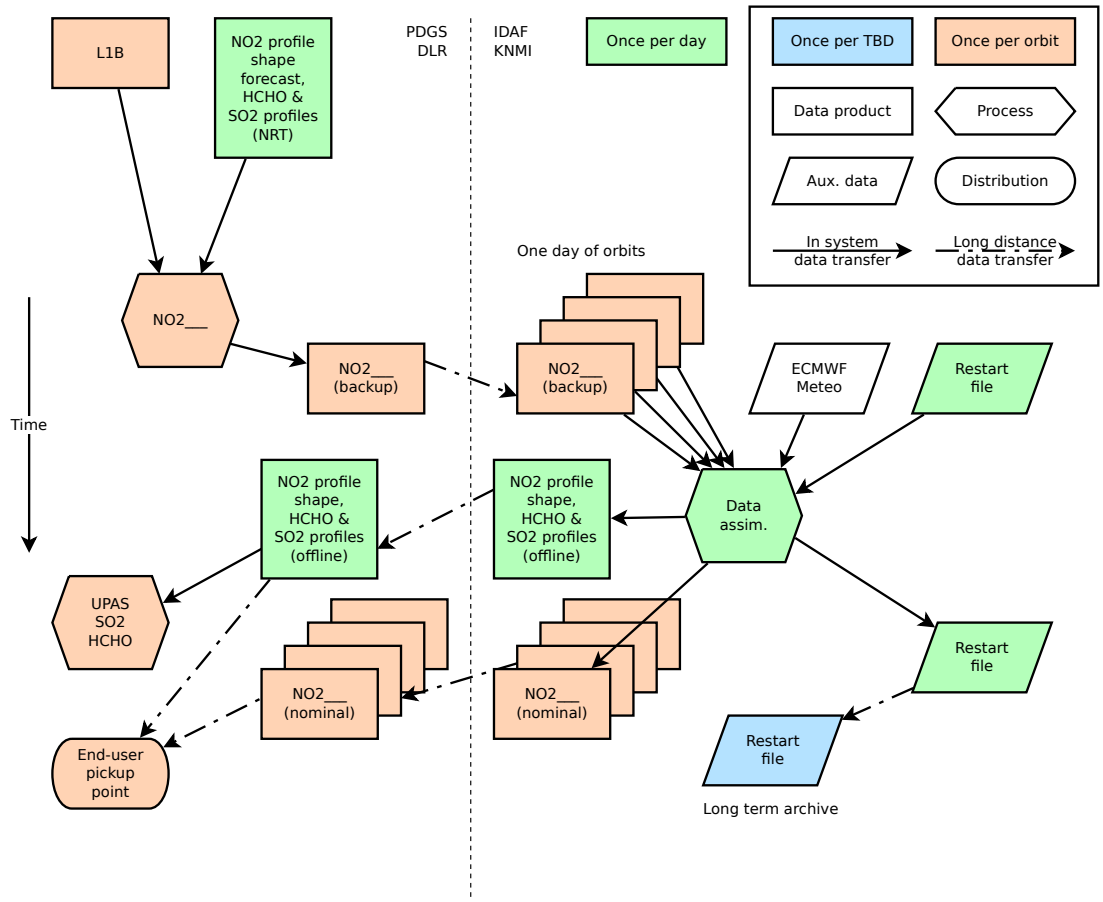

Figure 23: Schematic representation of the TROPOMI processing of tropospheric NO_2 data from a Level-1b spectrum received in the PDGS in the off-line mode. The dotted line marks the division of the processing locations: the Payload Data Ground Segment (PDGS) at DLR on the left and the Instrument Data Analysis Facility (IDAF-L2) at KNMI on the right. (Source of the figure: [RD1].)

the latest available NO_2 profile is used, rather than NO_2 profile data from a climatology, because a switch to climatology data would constitute an evident discontinuity in the NO_2 data.

In the NRT processing, the TM5-MP data assimilation run is started just after midnight, as soon as the ECMWF meteo data has arrived. In that run, the system incorporates all the NO_2 slant column data that has been processed since the previous data assimilation run (from 24 hours before). Since the (ECMWF) forecast is provided up to 5 days ahead, the NRT processing is capable of providing tropospheric NO_2 data, even after a period of missing data. Previous analysis [Boersma et al., 2007] has shown that the forecast is accurate enough to provide reliable NO_2 tropospheric columns for a few days ahead. The differences between the off-line and NRT NO_2 product are found to be small.

6.6 The NO_2 data product

The NO_2 vertical column data product contains the data sets listed in Table 6. The main product is the tropospheric NO_2 column, but the file also contains all intermediate steps such as the results from the DOAS retrieval, output from the data assimilation, cloud information, input database information, flags, uncertainties and the AMF calculation results. The attributes in the file provide full traceability of the data product (including information on processor version, settings, inputs).

Table 7 provides a list of seven main classes of possible TROPOMI NO_2 data usage, and lists the data sets that these users will need for their applications. For notes on applying the averaging kernel, see Sect. 6.4.9. More information on the content and usage of the data product can be found in the NO_2 Product User Manual (PUM; available via [ER2]).

In order to comply with the SI unit definitions, the TROPOMI NO_2 data product file gives trace gas concentrations in mol/m^2, rather than in the commonly used unit molec/cm^2. The following multiplication factors

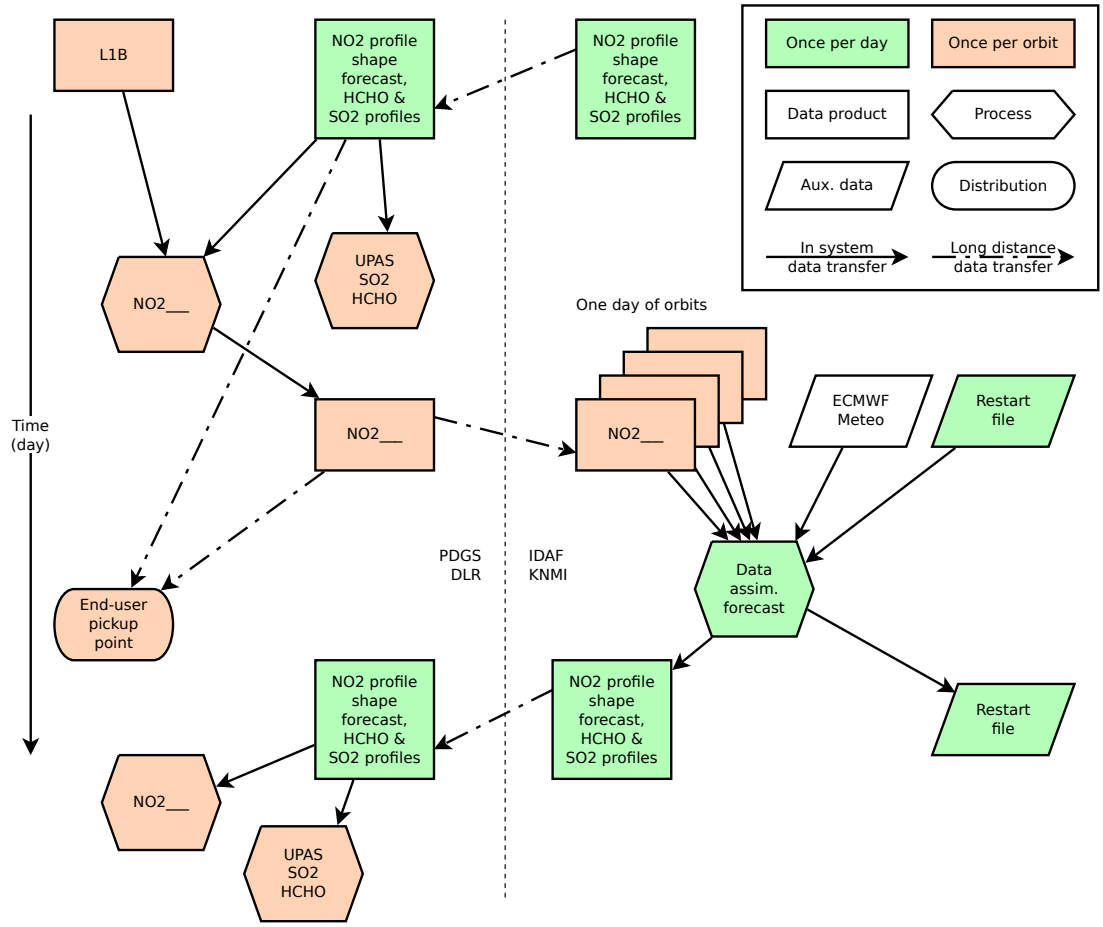

Figure 24: Schematic representation of the TROPOMI processing of tropospheric NO_2 data from a Level-1b spectrum received in the PDGS in the NRT mode. The dotted line marks the division of the processing locations: the Payload Data Ground Segment (PDGS) at DLR on the left and the Instrument Data Analysis Facility (IDAF-L2) at KNMI on the right. (Source of the figure: [RD1].)

– also provided as attributes to the data sets – enabling the user to easily make the conversions, if needed:

- The multiplication factor to convert mol/m^2 to molec/cm^2 is 6.02214×10^{19}.
- The multiplication factor to convert mol/m^2 to DU is 2241.15.
- The O_2–O_2 concentration is given in mol^2/m^5; the multiplication factor to convert this to the commenly used unit molec^2/cm^5 is 3.62662×10^{37}.

The output for each ground pixel is accompanied by two flags indicating the status of the results of the processing and the retrieval. The "quality assurance value" (`qa_value` or f_{QA}) is a continuous variable, ranging from 0 (no output) to 1 (all is well). Warnings that occur during processing or results of the processing can be reasons to decrease the flag value. The `qa_value` is the main flag for data usage:

- `qa_value` > 0.75.
  For most users this is the recommended pixel filter. This removes clouds (cloud radiance fraction > 0.5), scenes covered by snow/ice, errors and problematic retrievals. Default choice for user applications 1, 2, 5, 6, and 7 (viz. Table 7).
- `qa_value` > 0.50.
  This adds the good quality retrievals over clouds and over scenes covered by snow/ice. Errors and problematic retrievals are still filtered out. In particular this may be useful for assimilation and model comparison studies. Default choice for user applications 3 and 4, and may be considered for user applications 1 and 5 (viz. Table 7).

Table 6: Overview of data sets for each ground pixel in the final NO_2 data product assembled for dissemination via the TROPOMI website, the Sentinel-5P Core Service. Where relevant, the precision of a data set is provided as well. Data sets marked with $*$ are not part of the official Level-2 data product, but are provided in a separate support data file. A more detailed overview can be found in Tables 12 and 13.

origin of data set	*for each ground pixel*	*symbols*
Level-1b spectrum	measurement time	t
	ground pixel centre and corner coordinates	ϑ_{geo}, δ_{geo}
	viewing geometry data	θ_0, θ, ϕ_0, ϕ
Databases	surface albedo in the NO_2 window	$A_{\text{s,NO}_2}$
	surface albedo used for the cloud retrieval	A_{s}
	surface elevation and pressure	z_{s}, p_{s}
Cloud retrieval	cloud fraction and cloud pressure FRESCO	f_{eff}, p_{c}
	scene pressure and scene albedo FRESCO	p_{sc}, A_{sc}
	cloud fraction in the NO_2 window	$f_{\text{eff,NO}_2}$
	cloud radiance fraction in the NO_2 window	w_{NO_2}
DOAS retrieval	NO_2 slant column	$N_{\text{s,NO}_2}$
	NO_2 geometric column	$N_{\text{v,NO}_2}^{\text{geo}}$
	slant columns of secondary trace gases	$N_{\text{s,O}_3}$, $N_{\text{s,H}_2\text{O}_{\text{vap}}}$, $N_{\text{s,}\ldots}$
	Ring effect coefficient	C_{ring}
	polynomial coefficients	$a_m \;\; [m = 0, 1, ..., n_p]$
	intensity offset coefficients	$c_m \;\; [m = 0, 1, ..., n_{\text{off}}]$
	number of spectral points	n_λ
	degrees of freedom of the fit	D
	RMS error and χ^2 of the fit	R_{RMS}, χ^2
	runs test: deviation and longest run	R_D, R_L
	wavelength calibration coefficients	w_s^{E0}, w_s, w_q
Data assimilation & AMF calculation	NO_2 tropospheric vertical column	$N_{\text{v}}^{\text{trop}}$
	NO_2 stratospheric vertical column	$N_{\text{v}}^{\text{strat}}$
	NO_2 total vertical column	$N_{\text{v}} \equiv N_{\text{s}}/M$
		$N_{\text{v}}^{\text{sum}} \equiv N_{\text{v}}^{\text{trop}} + N_{\text{v}}^{\text{strat}}$
	NO_2 slant column stripe amplitude	$N_{\text{s,NO}_2}^{\text{str}}$
	NO_2 ghost column	$N_{\text{v}}^{\text{ghost}}$
	tropospheric AMF	M^{trop}, $M_{\text{clr}}^{\text{trop}}$, $M_{\text{cld}}^{\text{trop}}$
	stratospheric and total AMF	M^{strat}, M
	averaging kernel	$\mathbf{A}$
	TM5 tropopause layer index	$l_{\text{tp}}^{\text{TM5}}$
	TM5 pressure level coefficients	A_l^{TM5}, B_l^{TM5}
	$*$ NO_2 profile for stratosphere and troposphere	v_{l,NO_2}
	$*$ TM5 temperature profile	T_l^{TM5}
	$*$ TM5 surface elevation and pressure	$z_{\text{s}}^{\text{TM5}}$, $p_{\text{s}}^{\text{TM5}}$
Flags	quality assurance value (`qa_value`)	f_{QA}
	processing quality flags	—
	absorbing aerosol index	—
	snow/ice flag and land/water classification	—

The determination of the `qa_value` is described in detail in App. E. The `qa_value` indicates whether the footprint is cloud covered or not, and whether there is snow or ice on the surface. It is set to 0 if anywhere in the processing an error occured, as indicated by the `processing_quality_flags`. Warnings related to the South Atlantic Anomaly, sun glint, or missing non-critical input data lower the `qa_value`. The `qa_value`

Table 7: Overview of different user applications of NO_2 data and the data sets from the TROPOMI NO_2 data product the users will need. In addition all users may need pixel related data, such as measurement time, geolocation, viewing geometry, etc., as well as the processing and data quality flags.

	user application	*data sets needed*
# 1	Tropospheric chemistry / air quality model evaluation and data assimilation Validation with tropospheric NO_2 profile measurements (aircraft, balloon, MAX-DOAS)	N_v^{trop}, $\Delta N_v^{trop,kernel}$ M^{trop}, M, **A** † A_l^{TM5}, B_l^{TM5}, l_{tp}^{TM5}, p_s f_{QA}
# 2	Tropospheric column comparisons, e.g. with other NO_2 column retrievals	N_v^{trop}, ΔN_v^{trop} f_{QA}
# 3	Stratospheric chemistry model evaluation and data assimilation Validation with stratospheric NO_2 profile measurements (limb/occultation satellite observations)	N_v^{strat}, ΔN_v^{strat} ‡ A_l^{TM5}, B_l^{TM5}, l_{tp}^{TM5}, p_s f_{QA}
# 4	Stratospheric column comparisons, e.g. with ground-based remote sensors	N_v^{strat}, ΔN_v^{strat} f_{QA}
# 5	Whole atmosphere (troposphere + stratosphere) data assimilation systems	N_v, ΔN_v^{kernel}, **A** § A_l^{TM5}, B_l^{TM5}, l_{tp}^{TM5}, p_s f_{QA}
# 6	Whole atmosphere (troposphere + stratosphere) comparisons with ground-based remote sensing (e.g. Pandora)	N_v^{sum}, ΔN_v^{sum} § f_{QA}
# 7	Visualisation of the NO_2 product, as well as generation of Level-3 gridded and time averaged NO_2 fields	N_v^{trop}, N_v^{strat}, N_v^{sum} § f_{QA}

† The tropospheric kernel $\mathbf{A}^{trop}$ is derived from the total kernel **A** and the air-mass factors M and M^{trop}.
‡ The stratospheric column is a model (data assimilation analysis) quantity and therefore does not have an averaging kernel. The tropopause pressure can be computed using l_{tp}^{TM5} and the hybrid level specification.
§ Note that the total NO_2 vertical column $N_v \equiv N_s/M$ is *not* the same as the sum $N_v^{sum} \equiv N_v^{trop} + N_v^{strat}$

depends on the solar zenith angle, tropospheric air-mass factor and quality of the DOAS fit, and filters unrealistic albedo values.

As of TROPOMI NO_2 product version 1.2 the rather strict filtering of snow/ice covered scenes was abandoned and retrievals receive a `qa_value` > 0.75 when the scene pressure from the cloud retrieval is close to the surface pressure. This significantly enhances the coverage over high latitudes, as shown in Figure 25.

The "processing quality flags" (`processing_quality_flags`) contains the individual event that led to processing failure, and/or a precise record of the warnings that occurred during processing. The definitions and usage of these two flags is harmonised between the Level-2 data products of TROPOMI and is documented in the NO_2 Product User Manual (PUM; available via [ER2]).

The NO_2 data product provides the Absorbing Aerosol Index (AAI; the ATBD of the AAI is available via [ER1] and [ER5]) and a snow/ice flag (see Sect. 6.4.6) as additional information for the NO_2 data users, both in the off-line and the NRT processing mode. The AAI is not yet used in the flags discussed above, but this may be added in an upcoming update.

The data product consists of two files: one with the main NO_2 retrieval results and a separate TM5-MP model data file with vertical information on atmospheric NO_2, SO_2 and HCHO profile and temperature at the $1^\circ \times 1^\circ$ grid of TM5-MP on a half-hourly basis. The additional model datafile (described in [RD23] and available via [ER5]), is large and is not relevant for most NO_2 data users, but for some advanced users the model profiles have shown to be useful.

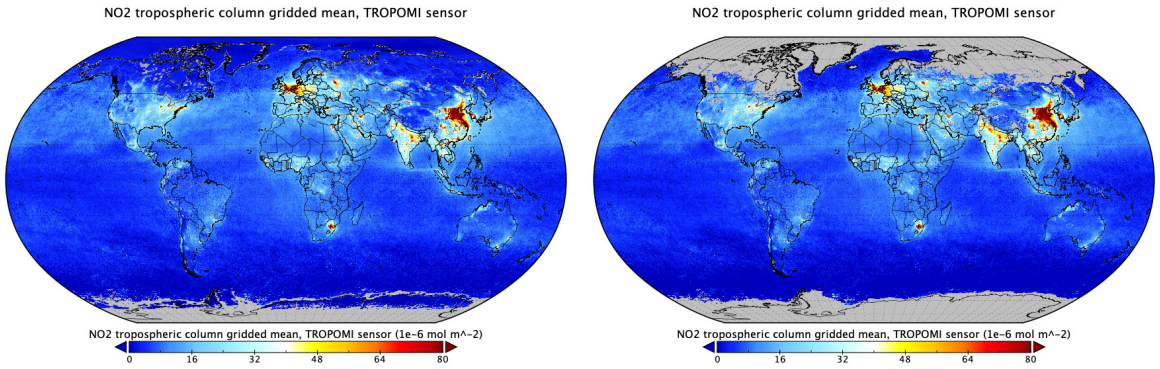

Figure 25: In TROPOMI NO_2 product version 1.2 (operational since 24 October 2018) the filtering over snow and ice is relaxed, greatly improving the coverage. *Left panel:* monthly mean NO_2 concentration for April 2018, v1.2; *right panel:* same but for v1.0.

7 Input-Output file description

7.1 Required input

The processing of TROPOMI NO_2 data poses different demands for different retrieval steps, as described in Sect. 6.5. The dynamic and static input data needed in the PDGS for the off-line and NRT processing of the NO_2 data product are listed below and summarised in Table 8 and Table 9, respectively. Table 8 also mentions the fall-back in the processing of a given ground pixel in case the dynamical data is not available.

The FRESCO/KNMI cloud product is a TROPOMI Level-2 support product, provided by KNMI software running in the PDGS as separate process with its own Level-2 data files. As of NO_2 v2.2.0 an additional cloud product, based on the KNMI O_2–O_2 cloud algorithm developed for OMI, is produced during the processing for NO_2 (cf. Sect. 6.4.4). Both the FRESCO and the O_2–O_2 cloud data are given in separate data groups in the NO_2 product files. The NO_2 v2.2.0 data product uses the FRESCO cloud product. For a later release we will study the quality of both cloud products and develope rules to use one or the other cloud product depending on under which circumstances they work best. The S5P/DLR cloud product is optional; the actual use of this product will be investigated.

For the snow/ice cover data, NISE [ER19] and ECMWF assimilated data are requested, at least one is required, with daily updates near the polar region, less frequent updates closer to the equator. (See also the general TROPOMI documents [RD14] and [RD1].)

7.1.1 Inputs at the PDGS for spectral fitting and air-mass factor calculation

In the PDGS at DLR the following input is required, making a distinction between: (a) static (constant) input data and dynamic input data, which changes every orbit, and (b) data needed for the spectral fitting, and information needed in the subsequent processing step. After the DOAS NO_2 retrieval, the PDGS assembles the NO_2 vertical column data product, using information from the data assimilation system from the IDAF at KNMI for further processing, as Illustrated in Fig. 23.

Spectral fitting input data for the DOAS fit

- Dynamic input:
  - Level-1b Earthshine and Solar spectra
- Static input:
  - Reference spectra (convolved with the TROPOMI slit function; [ER13]) for NO_2, O_3, H_2O_{vap}, O_2–O_2, H_2O_{liq}, Ring effect, irradiance

Note that since the TROPOMI slit function differs for each of the viewing directions, i.e. for each of the detector rows, there is one set of reference spectra for each viewing direction.

NO_2 data product input data

- Dynamic input:

Table 8: Overview of the dynamic input data needed for both the off-line and the NRT NO_2 data processing in the PDGS. The table does not list the meteorological input needed by the data assimilation system in the IDAF. See Sect. 7.1 for further remarks.

name/data	*symbol*	*unit*	*source*	*pre-process needs*	*backup if not available*	*comments*
S5P Level-1b Earth radiance VIS band	$I(\lambda)$	mol/s/m^2/nm/sr	S5P Level-1b product	per pixel	no retrieval	—
S5P Level-1b Solar irradiance VIS band	$E_0(\lambda)$	mol/s/m^2/nm	S5P Level-1b product	per pixel	use previous	—
NO_2 profile	$v_{l,\mathrm{NO_2}}$	mixing ratio	TM5-MP model	per pixel	latest available [†]	NRT
					N/A	off-line
KNMI cloud products	f_{eff}	1	S5P Level-2 support	—	no VCD product	—
FRESCO &	p_{c}	Pa	product			
O_2–O_2 [‡]	A_{c}	1				
	A_{sc}	1				
	p_{sc}	Pa				
S5P/DLR cloud product	f_{eff}	1	S5P Level-2 cloud product	—	no VCD product	optional
	p_{c}	Pa				
snow/ice cover flag	—	—	ECMWF	per pixel	previous day	[#]
					NISE [ER19]	
digital elevation map	z_{s}	m	Copernicus 90m [ER9]	per pixel	[§]	—
surface pressure	p_{s}	m	ECMWF	per pixel	from DEM	[¶]
aerosol absorbing index	AAI	1	S5P Level-2 AAI	—	set AAI fill value	NRT
			354/388 nm pair		set AAI fill value	off-line

[†] Latest available forecast NO_2 profile for that day.
[‡] The FRESCO and O_2–O_2 cloud product data are both included in the NO_2 data files in data sub-groups of `DETAILED_RESULTS`; the cloud product selected from these two for a given ground pixels is copied to the data group `INPUT_DATA`.
[#] If the ECMWF value for the day is not available, the value previous day is used; if that value is unavailable, the snow/ice flag from NISE is used, with ultimate fall-back to a climatological value.
[§] The dynamic elevation data is constructed as an average over the actual pixel geometry (with standard deviation and extrema). As backup in case of missing input and with degraded data quality, static input is used which in constructed as and average over a 10-km circular region which is representative for the TROPOMI pixel, sampled per 3 km [RD24].
[¶] When determining the surface pressure from the DEM surface altitude, ECMWF data (if available) is used to correct the DEM data.

  - NO_2 slant column density & errors from the DOAS fit
  - NO_2 profile shape from the TM5-MP data assimilation system
  - Temperature and pressure profile, orography and tropopause level from TM5-MP / ECMWF
  - Geolocation data (incl. pixel corner coordinates)
  - Viewing geometry
  - Pixel-average terrain height using the actual pixel geometry from a digital elevation map (the Copernicus 90m DEM; [ER9]), including a land/water classification
  - Effective cloud fraction and cloud pressure
  - Scene albedo and scene pressure
  - Snow and ice cover data
  - Surface pressure data
- Static input:
  - Pixel-average representative (interpolated) surface albedo at 440 nm (representative for the NO_2 window)
  - Altitude-dependent AMF look-up table
  - Cloud fraction and cloud radiance fraction look-up table

7.1.2 Inputs at the IDAF for the data assimilation

In the IDAF at KNMI the NO_2 slant column data received from the PDGS is used in the data assimilation system to determine the NO_2 profile shape needed for the conversion of the NO_2 slant columns from the DOAS fit into the stratospheric and tropospheric NO_2 columns at the PDGS. For this step the following input is required for the data assimilation system.

Table 9: Overview of the static input data needed for both the off-line and the NRT NO_2 data as of processor version 2.7.1 in the PDGS. The reference spectra convolved with the TROPOMI slit function (see column 5) are given each of the detector rows. The table does not list the input needed by the data assimilation system in the IDAF. See Sect. 7.1 for further remarks.

name/data	*symbol*	*unit*	*source*	*pre-process needs*	*comments*
absorption cross sections					
NO_2	$\sigma_{NO_2}(\lambda)$	m^2/mol	Vandaele et al. [1998]	convolution	—
O_3	$\sigma_{O_3}(\lambda)$	m^2/mol	Gorshelev et al. [2014] & Serdyuchenko et al. [2014]	convolution	—
O_2–O_2	$\sigma_{O_2-O_2}(\lambda)$	m^5/mol^2	Thalman and Volkamer [2013]	convolution	—
H_2O_{vap}	$\sigma_{H_2O_{vap}}(\lambda)$	m^2/mol	HITRAN 2012 data	convolution	†
H_2O_{liq}	$\sigma_{H_2O_{liq}}(\lambda)$	1/m	Pope and Frey [1997]	convolution	—
Ring reference spectrum	$I_{ring}(\lambda)$	mol/s/m^2/nm	Chance and Spurr [1997]	convolution	†
irradiance reference spectrum	$E_{ref}(\lambda)$	mol/s/m^2/nm	Chance and Kurucz [2010]	convolution	—
retrieval input settings	—	—	KNMI	—	—
air-mass factor lookup table	—	—	KNMI	—	—
cloud fraction lookup table	—	—	KNMI	—	‡
surface albedo database	A_{s,NO_2}	1	TROPOMI DLER v2.1 [RD21]; Tilstra et al. [2024]; [ER17]	per pixel	#

† Created e.g. as in Van Geffen et al. [2015]; see also [RD14].
‡ For the cloud fraction retrieval in the NO_2 fit window and for the cloud radiance fraction.
# Climatological value may be adjusted based on the dynamical snow/ice flag; cf. Sect. 6.4.5 & App. D.

Table 10: Approximate computational effort for the off-line TROPOMI NO_2 processing for processing ground pixels after the along-track pixel size reduction on 6 Aug. 2019 and including the O_2–O_2 cloud retrieval. Any delays introduced by the different processing steps having to wait for data to be available are not included.

	Time needed for processing one TROPOMI orbit	*Time needed for processing one day of TROPOMI data*
Spectral fitting & O_2–O_2 clouds & AMF	27 min (9 cores)	6.5 hours (9 cores)
Data transfer DLR $\rightarrow$ KNMI	$<$ 1 min	$<$ 15 min
AMF/assimilation/modelling (TM5-MP)	4 mins (20 cores)	1 hour (20 cores)
Data transfer KNMI $\rightarrow$ DLR	$<$ 1 min	$<$ 15 min
Total processing time	35 min	8 hours

Data assimilation input data

- Dynamic input:
  - ECMWF meteorological fields (pressure, temperature, wind, ...)
  - The "NO_2 data product input data" listed above
  - TM5-MP start field from the previous day
  - (In case de-striping is turned on:) Destriping coefficients from the previous day
- Static input:
  - TM5-MP static input data: NO_x (and other) emission inventories, climatologies, ...

7.2 Computational effort

Table 10 contains an overview of the processing time needed for the NO_2 product; for one pixel the spectral fitting and AMF calculation takes about 0.006 seconds (excluding overhead). The code was developed at KNMI, mainly in C++, and was transferred to and tested at DLR.

Compared to OMI, TROPOMI has about 10 times more observations, which implies a factor 10 extra computing time for the DOAS NO_2 SCD retreival; the inclusion of the O_2–O_2 cloud data retrieval as of NO_2 processor v2.2.0 increased the processing time by a factor of about 2.7. Especially the TM5-MP processing of TROPOMI was taking quite some CPU time. In April-May 2018 the AMF retrieval loop inside TM5-MP was

Table 11: Estimate of the computational effort for the near-real time TROPOMI NO_2 processing for processing ground pixels after the along-track pixel size reduction on 6 Aug. 2019 and including the O_2–O_2 cloud retrieval. Any delays introduced by the different processing steps having to wait for data to be available are not included.

	Time needed for processing one TROPOMI orbit in NRT
Spectral fitting & O_2–O_2 clouds & AMF	27 min (16 cores)
Data transfer DLR $\rightarrow$ KNMI	$<$ 1 min
Data assimilation with TM5-MP	N/A
Data transfer KNMI $\rightarrow$ DLR	$<$ 15 min (once a day)
Total processing time	45 min

parallelised over observations. Together with other optimisations this has resulted in a speed-up of a factor 5, to 1h processing time on 20 processors for one day of TROPOMI retrievals.

The assimilation of 15 million observations per day does not lead to a slowdown of the analysis step compared to OMI. The TROPOMI pixels are binned to so-called superobservations at $1^\circ \times 1^\circ$ (Sect. 6.3). The number of TROPOMI superobservations is comparable to the number for OMI (before the row anomaly occurred). The number of superobservations to be assimilated is thinned out by a factor 2 (checkerboard approach) to further reduce the computational burden.

7.3 Near-real time timeliness

For the NRT Level-2 data to be available within the required 3 hours after measurement, it is required that the processing of Level-2 data does not take more than about 40 minutes per orbit. Table 11 shows that the actual processing time is about 27 minutes (using 16 cores) and is therefore within the NRT constraints.

The data assimilation run is done at KNMI once a day (just after midnight) to provide a forecast of the NO_2 profile for the coming 5 days, based on assimilation of TROPOMI slant columns observed over the previous day. These forecast runs have recently been accelerated and takes $\sim$3h for one forecast. Note that the NRT chain does not need to wait for this, as mentioned in Sect. 6.5.2.

7.4 NO_2 product description and size

The TROPOMI NO_2 data output product consists of the retrieved tropospheric and stratospheric NO_2 columns, along with error estimates and the (total) averaging kernel. A general overview of the data product contents is given in Sect. 6.6 and Table 6. Table 12 provides a more detailed overview of the data sets, their unit, type, etc. in the main output data product.

As of NO_2 v2.2.0 the processor includes the O_2–O_2 cloud retrieval; see Sect. 6.4.4.3. With this processor change two data sub-groups of `DETAILED_RESULTS` are introduced to hold the FRESCO and the O_2–O_2 cloud & scene data, named `FRESCO` and `O22CLD`, respectively. The cloud data selected from these two for a given NO_2 ground pixels are copied to the data group `INPUT_DATA`. For readability Table 12 lists the cloud & scene data fields only once.

Given the number of data per ground pixel listed in Table 12, the Level-2 NO_2 output file of one orbit has the following size: about 340 MB for v1.2.x and v1.3.x prior to the along-track pixel size reduction on 6 Aug. 2019, and after that about 440 MB for v1.3.x and v1.4.0, while v2.2.0 is about 580 MB including the FRESCO and O_2–O_2 data variables. Before (after) the pixel size reduction, an orbit has about 1.5 (1.9) million observations.

The averaging kernel describes how the retrieved NO_2 columns relate to the true NO_2 profile shape [Eskes and Boersma, 2003]. The averaging kernel should be used in validation exercises, model evaluations, and assimilation or inverse modelling attempts with TROPOMI NO_2 data (cf. Sect 6.4.9). The output product also contains the necessary information (surface pressure and TM5-MP sigma coordinates) to construct the pressure grid to which the averaging kernel values correspond.

For advanced users, a separate support file is made available that contains the temperature and NO_2 (SO_2, HCHO) vertical profile. This data is given at the TM5-MP grid resolution of $1^\circ \times 1^\circ$, rather than on TROPOMI pixel basis, on a half-hourly basis for one day per file (i.e. 48 time steps); each file is about 1.6GB). The temperature and NO_2 profiles are not included in the standard Level-2 product, because most users will not need these and because vertical profiles will drastically increase the size of the TROPOMI Level-2 retrieval

Table 12: Overview of the data sets, their units, types and sizes, in the main data output product file, listed alphabetically; cf. Table 6. All quantities followed by a $*$ in the "symbol" column consist of the value and the associated precision (for these the number of data per pixel is doubled in the 6th column); for the vertical column densities the precisions are listed explicitly to clearly show the different types of precisions. See Sect. 7.4 for some remarks on the data from the cloud retrieval. In the last column 'PV' denotes the processor version when this variable was introduced. The data sets in the support data file are listed in Table 13.

name/data	*symbol*	*unit*	*description*	*type*	*data per pixel*	*comments*
aerosol absorbing index	—	1	L2 AAI $354/388$ nm wavel. pair	float	1	added as flag
air-mass factor	M^{trop}	1	tropospheric AMF	float	1	—
	$M^{\text{trop}}_{\text{clr}}$	1	clear-sky tropospheric AMF	float	1	
	$M^{\text{trop}}_{\text{cld}}$	1	cloudy tropospheric AMF	float	1	
	M^{strat}	1	stratospheric AMF	float	1	—
	M	1	total AMF	float	1	—
averaging kernel	$\mathbf{A}$	1	—	float	n_l	†
chi-squared	χ^2	1	χ^2 of the NO_2 DOAS fit	float	1	cf. Eq. (2)
cloud albedo	A_{c}	1	used in the cloud retrieval	float	1	cf. Sect. 6.4.4
cloud fraction	f_{eff}	1	from the cloud retrieval	float	1	—
cloud fraction NO_2	$f_{\text{eff,NO}_2}$	1	for the NO_2 VCD	float	1	in NO_2 fit window
cloud pressure	p_{c}	Pa	from the cloud retrieval	float	1	—
cloud radiance fraction	w_{NO_2}	1	for the NO_2 VCD	float	1	in NO_2 fit window
degrees of freedom	D	1	of the slant column fit	float	1	—
DOAS fit results	$N_{\text{s,NO}_2}$ *	mol/m^2	total NO_2 SCD	float	1 $\times$2	—
	$N^{\text{geo}}_{\text{v,NO}_2}$ *	mol/m^2	geometric NO_2 column	float	1	cf. Eq. (20)
	$N_{\text{s,H}_2\text{O}_{\text{liq}}}$ *	m	H_2O_{liq} coeff. in NO_2 window	float	1 $\times$2	—
	$N_{\text{s,H}_2\text{O}_{\text{vap}}}$ *	mol/m^2	H_2O_{vap} SCD in NO_2 window	float	1 $\times$2	—
	$N_{\text{s,O}_2\text{–O}_2}$ *	mol^2/m^5	O_2–O_2 SCD in NO_2 window	float	1 $\times$2	—
	$N_{\text{s,O}_3}$ *	mol/m^2	O_3 SCD in NO_2 window	float	1 $\times$2	—
	C_{ring} *	1	Ring coeff. in NO_2 window	float	1 $\times$2	—
ghost column	$N^{\text{ghost}}_{\text{v}}$	mol/m^2	NO_2 column below the clouds	float	1	‡
ground pixel coordinates	δ_{geo}	°	VIS pixel – latitude	float	5	centre, 4 corners
	ϑ_{geo}	°	VIS pixel – longitude	float	5	centre, 4 corners
ground pixel index	—	1	across-track pixel index	int	1	—
intensity off. coefficients	c_m *	1	in the NO_2 DOAS fit	float	$(n_{\text{off}}+1)$ $\times$2	cf. Eq. (11)
land/water classification	—	1	surface type classification	int	1	—
measurement time	t	s	VIS pixel	float	2	—
number of wavelengths	n_λ	1	in the NO_2 fit window	int	1	#
number of iterations	n_i	1	from the DOAS fit	int	1	—
polynomial coefficients	a_m *	1	in the NO_2 DOAS fit	float	$(n_p+1)\times$2	cf. Eq. (6)
processing quality flags	—	1	—	int	1	cf. Sect. 6.6
qa value	f_{QA}	1	quality assurance value	float	1	cf. Sect. 6.6 & E
root-mean-square error	R_{RMS}	1	RMS error of the NO_2 DOAS fit	float	1	cf. Eq. (4)
runs test results	R_D	1	deviation from expected #runs	float	1	cf. Eq. (9)
	R_L	1	longest run in the fit residual	int	1	cf. below Eq. (9)
satellite coordinates	z_{sat}	m	altitude of the satellite	float	1	—
	δ_{sat}	°	latitude sub satellite point	float	1	—
	ϑ_{sat}	°	longitude sub satellite point	float	1	—
	φ_{sat}	1	relative offset in orbit	float	1	—
scanline index	—	1	along-track pixel index	int	1	—
scene albedo	A_{sc} *	1	from the cloud retrieval	float	1 $\times$2	—
scene pressure	p_{sc} *	Pa	from the cloud retrieval	float	1 $\times$2	—
snow-ice flag	—	1	snow/ice case flagging	int	1	—
stripe amplitude	$N^{\text{str}}_{\text{s,NO}_2}$	mol/m^2	NO_2 SCD stripe amplitude	float	0 $^\otimes$	cf. Sect. 6.4.10
surface albedo	A_{s}	1	for the cloud retrieval	float	1	—
surface albedo NO_2	$A_{\text{s,NO}_2}$	1	for cloud fraction NO_2 window	float	1	cf. Sect. 6.4.4
surface elevation	z_{s} *	m	VIS pixel	float	1 $\times$2	—
surface pressure	p_{s}	Pa	VIS pixel	float	1	—

Table continues on next page

Table 12: — *continued.*

name/data	*symbol*	*unit*	*description*	*type*	*data per pixel*	*comments*
TM5 pressure level	A_l^{TM5}	Pa	—	float	0 ¶	—
coefficients	B_l^{TM5}	1	—	float	0 ¶	—
TM5 tropopause layer index	$l_{\text{tp}}^{\text{TM5}}$	1	—	int	1	—
vertical column density	$N_{\text{v,NO}_2}^{\text{trop}}$	mol/m^2	tropospheric NO_2 VCD	float	1	—
	$\Delta N_{\text{v,NO}_2}^{\text{trop}}$	mol/m^2	*id.* precision, kernel not applied	float	1	cf. Sect. 8.4
	$\Delta N_{\text{v,NO}_2}^{\text{trop,kernel}}$	mol/m^2	*id.* precision, kernel applied	float	1	cf. Sect. 8.4
	$N_{\text{v,NO}_2}^{\text{strat}}$	mol/m^2	stratospheric NO_2 VCD	float	1	—
	$\Delta N_{\text{v,NO}_2}^{\text{strat}}$	mol/m^2	*id.* precision	float	1	—
	$N_{\text{v,NO}_2}$	mol/m^2	total NO_2 VCD	float	1	$\equiv N_{\text{s}}/M$
	$\Delta N_{\text{v,NO}_2}$	mol/m^2	*id.* precision, kernel not applied	float	1	cf. Sect. 8.4
	$\Delta N_{\text{v,NO}_2}^{\text{kernel}}$	mol/m^2	*id.* precision, kernel applied	float	1	cf. Sect. 8.4
	$N_{\text{v,NO}_2}^{\text{sum}}$	mol/m^2	summed NO_2 VCD	float	1	$\equiv N_{\text{v}}^{\text{trop}} + N_{\text{v}}^{\text{strat}}$
	$\Delta N_{\text{v,NO}_2}^{\text{sum}}$	mol/m^2	*id.* precision	float	1	—
viewing geometry data	θ_0	$^\circ$	solar zenith angle	float	1	at surface
	ϕ_0	$^\circ$	solar azimuth angle	float	1	at surface
	θ	$^\circ$	viewing zenith angle	float	1	at surface
	ϕ	$^\circ$	viewing azimuth angle	float	1	at surface
wavelength calibration	w_s *	nm	wavelength shift	float	1 ×2	cf. Eq. (7)
radiance	w_q *	1	wavelength stretch	float	1 ×2	cf. Eq. (7)
	χ_w^2	1	χ^2 of the calibration	float	1	cf. Eq. (7)
wavelength calibration	w_s^{E0} *	nm	wavelength shift	float	0 ×2 ⊗	cf. Eq. (7)
irradiance	$(\chi_w^{E0})^2$	1	χ^2 of the calibration	float	0 ⊗	cf. Eq. (7)

† The number of TM5-MP layers is $n_l = 34$.
‡ The NO_2 ghost column is the TM5-MP NO_2 profile integrated from the surface to the cloud pressure level.
# The actual number of wavelengths n_λ used in the fit (cf. Eq. (2)), i.e. after removal of, for example, bad pixels within the fit window.
¶ One set of $n_l + 1$ (see note †) TM5-MP pressure level coefficients per data file.
⊗ One value per detector row.

Table 13: Overview of the data set units, types and sizes in the support output product file; this file is also used to store the profiles of HCHO and SO_2, delivered along with the NO_2 profile by the TM5-MP model (see [RD23], available via [ER5]). The data is provided on the TM5-MP grid resolution of $1^\circ \times 1^\circ$ on a half-hourly basis, rather than on TROPOMI pixel basis. The data sets in the main data file are listed in Table 12.

name/data	*symbol*	*unit*	*description*	*type*	*data per grid cell*	*comments*
HCHO profile	$v_{l,\text{HCHO}}$	1	volume mixing ratio	float	n_l	†
NO_2 profile	v_{l,NO_2}	1	volume mixing ratio	float	n_l	†
SO_2 profile	v_{l,SO_2}	1	volume mixing ratio	float	n_l	†
TM5 temperature profile	T_l^{TM5}	K	—	float	n_l	†
TM5 pressure level coefficients	A_l^{TM5}	Pa	—	float	0 ¶	—
	B_l^{TM5}	1	—	float	0 ¶	—
TM5 surface elevation	$z_{\text{s}}^{\text{TM5}}$	m	—	float	1	cf. Table 9
TM5 surface pressure	$p_{\text{s}}^{\text{TM5}}$	Pa	—	float	1	—
TM5 tropopause layer index	$l_{\text{tp}}^{\text{TM5}}$	1	—	int	1	—
stripe amplitude	$N_{\text{s,NO}_2}^{\text{str}}$	mol/m^2	NO_2 SCD stripe amplitude	float	0 ⊗	cf. Sect. 6.4.10
date & time	—	1	year, month, day, hour, min, sec	int	0 §	—
time	d	days	no. of days since 1 Jan. 1950	float	0 §	—

† The number of TM5 layers is $n_l = 34$.
¶ One set of $n_l + 1$ (see note †) TM5-MP pressure level coefficients per data file.
§ One set per data file.
⊗ One value per detector row.

files. Table 13 provides an overview of the data sets in the support output data product; a Product User Manual (PUM) for this TM5 NO_2, SO_2 and HCHO profile auxiliary support product, identified as S5P-KNMI-L2-0035-MA [RD23], is available via [ER2].

8 Error analysis

The TROPOMI NO_2 retrieval algorithm generates stratospheric and tropospheric vertical column densities for all pixels. Since assumptions differ considerably for stratospheric and tropospheric retrievals, the error budget for each case is treated separately below.

The overall error for the retrieved tropospheric columns is determined through propagation of the three main error sources: (a) measurement noise and spectral fitting affecting the slant columns, (b) errors related to the separation of stratospheric and tropospheric NO_2, and (c) systematic errors due to uncertainties in model parameters such as clouds, surface albedo, and a-priori profile shape, affecting the tropospheric air-mass factor. For the stratospheric NO_2 column, the errors are driven by slant column errors, errors in the estimate of the stratospheric contribution to the slant column, and stratospheric AMF (observation operator) errors.

For NO_2, the overall error budget thus consists of several different error source terms. Errors in the slant columns are driven in part by instrumental noise (random errors), and in part by necessary choices on the physical model and reference spectra used (systematic errors). Errors in the AMF are mostly systematic (e.g. assumptions on albedo) but will also have random contributions (e.g. from observed cloud parameters, or sampling / interpolation errors). It is thus not possible to make a clear distinction between these error types in the total error reported in the TROPOMI NO_2 data product. This implies that by averaging TROPOMI pixels over time or over a larger area, the random part of the overall error can be largely eliminated, but systematic effects may still persist in averaged retrievals.

Experience with errors in OMI NO_2 over polluted regions, largely stemming from theoretical error analysis and practical validation studies, indicates that overall errors on the order of 25% for individual tropospheric NO_2 column retrievals may be expected. Validation studies show that the systematic part of this error is on the order of 10-15% (e.g. Hains et al. [2010]; Irie et al. [2012]; Ma et al. [2013]). For stratospheric NO_2 columns, the errors are considerably smaller and depend mostly on the absolute accuracy of the slant columns, and on the separation of the stratospheric and tropospheric contributions. The stratospheric NO_2 column error is expected to have errors on the order of 5-10% (e.g. Hendrick et al. [2012]) or $0.15-0.2\times10^{15}$ molec/cm^2.

8.1 Slant column errors

Instrument noise is the main source of errors in the spectral fitting of TROPOMI Level-1b spectra. The radiometric signal-to-noise ratios (SNR) of TROPOMI in the $400-500$ nm range turns out to be $1400-1500$ for a individual Level-1b spectra [RD4]. Experience with OMI spectral fitting in the $405-465$ nm spectral domain showed that the uncertainty in OMI NO_2 slant column densities of about 0.75×10^{15} molec/cm^2 in 2005 (when the SNR of OMI was $900-1000$) to about 0.90×10^{15} molec/cm^2 in 2015 (Boersma et al. [2007], Zara et al. [2018]). Van Geffen et al. [2020] show a comparison between TROPOMI and OMI slant column errors and statistical uncertainties. Other, potentially systematic, errors include inaccuracies in the NO_2 cross-section spectrum (Vandaele et al. [1998]; [ER14]), in other reference spectra, notably in the Ring spectrum, and in the temperature dependence of the NO_2 cross section, but these have been shown to be of little concern for the slant column errors [Boersma et al., 2002].

Fig. 26 shows as function of the SNR an estimate of the uncertainty of the retrieved slant column density determined by a DOAS fit in the wavelength window $405-465$ nm with polynomial degree 5. Spectra were simulated with a radiative transfer code using an atmosphere with two NO_2 profiles, taken from the CAMELOT study [RD9], with the same profile shape in the stratosphere:

(*a*) European background profile, simulated with a total vertical column $N_\mathrm{v}=2.5\times10^{15}$ molec/cm^2

(*b*) European polluted profile, simulated with a total vertical column $N_\mathrm{v}=7.5\times10^{15}$ molec/cm^2

The simulations are performed with surface albedo $A_\mathrm{s}=0.05$, no clouds, solar zenith angle $\theta_0=50^\circ$, and looking down in nadir. The legend of Fig. 26 gives the total slant column N_s in 10^{15} molec/cm^2. The retrieved N_s varies very little with the SNR: about 3×10^{12} molec/cm^2 between SNR$=700$ and 1100. For profile (*a*) the retrieved N_s is within 5% of the inital N_s and for profile (*b*) it is within 3%. Given this, a good accuracy of the DOAS fits can be expected, with uncertainties in the range of $10-15\%$ for background NO_2 cases and $5-10\%$ for polluted cases.

Fig. 27 shows a direct comparison of the NO_2 slant column error of OMI and TROPOMI as reported by the DOAS fits on actual observations from both instruments. The figure demonstrates that TROPOMI has an SCD error of about $8-10$ μmol/m^2, or $0.5-0.6\times10^{15}$ molec/cm^2. The OMI noise level in 2005 is about 40% higher than what is observed with TROPOMI. This is in agreement with the theoretical dependence on SNR described above. Some further comparisons are reported by Van Geffen et al. [2020].

During the TROPOMI commissioning phase it became clear that over bright scenes, e.g. high thick clouds in the tropics, the measurements at the visible wavelengths may become saturated. One very sensitive parameter

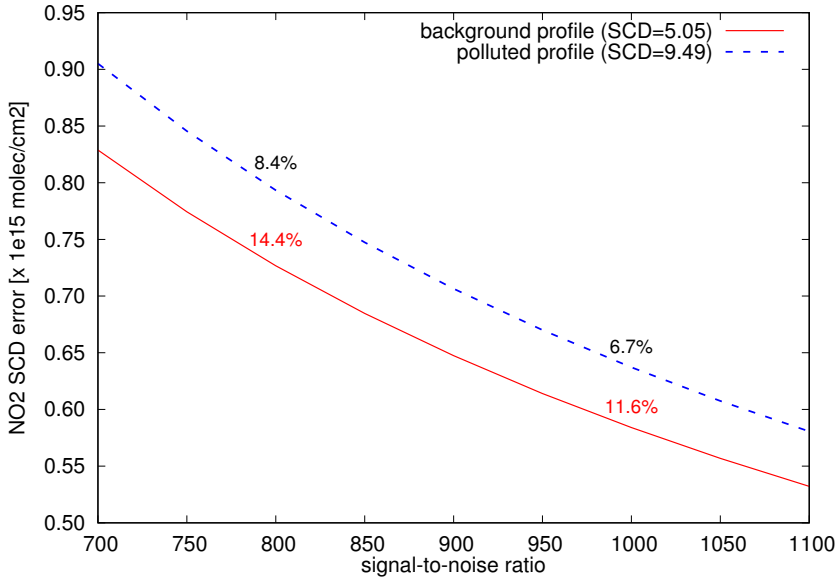

Figure 26: DOAS retrieval slant column uncertainty estimate [in 10^{15} molec/cm^2] as function of the SNR for two NO_2 profiles. The plot legend gives the retrieved slant column in 10^{15} molec/cm^2. At SNR equal 800 and 1000 the relative slant column uncertainty is indicated. For further details see the text.

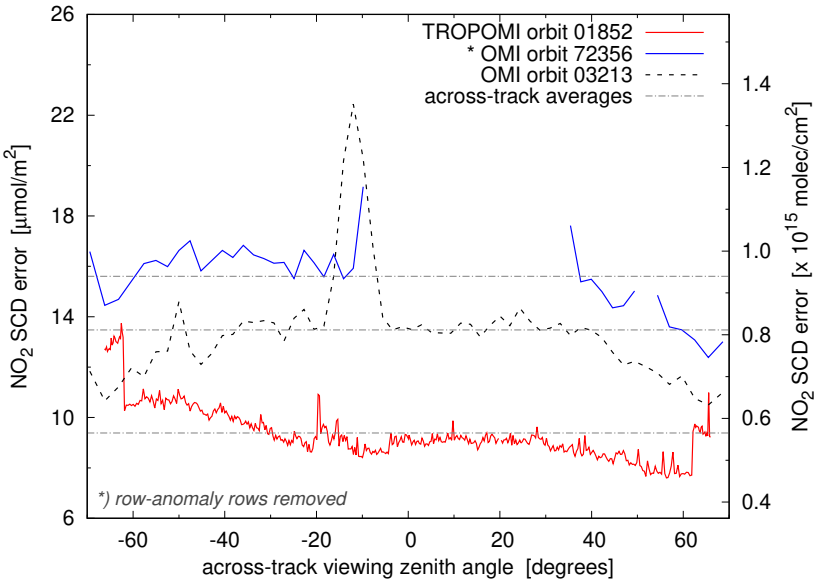

Figure 27: NO_2 slant column error estimates for the Pacific Ocean orbit on 20 Feb. 2018 of TROPOMI are compared to those for the almost overlapping OMI orbit (with rows affected by the row anomaly removed) and to those of a similar OMI orbit from 20 Feb. 2005. Data of scanlines with nadir latitude in the range $[-20°:+20°]$ is averaged along-track; OMI data is processed within the QA4ECV project [RD6], [ER7].

to detect saturation is the NO_2 slant column uncertainty, and therefore this is used as one of the quality criteria (`qa_value`, see App. E): when the slant column uncertainty exceeds 33 μmol/m^2, or 2×10^{15} molec/cm^2, the ground pixel is flagged as being of bad quality.

8.2 Errors in the stratospheric (slant) columns

Data assimilation of TROPOMI NO_2 slant columns in TM5-MP provides the estimate of the stratospheric contribution to the NO_2 slant columns. The accuracy of these estimates is largely determined by the accuracy of the slant columns, as the TM5-MP stratospheric NO_2 distributions are scaled to become consistent with the

retrieved slant columns. Random error estimates are derived from the assimilation approach: a considerable advantage of the assimilation scheme is that it provides a statistical estimate of the uncertainties in the stratospheric (slant) columns through the standard deviation of the differences between the TM5-MP model analysis and forecast stratospheric NO_2 ("A–F"). Generally, the uncertainty for the stratospheric NO_2 columns is of the order of $0.1 - 0.2 \times 10^{15}$ molec/cm^2, similar to OMI [Dirksen et al., 2011]. This similarity with OMI is partly the result of using superobservations, which reduces the random contribution to the errors in the stratospheric slant column estimates. Fig. 8, bottom panel, shows the average A–F difference for 1 April 2018 in the data assimilation system based on TM5-MP. The A–F differences are on average 0.15×10^{15} molec/cm^2, and O–F over unpolluted scenes are about 0.2×10^{15} molec/cm^2. The latter is used as estimate of the uncertainties of the stratospheric NO_2 columns.

Forward (radiative transfer) model calculations are important for, but contribute little to errors in the assimilation procedure. The observation operator **H** (see Eq. (12)) is proportional to the averaging kernel [Eskes and Boersma, 2003], the vector that contains the vertical sensitivity of TROPOMI to NO_2 in each layer. The scalar product of the observation operator vector and the TM5-MP NO_2 profile at the location of the individual TROPOMI observations yields the slant column that would be observed by TROPOMI given the modeled profile. Stratospheric radiative transfer calculations around 435 nm are relatively straightforward compared to those for the troposphere, where multiple scattering occurs, and the effects of clouds and aerosols interact with the vertical distribution of NO_2. The main forward model parameter influencing errors in the stratospheric estimate is the a-priori stratospheric NO_2 profile shape (and associated temperature correction), but sensitivity tests suggest that uncertainties in the exact shape of this profile are of little influence to the overall error of the stratospheric NO_2 column.

One potential source of error is the sphericity correction in the radiative transfer model. These errors are negligible for most viewing geometries, but need to be considered for far off-nadir viewing angles and high solar zenith angles. Lorente et al. [2017] investigated the differences between stratospheric NO_2 AMFs calculated with a model simulating radiative transfer for an atmosphere spherical for incoming, single-scattered, and multiple-scattered light (McArtim), and a model with an atmosphere that is spherical for incoming light, but plane-parallel for scattered sunlight. When solar and viewing zenith angles are both large, the DAK model overestimates the stratospheric AMFs by 5-10%. For TROPOMI, we therefore use an AMF LUT that is based on DAK radiative transfer simulations, but whose values for extreme viewing geometries have been made consistent with the McArtim simulations. This is the same AMF LUT that is being used in the QA4ECV retrievals of NO_2 from OMI and GOME-2A ([RD6], [ER7]).

8.3 Errors in the tropospheric air-mass factors

The tropospheric AMF is calculated with a forward model (here version 3.2 of the DAK radiative transfer model) and depends on the a-priori assumed profile shape and forward model parameters (cloud fraction, cloud pressure, surface albedo, surface pressure and aerosol properties). The AMF also depends on the solar zenith, viewing zenith and relative azimuth angles, but the measurement geometry is known with high accuracy and therefore does not contribute significantly to the AMF errors. The forward model itself is assumed to represent the physics of the measurement accurately, so that forward model errors can be characterised in terms of model parameters only.

The most important AMF errors are cloud fraction, surface albedo, and a-priori profile shape. Cloud parameters are obtained from TROPOMI observations, and these have random as well as systematic components. Surface albedo and NO_2 profile shape are obtained from a-priori assumptions (i.e. a pre-calculated climatology and CTM simulations, respectively), and much depends on the accuracy of these assumptions that are different for different retrieval situations (e.g. season, surface type etc.). Because the retrieved cloud fraction depend on similar (if not the same) surface albedo assumptions as the NO_2 air-mass factors, errors will be dampened to some extent [Boersma et al., 2004].

In Table 14 the most probable uncertainties of the forward model parameters to provide a cautious error prediction for TROPOMI NO_2 AMFs are listed. For this the theoretical error propagation framework used in Boersma et al. [2004] is followed. This approach takes into account the sensitivity of the AMF to uncertainties around the actual value of a particular forward model parameter (e.g. the AMF is much more sensitive to albedo errors for dark surfaces than for brighter surfaces).

Aerosol-related errors are intimately coupled to cloud parameter errors. The O_2 A-band cloud algorithm currently does not correct for the presence of aerosols, so that an effective cloud fraction and cloud pressure are retrieved; the same holds for the cloud fraction in the NO_2 window, which is computed in the same manner as the O_2 A-band cloud fraction (Sect. 6.4.4). It is a matter of ongoing research whether or not the

Table 14: Estimate of the contributions to the error in the AMF due to individual error sources ('BL' stands for Boundary Layer.) The estimated AMF errors are considered to be representative of 'typical' retrieval scenarios over regions of interest, i.e. with substantial NO_2 pollution for mostly clear-sky situations, and non-extreme boundary conditions for surface albedo and pressure. Note that the uncertainties can be substantially lager for specific condition, e.g. for very small albedo and large SZA.

Error type	*Estimated error*	*Corresponding AMF error*
Cloud fraction	± 0.025	$\pm 10\%$
Cloud pressure	± 50 hPa	$\pm[0-10]\%$
Surface albedo	± 0.015	$\pm 10\%$
Surface pressure	± 20 hPa	$\pm[0-5]\%$
A-priori NO_2 profile shape	BL height & mixing schemes & free troposphere & emissions	$\pm 20\%$
A-priori NO_x emissions	$\pm[0-25]\%$	$\pm[0-10]\%$
Aerosol-related errors		$\pm[0-10]\%$
Overall error		$\pm[15-25]\%$

disentanglement of aerosol and cloud effects will improve the quality of the AMFs (Leitão et al. [2010]; Boersma et al. [2011]; Lin et al. [2014]).

The results in Table 14 provide a general estimate of overall retrieval uncertainties that may be expected for TROPOMI NO_2 data under polluted conditions. In these conditions, AMF uncertainties contribute most to the retrieval uncertainties. But error analysis for individual retrievals show considerable variability on these estimates [Boersma et al., 2004]. For instance, regions with a low surface albedo are very sensitive to albedo uncertainties, and this can be reflected in AMF errors of more than 50%. For TROPOMI NO_2 a full error propagation that takes these sensitivities into account are provided, and as well as a unique error estimate for every pixel.

Table 14 shows the settings used for TROPOMI retrieval reprocessing. Compared to the OMI-QA4ECV product we have increased the a-priori tropospheric profile shape error to 20%. A motivation for this is the increased resolution of TROPOMI which leads to an increased variability in profile shapes. Also the uncertainties in free tropospheric NO_2 lead to additional errors, and the OMI estimate may be too optimistic. Note that the aerosol-related errors and emission errors are not explicitly accounted for in the error estimate. The emission-related errors are implicitly included in the profile shape error. The estimate of the profile shape error comes from a comparison of the TM5-MP derived air-mass factors and air-mass factors computed with the CAMS regional ensemble forecasts over Europe. Typical differences of the order of 20% are found over the polluted areas.

8.4 Total errors in the tropospheric NO_2 columns

The overall error in the TROPOMI tropospheric NO_2 columns is driven by error propagation of the error terms discussed before, i.e. (1) slant column errors, (2) errors associated with the separation of the stratospheric and tropospheric contributions to the slant column, and (3) tropospheric air-mass factor errors.

The overall error variance for each pixel is written as in Boersma et al. [2004]:

$$\left\langle \varepsilon^2 \right\rangle = \left(\frac{\sigma(N_\mathrm{s})}{M^\mathrm{trop}} \right)^2 + \left(\frac{\sigma(N_\mathrm{s}^\mathrm{strat})}{M^\mathrm{trop}} \right)^2 + \left(\frac{(N_\mathrm{s} - N_\mathrm{s}^\mathrm{strat}) \cdot \sigma(M^\mathrm{trop})}{(M^\mathrm{trop})^2} \right)^2 \tag{25}$$

with $\sigma(N_\mathrm{s})$ the slant column error, $\sigma(N_\mathrm{s}^\mathrm{strat})$ the stratospheric slant column error and $\sigma(M^\mathrm{trop})$ the estimated error in the tropospheric air-mass factor ($\pm 25\%$). The total error depends on details in the retrieval and therefore differs from one pixel to the next. For small tropospheric excess slant columns, the overall retrieval uncertainty is dominated by the random errors in spectral fitting, whereas for large tropospheric slant columns, the retrieval uncertainty is dominated by air-mass factor uncertainties (the last term in Eq. (25)).

Fig. 28 shows the absolute and relative error in the tropospheric NO_2 column retrieved for clear-sky scenes from TROPOMI data on 17 April 2018. We see that over the oceans and the remote continental regions, the overall tropospheric retrieval uncertainty is dominated by errors in the spectral fitting and the stratospheric column estimate and is typically more than 100% (indicated by purple colours in the bottom panel of Fig. 28).

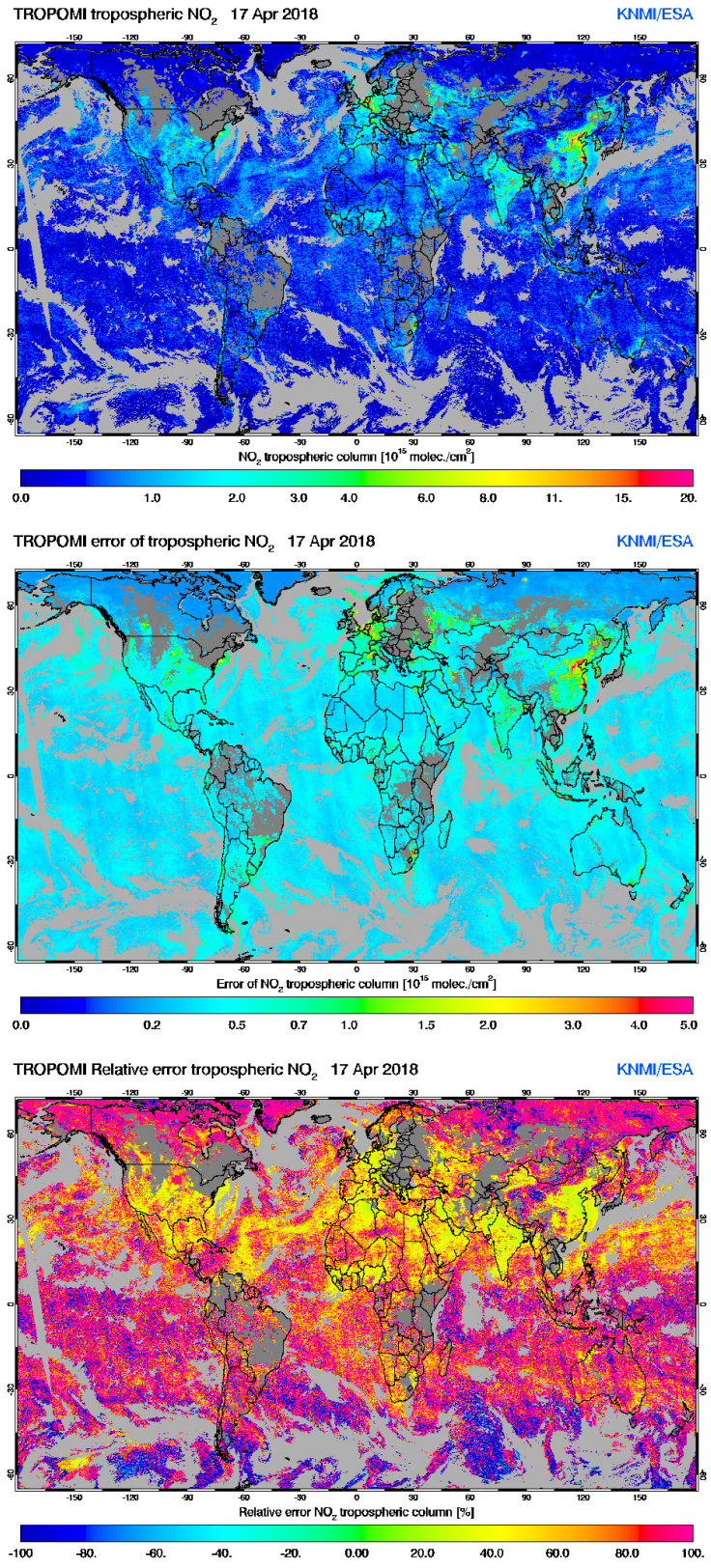

Figure 28: TROPOMI tropospheric NO_2 vertical column values (*top panel*; in 10^{15} molec/cm^2), the corresponding absolute error estimate (*middle panel*; in 10^{15} molec/cm^2; note that the scale range is reduced by a factor 4), and the relative error (*bottom panel*; in %) for 17 April 2018. Large relative errors are seen mostly over areas with small NO_2 column values: oceans and remote continental regions. These errors reflect uncertainties in the slant and stratospheric column. Over the very polluted hotspots typical errors are in the $25-40$% range, reflecting uncertainties in the air-mass factor.

Table 15: Relative tropospheric NO_2 vertical column per pixel uncertainty due to the tropospheric AMF uncertainty only. Estimates based on QA4ECV OMI NO_2 data for selected regions for the year 2005, taken from Boersma et al. [2018].

Region	*Average AMF uncertainty*	*box size ranges*	
		longitude	*latitude*
China	17 - 22 %	$110:140$	$35:45$
USA	17 - 27 %	$-100:-75$	$35:45$
Europe	18 - 26 %	$-10:15$	$40:55$
Johannesburg	15 - 20 %	$26:30$	$-28:-24$

For larger columns over continental areas, the relative uncertainty in the retrieved column reduces to $15-50\%$, and is dominated by the uncertainty in the tropospheric air-mass factor. Retrieval results are generally best for regions with strong NO_2 sources and/or high surface albedos.

Based on the instrumental performance for TROPOMI, and our experience with OMI tropospheric NO_2 retrievals (see Fig. 28 and Table 15), the overall error budget for individual TROPOMI tropospheric NO_2 retrievals can tentatively be approximated as $\varepsilon = 0.5\times10^{15}$ molec/cm^2 + [0.2 to 0.50] $\cdot N_v^{trop}$. This is a more complete and realistic error statement than the requirements from [RD5] ($\varepsilon = 1.3\times10^{15}$ molec/cm^2 + $0.1\cdot N_v^{trop}$ for a horizontal resolution of $5-20$ km; cf. Table 1).

The error components can be split in two classes: input parameter plus DOAS related uncertainties (cloud, albedo, aerosol, stratosphere, slant column) and a-priori related uncertainties (profile shape). In Rodgers optimal estimation formalism [Rodgers, 2000] the latter may be called the smoothing error. It depends on the use of the data which uncertainty should be used. When the NO_2 vertical columns are used without knowledge of the NO_2 profiles, then the uncertainty, $\Delta N_{v,NO_2}^{trop,kernel}$, is the sum of input parameter, DOAS and smoothing. When profile information is available (e.g. when comparisons with models are performed) and the kernels are used, the uncertainty, $\Delta N_{v,NO_2}^{trop}$, is the sum of input parameter and DOAS only, without the smoothing error contribution. Both uncertainty estimates for the tropospheric vertical column are made available in the product: one for applications with the kernel, one for applications without.

The individual components of the total uncertainty of the tropospheric column are available in the code and provided in the NO_2 data files of the QA4ECV project ([RD6], [ER7]). In the current TROPOMI NO_2 processor (mid-2017) only the total error is made available in the data product. In the next upgrade we may consider to add the tropospheric column error components due to the slant column uncertainties, stratospheric estimate and the air-mass factor, and contributions of this AMF uncertainty due to cloud fraction, cloud pressure, albedo and profile shape uncertainties.

9 Validation

9.1 Routine validation & validation activities

The routine validation of TROPOMI is organised through the S5P Mission Performance Centre (MPC), see [ER21]. Since November 2018 the MPC generates routine validation results for the TROPOMI Level-2 products in the form of up-to-date validation results and consolidated quarterly validation reports (ROCVR, available via [ER4]). These validation activities are coordinated through the MPC VDAF website [ER22]. Further validation is performed by the S5P Validation Team (S5PVT) members.

The MPC validation activities include comparisons with MAX-DOAS and PANDORA observations (to evaluate the tropospheric column), SAOZ observations (to evaluate the stratospheric column), and satellite observations (comparisons with OMI in particular); see, for example, Griffin et al. [2019], Ialongo et al. [2020], Van Geffen et al. [2020], Verhoelst et al. [2021], Zhao et al. [2020], Van Geffen et al. [2022]. On top of the routine MPC activities, the TROPOMI data has been and will be compared to any campaign data organised by Europe and partners outside Europe.

9.2 Algorithm testing and verification

Algorithm testing and verification by the S5PVT before launch provided confidence in the retrieval algorithms, including forward and inverse models, based on simulations, and comparisons between different techniques and software programs, as described in [RD25]. That activity also included reviews and updates of the TROPOMI NO_2 ATBD.

Verification covers a wide range of activities, including:

- Testing of all the individual input datasets (albedo, cloud parameters, surface properties, snow and ice data) and comparisons with alternative input datasets and measurements when available.
- Testing of the air mass factor calculations by comparing with alternative radiative transfer calculations [Lorente et al., 2017].
- Comparisons with alternative retrieval approaches, such as the scientific retrievals performed by the university of Bremen, or approaches that start from the operational TROPOMI data and aim to improve the air-mass factors (Liu et al. [2020]; Griffin et al. [2019]).
- Study the impact of alternative (high-resolution) a-priori profile shapes from for instance regional air quality modelling systems (Laughner et al. [2019]; Marecal et al. [2015]; Liu et al. [2020]; Griffin et al. [2019]).

9.3 Stratospheric NO_2 validation

For stratospheric NO_2 columns, correlative (column and profile) measurements are needed in regions that are representative for a complete zonal band, and hence need to be relatively unpolluted. The currently operational NDACC ZSL-DOAS/SAOZ instruments are a key dataset to evaluate the stratospheric column (e.g. Verhoelst et al. [2021], Dirksen et al. [2011] and the S5P MPC validation reports [ER4]). Additional routine information comes from the Pandonia Global Network (PGN) remote and/or high altitude stations.

In our view a priority of the stratospheric validation efforts should be a better characterisation of the spatial and seasonal variations of the vertical profile of stratospheric NO_2. These profile shapes are an essential input to the data assimilation system in use for the separation between tropospheric and stratospheric NO_2 columns from the TROPOMI measurements. Useful sources of stratospheric NO_2 profile data are satellite instruments that measure in limb view, SCIAMACHY (Beirle et al. [2010], Hilboll et al. [2013b]), HIRDLS and MLS [Belmonte et al., 2014], OSIRIS [Adams et al., 2016]. Note that there are difficulties in using these for direct validation as they are often only sparsely validated themselves.

Stratospheric NO_2 measurements near the Arctic vortex in late winter and early spring would be useful to better test the capability of the data assimilation scheme (and other stratosphere-troposphere separation schemes) in capturing the influence of stratospheric air masses low in NO_x on stratospheric NO_2 at lower latitudes. Such excursions are known to occur and may lead to systematic errors in the separation scheme (e.g. Dirksen et al. [2011]; Bucsela et al. [2013]). Independent measurements may provide further important information on how to improve these issues in the future.

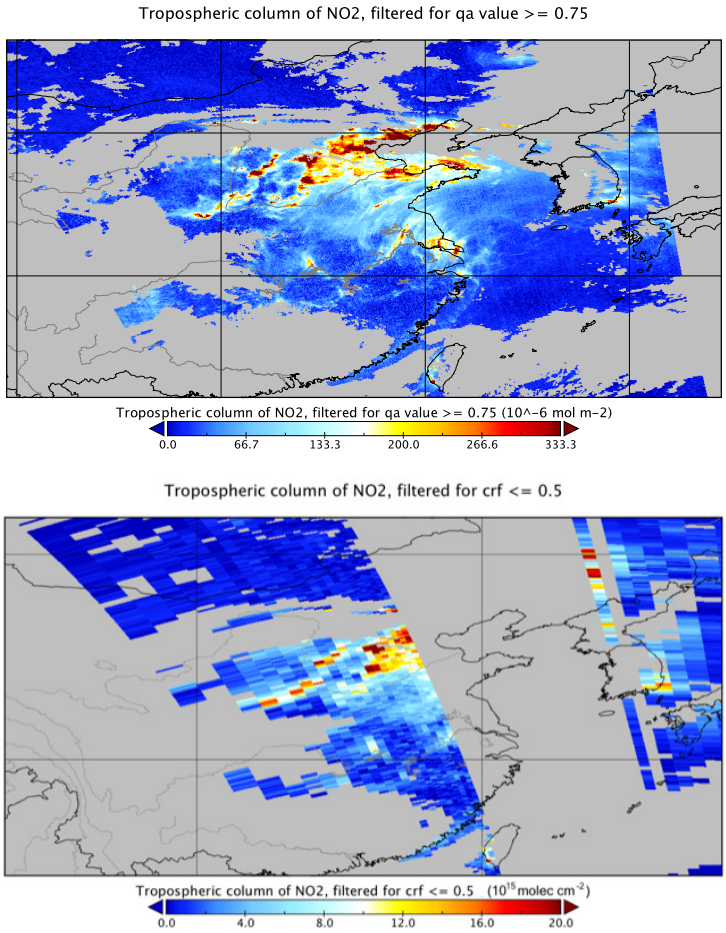

Figure 29: Tropospheric NO_2 vertical column values retrieved from TROPOMI observations (*top panel*) on 23 February 2018 (unit μ mol/m^2), compared with the corresponding OMI NO_2 tropospheric column observations for the same day (*lower panel*) (unit 10^{15} molec/cm^2). The scales have been chosen to allow a quantitative comparison. Note that the OMI data has been stripe corrected, while no stripe correction was applied to TROPOMI.

9.4 Tropospheric NO_2 validation

Information on tropospheric NO_2 concentrations – with the NO_2 in the planetary boundary layer and/or in the free troposphere – comes from in-situ instruments (at the ground, in masts, on aircraft or on low-flying balloons) and from remote-sensing instruments at the ground, on balloons or aircraft.

For the validation of TROPOMI tropospheric NO_2 columns, correlative (column and profile) measurements are needed in the highly populated polluted regions at mid-latitudes, and also in regions with natural sources of nitrogen oxides, e.g. from biomass burning, microbial soil activity and lightning. The expanding networks of MAX-DOAS and PANDORA (PGN) instruments are used as backbone for tropospheric column validation in the MPC VDAF validation reports ([ER4]; Verhoelst et al. [2021]).

Aircraft remote sensing tropospheric column observations with high spatial resolution mapping instruments is also a very valuable source of validation data for TROPOMI, (e.g. Nowlan et al. [2016], Judd et al. [2020], Tack et al. [2021]). In this way the impact of the fine-scale horizontal variability in NO_2 can be quantified.

The local overpass time of OMI and TROPOMI are nearly identical. This implies that a direct comparison of OMI and TROPOMI for (nearly) overlapping orbits is a key element of the TROPOMI validation and is also reported in the MPC VDAF validation reports [ER4]. An early example of this is shown in Fig. 29. The figure demonstrates a good quantitative agreement between OMI and TROPOMI measurements, but also demonstrates the good agreement between the OMI-QA4ECV and TROPOMI retrieval software.

Important for the validation as well as for the data assimilation system in use for the separation between tropospheric and stratospheric NO_2 columns from the TROPOMI measurements is a good understanding of the vertical profile of the tropospheric NO_2. The best source of information on vertical profiles of NO_2 is

still from incidental aircraft campaigns. Apart from this, routine profile measurements with aircraft, such as provided by a recent extension of the IAGOS programme [ER23] are very valuable. Alternatively, experimental NO_2 profiles from (tethered) balloon sondes and measurement towers, will provide valuable information on the vertical distribution of NO_2.

Since tropospheric retrievals depend on the concept of the air-mass factor, which has to rely on a-priori information, it is important to also validate the inputs and assumptions that go into the air-mass factor calculation. This mostly concerns cloud parameters – cloud fraction and cloud pressure – that should be well characterised. Another critical issue, about which very little is known as yet, is the effect of the presence of aerosols on the NO_2 retrieval. Collocated information on the aerosol profile – e.g. coming from the TROPOMI Aerosol Layer Height data product – could be useful for this. There is also a need for correlative surface albedo data to investigate the accuracy of the surface albedo climatology.

Despite the routine validation activities, based on a large number of measurement instruments and sites, the quantification of the biases in the TROPOMI retrievals remains a difficult task. This difficulty is related to several factors, e.g. the uncertainty of the independent surface remote sensing NO_2 data used for the validation, large differences in the sensitivity profiles between e.g. MAXDOAS and TROPOMI, and the issue of representativity of the local ground-based and in-situ measurements w.r.t. the finite-sized satellite ground pixels (of order 5×5 km^2), given the large fine-scale variability of NO_2 close to the surface.

10 Conclusion

We have presented the baseline approach for the retrieval of the operational tropospheric and stratospheric NO_2 column products from the TROPOMI sensor. The NO_2 data are deliverd both as an off-line product for the NO_2 data record and as a near-real time product, with the NO_2 data delivered within 3 hours after observation. The TROPOMI NO_2 data products pose an improvement over previous NO_2 data sets, particularly in their unprecedented spatial resolution (approximately 7.0×3.5 km^2 or, since the along-track pixel size reduction on 6 Aug. 2019, 5.5×3.5 km^2 at nadir), high signal-to-noise and daily global coverage, but also in the separation of the stratospheric and tropospheric contributions of the retrieved slant columns, and in the calculation of the air-mass factors used to convert slant to total columns.

The backbone of the retrieval system is the TM5-MP chemistry transport model, that is operated at a global resolution of $1^\circ \times 1^\circ$. The assimilation of NO_2 slant columns in TM5-MP ensures that the modelled stratospheric state becomes consistent with the TROPOMI slant columns over regions with small tropospheric NO_2 amounts. The information from the data assimilation system is used to separate the slant column into its stratospheric and tropospheric components and to provide the a-priori NO_2 vertical profile required by the air-mass factor calculation.

For each TROPOMI pixel an air-mass factor (AMF) is calculated, using altitude-dependent AMFs from a look-up table calculated with the DAK radiative transfer model, in combination with the vertical distribution of NO_2 provided by the TM5-MP chemistry transport model (in assimilation mode) at a spatial resolution of $1^\circ \times 1^\circ$. The AMF calculation uses local surface albedos from the OMI surface reflectance climatology that is based on 5 years of OMI measurements. It accounts for cloud scattering using information on effective cloud fraction and cloud pressure retrieved for every TROPOMI pixel from the reflectance at the AMF wavelength and from the FRESCO retrieval algorithm, respectively.

Several additional algorithm improvements w.r.t. the OMI / DOMINO v2 processing have been implemented, such as the inclusion of additional reference spectra in the DOAS spectral fit to improve the accuracy of the retrieved NO_2 slant columns, major updates to the data assimililation / chemistry transport model used to determine the vertical column densities, and a more careful quality filtering of the measurements, reflected in the `qa_value`. Part of these improvements were developed during the European QA4ECV project. Residuals resulting from tests with the TROPOMI prototype fitting algorithm on OMI spectra suggest a need to include absorption by liquid water, in any case over cloud-free ocean scenes without substantial oceanic chlorophyll. Revisiting the OMI spectra also re-emphasised the importance of an appropriate spectral calibration that is representative for the complete fitting window. Using TM5-MP at a spatial resolution of $1^\circ \times 1^\circ$ (instead of a lower spatial resolution) has been shown to provide more accurate estimates of the NO_2 profiles. The conversion of the slant to vertical columns has been improved by using an air-mass factor look-up table with more nodes, in order to reduces interpolation errors.

The TROPOMI NO_2 processing chain enables us to provide a realistic error budget. The retrieval error is dominated by the spectral fitting error over oceans and regions with low tropospheric NO_2 amounts. Over the polluted regions, air-mass factor errors contribute substantially to the overall error, which can be generally approximated as 0.5×10^{15} molec/cm$^2 + 25\%$ for an individual pixel.

Besides a complete error analysis, the TROPOMI data product also provides the averaging kernel, which describes the sensitivity of TROPOMI to NO_2 in each model layer, for every pixel. The averaging kernel is especially relevant for data users who wish to minimise the discrepancies between the assumptions in the TROPOMI retrieval and their own application of interest, e.g. for data assimilation, validation, or comparison studies.

TROPOMI's high spatial resolution enables monitoring NO_2 columns with an unprecedented accuracy, both in the troposphere and the stratosphere. From these measurements we learn more about the distribution of NO_2, its sources and sinks, its transport through the atmosphere, its role in stratospheric and tropospheric chemistry, as well as in climate issues, notably through the important role that nitrogen oxides play in the formation of secondary pollutants ozone and aerosol. The early-afternoon NO_2 data record, which started with OMI, is extended by TROPOMI, alongside the mid-morning measurements of the GOME-2 instruments, and Sentinel-5 in the near future, thus providing essential information on the diurnal cycle of NO_2. Over the past 20-odd years various UV/Vis backscatter instruments have been used to monitor NO_2 on a global scale. The operational TROPOMI NO_2 data processing is consistent with the NO_2 retrieval record generated at KNMI, and will continue and improve that record.

A Wavelength calibration

The S5P/TROPOMI radiance and irradiance spectra in the Level-1b input data are not wavelength calibrated, because most Level-2 processors perform a wavelength calibration on the fitting window specific to the algorithm. If the calibrations had been done in the Level 0-to-1b processor, they would have been done for the whole spectral band, and this may or may not have met the science requirements for the wavelength calibration for the Level-2 trace gas retrievals. For the wavelength calibration of the radiances an atmosphere model is needed, especially at the shorter wavelengths where ozone absorption is significant, but also the Ring effect modifies the radiance spectra in ways that have to be taken into account when calibrating the wavelength. In the unlikely case the wavelength calibration of radiance or irradiance fails, the retrieval will be performed using the respective nominal wavelenth grids.

For the calibration of a complete band or a complete detector, the calibration is split up in micro-windows, and a polynomial is drawn through the micro-windows to cover the whole band. When fitting for a specific retrieval window, a single fit covering the retrieval window is more appropriate. The model function that is used for the radiance wavelength calibration is a modified version of a DOAS fit. Sections A.1 and A.2 describe the generic wavelength fit used in most retrieval algorithms for S5P/TROPOMI, in section A.3 the actual application to NO_2 retrieval is discussed. For the irradiance calibration the same procedure is used, except that atmosphere related effects should be disabled, specifically the Ring effect should *not* be included in this fit. The polynomial order N is set to 1 for the irradiance fit.

A.1 Description of the problem

The S5P/TROPOMI Level-1b radiance spectra have a nominal wavelength scale (λ_{nom}), but this wavelength grid is not corrected for inhomogeneous slit illumination [RD12, section 28]. The measurements are also not temperature corrected, but because the instrument itself is temperature stabilized it is expected that this effect can be ignored. The Level-2 processors must correct the nominal wavelength scale of the radiance measurements for inhomogeneous slit illumination due to the presence of clouds in the field of view.

One would like to follow the calibration of the irradiance spectra, for a short wavelength interval. The range $\lambda_{\text{fit}} = [\lambda_-, \lambda_+]$ is the approximate range on which to do the wavelength calibration. To avoid non-linearities this wavelength range is tailored to the specific Level-2 algorithm. For each detector row the nominal wavelength λ_{nom} is adjusted with a wavelength offset (or: shift) w_s and a wavelength stretch w_q to find the calibrated wavelength λ_{cal}:

$$\lambda_{\text{cal}} = \lambda_{\text{nom}} + w_s + w_q \left(2\,\frac{\lambda_{\text{nom}} - \lambda_0}{\lambda_+ - \lambda_-} \right) + \cdots \tag{26}$$

with λ_0 the center of the fit window, λ_- the beginning of the fit window and λ_+ the end of the fit window. In the third term the factor 2 is used to ensure that the wavelength factor of the stretch lies in the range $[-1:+1]$. The higher order terms in Eq. (26) are ignored, even fitting w_q is optional.

A.2 Non-linear model function and Jacobian

The model function in the fit is similar to a non-linear DOAS equation. Instead of fitting the reflectance R, we fit the radiance I directly, bringing the (model) irradiance E_{mod} to the other side of the equation. The model function $\mathscr{M}$ is given by:

$$\mathscr{M}(\lambda_{\text{nom}}; a_0, \ldots, a_N, C_{\text{ring}}, w_s, w_q, N_{\text{s},0}, \ldots, N_{\text{s},M}) = P_N(\lambda^*) \cdot \exp\left(\sum_{k=0}^{n_k} -N_{\text{s},k}\sigma_k(\lambda_{\text{cal}}) \right) \cdot \left(E_{\text{mod}}(\lambda_{\text{cal}}) + C_{\text{ring}} I_{\text{ring}}(\lambda_{\text{cal}}) \right) \tag{27}$$

with λ_{cal} the calibrated wavelength as given by the first three terms in Eq. (26),

$$P_N(\lambda^*) = \sum_{k=0}^{N} a_j (\lambda^*)^j\,, \qquad \lambda^* \equiv 2\,\frac{\lambda_{\text{nom}} - \lambda_0}{\lambda_+ - \lambda_-} \tag{28}$$

a polynomial of order N, E_{mod} the reference irradiance spectrum, and I_{ring} the Ring spectrum; both E_{mod} and I_{ring} are convolved with the instrument slit function (or: instrument spectral response function; ISRF; available via [ER13]). The spectra σ_k ($k = 0, \ldots, M$) are optional absorption spectra that have a relevant impact on the radiance, for instance the O_3 absorption cross section. These additional reference spectra have also been

convolved with the ISRF, but note that the DOAS assumption still applies: this merit function is not applicable to line absorbers such as H_2O_{vap}, CH_4, CO or O_2, and will fail at wavelengths below ~ 320 nm because the profile shape of O_3 is relevant at those wavelengths. The order of the polynomial is $1 \leq N \leq 5$, depending on the length of the fit window.

The wavelength calibration fit adjusts the parameters $a_0, \ldots, a_N, C_{\text{ring}}, w_s, w_q, N_{\text{s},0}, \ldots, N_{\text{s},M}$ to minimize χ^2:

$$\chi^2 = \frac{1}{m-n} \sum_{i=0}^{m-1} \left(\frac{I_i \; - \; \mathscr{M}(a_0, \ldots, a_N, C_{\text{ring}}, w_s, w_q, N_{\text{s},0}, \ldots, N_{\text{s},M})}{\Delta I_i} \right)^2 \tag{29}$$

with I_i the measured radiance at detector pixel index i, ΔI_i the precision of this radiance, and m the number of spectral points between λ_- and λ_+. The number of degrees of freedom is m minus the number of fit parameters:

$$n = N + 1 + M + 1 + 3 \tag{30}$$

The additional 3 here is when fitting C_{ring}, w_s and w_q; if C_{ring} and/or w_q are not fitted, the number of degrees of freedom increases.

To minimize the number of function calls in the optimisation routine derivatives with respect to the fit parameters as a Jacobian matrix need to be supplied, with i the detector pixel index: The components of the Jacobian are given by Eqs. (31–35) below.

$$\frac{\partial \mathscr{M}_i}{\partial a_j} = (\lambda_i^*)^j \cdot \exp\left(\sum_{k=0}^{M} -N_{\text{s},k} \sigma_k(\lambda_{\text{cal},i}) \right) \cdot \left[E_{\text{mod}}(\lambda_{\text{cal},i}) + C_{\text{ring}} I_{\text{ring}}(\lambda_{\text{cal},i}) \right] \tag{31}$$

$$\frac{\partial \mathscr{M}_i}{\partial C_{\text{ring}}} = P_N(\lambda_i^*) \cdot \exp\left(\sum_{k=0}^{M} -N_{\text{s},k} \sigma_k(\lambda_{\text{cal},i}) \right) \cdot I_{\text{ring}}(\lambda_{\text{cal},i}) \tag{32}$$

$$\begin{aligned} \frac{\partial \mathscr{M}_i}{\partial w_s} = P_N(\lambda_i^*) \cdot \exp\left(\sum_{k=0}^{M} -N_{\text{s},k} \sigma_k(\lambda_{\text{cal},i}) \right) \times \\ \left\{ \left(-\sum_{k=0}^{M} N_{\text{s},k} \left. \frac{\mathrm{d}\sigma_k}{\mathrm{d}\lambda} \right|_{\lambda=\lambda_{\text{cal},i}} \right) \cdot \left(E_{\text{mod}}(\lambda_{\text{cal},i}) + C_{\text{ring}} I_{\text{ring}}(\lambda_{\text{cal},i}) \right) \right. \\ \left. + \left(\left. \frac{\mathrm{d}E_{\text{mod}}}{\mathrm{d}\lambda} \right|_{\lambda=\lambda_{\text{cal},i}} + C_{\text{ring}} \left. \frac{\mathrm{d}I_{\text{ring}}}{\mathrm{d}\lambda} \right|_{\lambda=\lambda_{\text{cal},i}} \right) \right\} \end{aligned} \tag{33}$$

$$\begin{aligned} \frac{\partial \mathscr{M}_i}{\partial w_q} = P_N(\lambda_i^*) \cdot \exp\left(\sum_{k=0}^{M} -N_{\text{s},k} \sigma_k(\lambda_{\text{cal},i}) \right) \times \\ \left\{ \left(-\sum_{k=0}^{M} N_{\text{s},k} \lambda_i^* \left. \frac{\mathrm{d}\sigma_k}{\mathrm{d}\lambda} \right|_{\lambda=\lambda_{\text{cal},i}} \right) \cdot \left(E_{\text{mod}}(\lambda_{\text{cal},i}) + C_{\text{ring}} I_{\text{ring}}(\lambda_{\text{cal},i}) \right) \right. \\ \left. + \left(\lambda_i^* \left. \frac{\mathrm{d}E_{\text{mod}}}{\mathrm{d}\lambda} \right|_{\lambda=\lambda_{\text{cal},i}} + C_{\text{ring}} \lambda_i^* \left. \frac{\mathrm{d}I_{\text{ring}}}{\mathrm{d}\lambda} \right|_{\lambda=\lambda_{\text{cal},i}} \right) \right\} \end{aligned} \tag{34}$$

$$\frac{\partial \mathscr{M}_i}{\partial N_{\text{s},k}} = -P_N(\lambda_i^*) \cdot \sigma_k(\lambda_{\text{cal},i}) \cdot \exp\left(\sum_{k=0}^{M} -N_{\text{s},k} \sigma_k(\lambda_{\text{cal},i}) \right) \cdot \left(E_{\text{mod}}(\lambda_{\text{cal},i}) + C_{\text{ring}} I_{\text{ring}}(\lambda_{\text{cal},i}) \right) \tag{35}$$

The reference spectra $E_{\text{mod}}(\lambda)$, $I_{\text{ring}}(\lambda)$ and $\sigma_k(\lambda)$ are pre-convolved with the ISRF. During the fitting 4th degree splines are used to represent these spectra. An interesting feature is that a spline of the derivative with respect to the independent variable can be calculated from the parameters of the original spline (given that the derivatives are w.r.t. the wavelength, the resulting spline for these derivaties is 3rd degree).

These equation can be solved with various optimization routines, for instance Levenberg-Marquardt or Gauss-Newton, with or without constraints or regularization methods. After thorough testing the optimal estimation method as implemented in DISAMAR, which is based on Rodgers [2000] and uses an unmodified Gauss-Newton to find the state vector for the next iteration, was selected for the S5P/TROPOMI wavelength calibration. For this usage, the a-priori error estimates are set very large (see Sect A.2.1), so that these do not limit the solution, and a pre-whitening of the data is performed to improve numerical stability.

A.2.1 Prior information for the optimal estimation fit

Optimal estimation needs prior information for the regularisation process during the fitting procedure, both a starting value and a covariance value. For input only the diagonal elements of the covariance matrix are specified, on output a full posteriori error covariance matrix is available. The polynomial coefficients are not important, the values and variance were estimated from a large number of retrievals. The Ring coefficient was taken from the same data set. The value for w_s is taken from the spacing of the nominal grid. A 1-σ error of a third of the spacing of the wavelength grid seems reasonable: $\sigma_{\text{prior}}(w_s) = \Delta\lambda/3$. This value will mostly prevent fitting a shift w_s that is larger than half of the grid spacing, which basically means the wavelength is not known at all. The prior value for w_q is 0 (zero), i.e. no stretch or squeeze. The range depends on the size of the fitting window, a consequence of the use of λ^*, as defined in Eq. (28). The current value is a deliberate overestimation. The slant column of O_3 is typically 0.18 mol/m^2 (about 600 DU); other trace gases are not included. An overview of the prior information used for S5P/TROPOMI is given in Table 16.

Table 16: A-priori values and a-priori error for the optimal estimation wavelength fit for S5P/TROPOMI. The ozone slant column is expressed in mol/m^2; the other quantities are dimensionless.

Names	a_0	a_1	$a_{2,\ldots,N}$	C_{ring}	w_s	w_q	N_{s,O_3}
Prior	1	-0.5	0.01	6×10^{-2}	0	0	0.25
Covariance	$(1)^2$	$(0.5)^2$	$(0.1)^2$	$(6\times10^{-2})^2$	$(\Delta\lambda/3)^2$	$(0.1)^2$	$(0.18)^2$
Optional	no	no	yes	yes	no	yes	yes

A.3 Application of the wavelength calibration in NO_2

For the retrieval of NO_2 the N_{s,O_3} is not fitted, as O_3 shows little structure and is a weak absorber in band 4, where the slant columns of NO_2 (window $405-465$ nm) and O_2–O_2 (window $460-490$ nm) are fitted.

Testing with OMI [RD26] has shown that there is no significant amount of stretch in the wavelength of the spectra of that instrument in the $405-465$ nm range and given the similarities of the OMI and S5P/TROPOMI detectors, no significant stretch was expected for S5P/TROPOMI. This has been confirmed using retrieval results for a S5P/TROPOMI orbit, which resulted in a very small stretch with a precision larger than the stretch itself, and a negligible effect on the retrieval results [Van Geffen et al., 2020], and hence the w_q fit parameter will remain turned off.

The order of the polynomial in Eq. (28) is set to 2 and the Ring effect is included in the fit. The a-priori error of w_s is set to 0.07 nm.

B High-sampling interpolation

After the wavelength calibration of the radiance spectrum, discussed in App. A, the irradiance and radiance observations need to be brought to the same wavelength grid in order to be able to compute the reflectance in Eq. (1). Because of the geometry of the solar observations, these measurements are shifted with respect to the radiance observations due to the Doppler shift caused by the motion of the satellite relative to the sun. Given that the irradiance spectrum is known better than the radiance spectrum, the irradiance spectrum is shifted to the radiance grid and the radiance observations are left without modification:

$$E_0\left(\lambda_{i,\text{earth}}\right) = \frac{E_{\text{high}}\left(\lambda_{i,\text{earth}}\right)}{E_{\text{high}}\left(\lambda_{i,\text{solar}}\right)}\, E_0\left(\lambda_{i,\text{solar}}\right) \tag{36}$$

with E_0 the observed irradiance, E_{high} a high resolution solar reference spectrum, convolved with the instrument spectral response function, $\lambda_{i,\text{earth}}$ the wavelength of the earth radiance spectrum for pixel i, and $\lambda_{i,\text{solar}}$ the wavelength of the solar irradiance spectrum for pixel i. The index i is synchronized between the radiance and irradiance observations, such that they refer to the same physical pixel on the detector. On E_{high} 4th degree spline interpolation is used to find the value at the indicated wavelengths. The input data for the splines have sufficient spectral resolution to allow for this.

Fig. 30 shows the procedure graphically. Panel (d) shows the effect of spline interpolation on the irradiance data to find the values at the earth radiance wavelength grid. Errors are small but systematic. Note that these errors appear directly in the reflectance data. The reflectance in Eq. (1) is then be calculated a at the radiance wavelenth grid: $R_{\text{meas}}(\lambda_{i,\text{earth}}) = \pi I(\lambda_{i,\text{earth}})/\mu_0 E_0(\lambda_{i,\text{earth}})$.

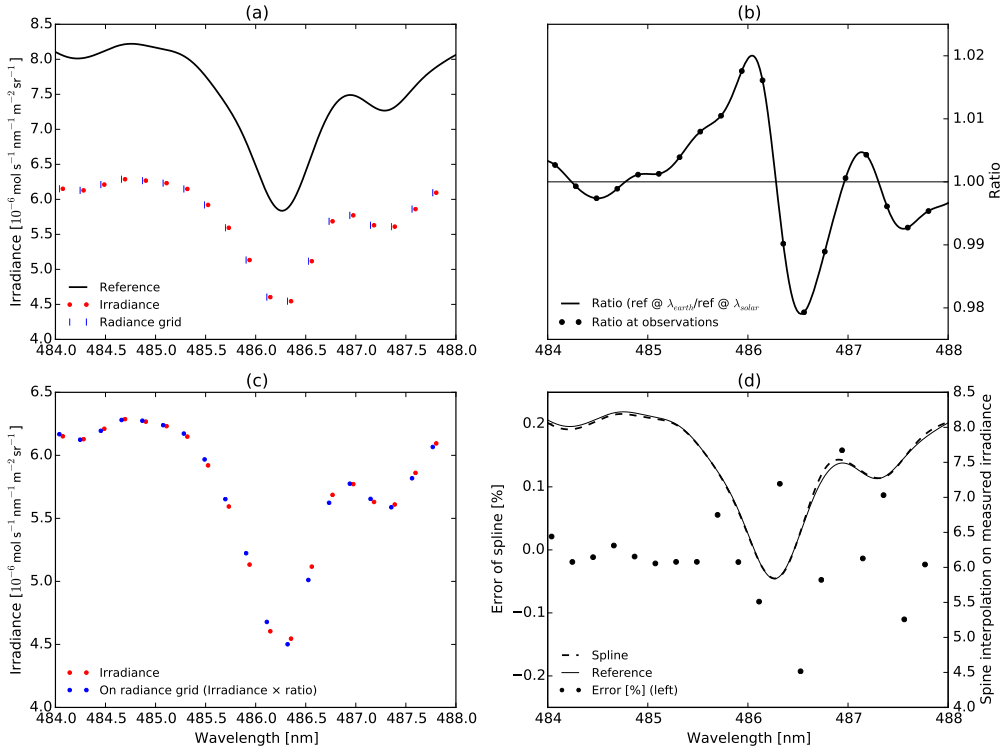

Figure 30: High sampling interpolation on part of a solar observation. (**a**) The red dots show the actual observation (taken from GOME-2A). The blue vertical lines indicate the wavelength grid of the radiance observation. The solid line shows a high resolution solar reference spectrum that has been convolved with the instrument spectral response function of the instrument (in this case GOME-2A). (**b**) The ratio $E_{\text{high}}\left(\lambda_{i,\text{earth}}\right)/E_{\text{high}}\left(\lambda_{i,\text{solar}}\right)$. (**c**) In red $E_0\left(\lambda_{i,\text{solar}}\right)$, in blue $E_0\left(\lambda_{i,\text{earth}}\right)$. (**d**) The solid line is the solar reference spectrum. The dash-dotted line is a high resolution irradiance spectrum created by spline interpolation directly on the observed irradiances, brought to the same average level of the window shown here to ease comparisons. The black dots indicate the error in % that are caused by using spline interpolation directly on the irradiance observations. Clear artifacts are caused by this, especially because noise on the observations becomes correlated between nearby points in the spectrum.

C Effective cloud fraction in the NO_2 window

The cloud radiance fraction, w_{NO_2} (Sect 6.4.3), and the effective cloud fraction, f_{eff,NO_2} (Sect. 6.4.4), in the NO_2 fit window, can be computed from a look-up table (LUT) with the top-of-atmosphere (TOA) reflectance at $\lambda_{c,NO_2} = 440$ nm as a function of viewing geometry, surface & cloud albedo, and surface & cloud pressure, based on the continuum reflectance at 440 nm of the measurement. The continuum reflectance at 440 nm could be determined from the observed spectrum, averaged over a small wavelength interval, but that may lead to unexpected values, e.g. in case of spikes in the measurement. Instead, we have opted for using the modelled reflectance of Eq. (5) evaluated at 440 nm. The approach is very similar to FRESCO [RD18] and explicitly accounts for Rayleigh scattering. The following description is adapted from [RD27].

The LUT assumes that the measured reflectance at TOA is defined as (cf. Eq. (1)):

$$R_{\mathrm{TOA}}(\lambda) = \frac{\pi I(\lambda)}{\mu_0 E_0(\lambda)} \tag{37}$$

In the independent pixel approximation the cloud faction, f_{c}, for a given wavelength is given by:

$$f_{\mathrm{c}} = \frac{R_{\mathrm{TOA}} - R_{\mathrm{s}}}{R_{\mathrm{c}} - R_{\mathrm{s}}} \tag{38}$$

and the cloud radiance fraction, the fraction of the total radiation that comes from the clouds, is given by:

$$w_{NO_2} = \frac{f_{\mathrm{c}} R_{\mathrm{c}}}{R_{\mathrm{TOA}}} = \frac{f_{\mathrm{c}} R_{\mathrm{c}}}{f_{\mathrm{c}} R_{\mathrm{c}} + (1 - f_{\mathrm{c}}) R_{\mathrm{s}}} \tag{39}$$

where R_{s} and R_{c} are the reflectances at surface and cloud, respectively. These are computed from a limited LUT, based on Chandrasekhar (Chandrasekhar [1950], Sect. 72). For bounding surface 'b', i.e. either surface ('s') or cloud ('c'):

$$R_{\mathrm{b}}(\lambda, A_{\mathrm{b}}(\lambda)) = R_0(\lambda) + \frac{A_{\mathrm{b}}(\lambda)\, T(\lambda)}{1 - A_{\mathrm{b}}(\lambda)\, s(\lambda)} \tag{40}$$

where:

$R_{\mathrm{b}}(\lambda, A_{\mathrm{b}}(\lambda))$	=	The reflectance of the combined atmosphere-surface system related to the light coming from the boundary 'b', i.e. either surface ('s') or cloud ('c').
$R_0(\lambda)$	=	The reflectance of the atmosphere if the surface is perfectly black: $A_{\mathrm{b}} = 0$.
$A_{\mathrm{b}}(\lambda)$	=	The albedo at the bounding surface, either cloud (A_{c}) or surface (A_{s}).
$T(\lambda)$	=	The transmittance of the atmosphere, a measure for the probability that photons travel through the atmosphere, are reflected by a surface with unit albedo, and travel back to the sensor (reflections by the atmosphere back towards the surface are ignored here).
$s(\lambda)$	=	The spherical albedo of the atmosphere for illumination at its lower boundary; $1/[1 - A_{\mathrm{b}}(\lambda) s(\lambda)]$ is the sum of a geometrical series accounting for the reflections between the atmosphere and the surface.

The transmittance of the atmosphere $T(\lambda)$ is a product of two terms depending on the viewing and solar zenith angles:

$$T(\lambda) = t(\lambda; \mu)\, t(\lambda; \mu_0) \tag{41}$$

where $\mu = \cos(\theta)$ and $\mu_0 = \cos(\theta_0)$ and:

$$t(\lambda; \mu) = \exp(-\frac{\tau(\lambda)}{\mu}) + \int_0^1 2\mu' T_0(\lambda; \mu, \mu')\mathrm{d}\mu' \tag{42}$$

In Eq. (42) we assume a plane parallel atmosphere; for a spherical shell atmosphere the factor $1/\mu$ in $\exp(-\tau/\mu)$ has to be replaced by a different expression.

The TOA reflectance related to the light coming from the boundary 'b', i.e. either surface ('s') or cloud ('c'), is a function of solar and viewing geometries and surface properties: $R_{\mathrm{b}}(\lambda, A_{\mathrm{b}}(\lambda)) = R_{\mathrm{b}}(\lambda; \theta_0, \theta, \phi - \phi_0; p_{\mathrm{b}}, A_{\mathrm{b}}(\lambda))$, where p_{b} is the pressure at the boundary 'b'. In addition extra dependencies may be needed to account for absorbing species, in particular at shorter wavelengths where absorption by ozone (O_3) is significant. A more

Table 17: Look-up tables and dimensions for reflectance calculations; no trace gas column entries included.

R_0		Reflectance of the black surface
	λ	For all wavelengths where a cloud fraction must be computed $[1,\ldots,n]$
	μ_0	For $\mu_0 = [0.0012141231 : 1.0]$, i.e. $\theta_0 = [89.93^\circ : 0^\circ]$, in 42 steps of $2-5^\circ$
	μ	For $\mu = [0.0012141231 : 1.0]$, i.e. $\theta = [89.93^\circ : 0^\circ]$, in 42 steps of $2-5^\circ$
	$\phi - \phi_0$	Dependency stores in three Fourier terms
	p_b	Pressure of the bounding surface (cloud or surface) for $p_\mathrm{b} = [1075$ hPa $: 95$ hPa$]$ in 68 steps *
T		Transmittance of the atmosphere
	λ	For all wavelengths where a cloud fraction must be computed $[1,\ldots,n]$
	μ_0	For $\mu_0 = [0.0012141231 : 1.0]$, i.e. $\theta_0 = [89.93^\circ : 0^\circ]$, in 42 steps of $2-5^\circ$
	μ	For $\mu = [0.0012141231 : 1.0]$, i.e. $\theta = [89.93^\circ : 0^\circ]$, in 42 steps of $2-5^\circ$
	p_b	Pressure of the bounding surface (cloud or surface) for $p_\mathrm{b} = [1075$ hPa $: 95$ hPa$]$ in 68 steps *
s		Spherical albedo of the atmosphere
	λ	For all wavelengths where a cloud fraction must be computed $[1,\ldots,n]$
	p_b	Pressure of the bounding surface (cloud or surface) for $p_\mathrm{b} = [1075$ hPa $: 95$ hPa$]$ in 68 steps *

*) Through a fixed scale height p_b is linked to the elevation of the bounding surface: $z_\mathrm{b} = [-55$ m $: 16250$ m$]$.

detailed study is needed to determine if O_3 is needed for the cloud fraction, but for NO_2 we estimate that ignoring O_3 absorption leads to an error of $0.01-0.02$ in the cloud fraction. Raman scattering is ignored here.

The terms used in Eq. (40) have the same or less dependencies: $R_0(\lambda) = R_0(\lambda;\theta_0,\theta,\phi-\phi_0;p_\mathrm{b})$, but crucially not on $A_\mathrm{b}(\lambda)$. Further: $T(\lambda) = T(\lambda;\theta_0,\theta;p_\mathrm{b})$ and $s(\lambda) = s(\lambda;p_\mathrm{b})$. The dependency of $R_\mathrm{b}(\lambda)$ and $R_0(\lambda)$ on $\phi-\phi_0$ can be expressed as a Fourier sum, in case of a Rayleigh atmosphere with three terms. All in all this gives a small set of LUTs for $R_0(\lambda)$, $T(\lambda)$ and $s(\lambda)$; see the overview in Table 17. For use in the NO_2 retrieval, the set of LUTs has been computed using DAK at $\lambda_{c,\mathrm{NO_2}} = 440$ nm, the wavelength used for the air-mass factor calculations.

From these LUTs we can calculate the reflectance of the cloudy part of the pixel, R_c, using the cloud pressure, p_c, and cloud albedo, A_c, from the cloud product. And the reflectance of the cloud-free part of the pixel, R_s, using the surface pressure, p_s, from meteorology or a fixed scale height and the surface elevation, z_s, and the surface albedo, A_s, from a climatology. Note that either p_s or z_s can be used as entry to the LUT: they are "linked" through the fixed scale height.

C.1 Adjusting albedo to respect physical limits to the cloud fraction

In order to limit the cloud fraction to the range $[0,1]$, the albedo of the boundary is adjusted to ensure radiative closure [Van Geffen et al., 2022]. From Eq. (38) it is clear that a negative cloud fraction results when $R_\mathrm{s} > R_\mathrm{TOA}$. Rewriting Eq. (40) to set $R_\mathrm{s} = R_\mathrm{TOA}$ provides an adjusted value for A_s:

$$A_\mathrm{s}(\lambda) = \frac{R_\mathrm{TOA}(\lambda) - R_0(\lambda,p_\mathrm{s})}{T(\lambda,p_\mathrm{s}) + s(\lambda,p_\mathrm{s})\,[R_\mathrm{TOA}(\lambda) - R_0(\lambda,p_\mathrm{s})]} \tag{43}$$

In a similar fashion it is clear from Eq. (38) that a cloud fraction larger than 1 results when $R_\mathrm{TOA} > R_\mathrm{c}$. Rewriting Eq. (40) to set $R_\mathrm{c} = R_\mathrm{TOA}$ provides an adjusted value for A_c:

$$A_\mathrm{c}(\lambda) = \frac{R_\mathrm{TOA}(\lambda) - R_0(\lambda,p_\mathrm{c})}{T(\lambda,p_\mathrm{c}) + s(\lambda,p_\mathrm{c})\,[R_\mathrm{TOA}(\lambda) - R_0(\lambda,p_\mathrm{c})]} \tag{44}$$

After adjustment of the albedo, the R_s or R_c – which led to the cloud fraction going outside the range $[0,1]$ – is re-computed, thus ensuring that the cloud radiance fraction $w_{\mathrm{NO_2}}$ (Sect 6.4.3) lies within $[0,1]$ as well (unfortunately $w_{\mathrm{NO_2}}$ could be >1 in v2.4.0-v2.6.0; as of v2.7.1 this coding issue is repaired).

Note that in the FRESCO cloud retrieval (Sect. 6.4.4) the surface albedo is adjusted ignoring Rayleigh scattering, which simplifies Eq. (43) to $A_s(\lambda) = R_{TOA}(\lambda)$, and Eq. (44) to $A_c(\lambda) = R_{TOA}(\lambda)$; the corrected albedos are provided in the data product.

D Surface albedo correction using the snow/ice flag

The retrieval process uses the surface albedo in the NO_2 fit window, A_{s,NO_2}, as one of the input parameters for the air-mass factor and vertical column calculations (Sect. 6.4). This surface albedo is taken from a surface albedo climatology as described in Sect. 6.4.5.

Substantial errors are introduced in the retrieval results if the real surface albedo, A_s, differs considerably from what is expected, for example in the case of the sudden snowfall or ice cover. Correcting the surface albedo from the climatology, A_{clim}, using knowledge of actual snow/ice cover (Sect. 6.4.6) will therefore improve the final data product, in terms of the retrieval itself and for flagging such cases. In processor versions up to 2.6.0, the correction of A_{s,NO_2} followed the approach included in the OMI cloud data product OMCLDO2 [Veefkind et al., 2016] to adapt the surface albedo in the O_2–O_2 fit window (i.e. at 477 nm). As of processor version 2.7.1, the albedo correction is based on the presence of improved flagging in the v2.1 DLER albedo climatology for snow/ice cases. The corrected A_{s,NO_2} is provided in the data product.

The basis for the correction are the snow/ice flag values derived from ECMWF data and sampled at the ground pixel centre coordinate (Sect. 6.4.6). Table 18 provides an overview of these flags, where an asterisk marks snow/ice flag values that lead to an adjustment of the surface albedo in case a certain threshold is exceeded.

Table 18: Overview of the snow/ice flag values f_{NISE} as defined in the NISE snow/ice data. The ECMWF snow/ice information is mapped onto these NISE flag values in a preprocessing step, and are then included in the L2 data files. Note that nrs. 252, 253 and 254 do not occur in the ECMWF-based data. Flag values marked with an asterisk may lead to adjustment of the climatological surface albedo as described in the text.

f_{NISE}	meaning	remark
000 *	snow-free land	
001-100 *	sea ice concentration (percent)	
101	permanent ice	
103 *	dry & wet snow	
252	mixed pixels at coastlines	land-ocean or snow/ice-ocean boundaries
253	suspect ice value	considered to represent an error
254	error value	
255 *	ocean	

D.1 Surface albedo adjustment as of processor version v2.7.1

The DLER v2.1 albedo climatology (Tilstra et al. [2024]; [RD21]; see Sect. 6.4.5.2) has both a 'clear' (i.e. snow-free) and a 'snice' (i.e. snow/ice) database, as well as a flag variable that indicates if a value in the 'snice' database has been taken from the 'clear' database, or the other way around.

The meaning of all values in the flag variable, f_{DLER}, is defined in Table 19, from which only the values corresponding to "empty cell replaced clear" ($f_{DLER}\&8$) and "empty cell replaced snice" ($f_{DLER}\&128$) are used; see [RD28] for full details. The following configurable constants are used below:

- Default value for the albedo over land: $A_{land} = 0.05$
- Default value for the albedo over water: $A_{water} = 0.05$
- Default value for the albedo of snow: $A_{snow} = 0.6$
- Default values for the albedo of sea ice for month M and hemisphere H: $A_{ice}(M,H)$, defined in Table 20
- Threshold for adjusting the surface albedo of sea ice: $A_{thrs} = 0.1$

Four possible cases can be distinguished for the combination of the dynamic snow/ice information given by f_{NISE} and the DLER flags given by f_{DLER}:

1. If f_{NISE} indicates there is *n*o snow or ice at the surface and f_{DLER} indicates *n*o replacement ($(f_{DLER}\&8) \equiv 0$), then the information from the 'clear' variables is used *w*ithout modifications.

2. If f_{NISE} indicates there *i*s snow or ice at the surface and f_{DLER} indicates *n*o replacement ($(f_{DLER}\&128) \equiv 0$), then the information from the 'snice' variables is used *w*ithout modifications.

3. If f_{NISE} indicates there is *n*o snow or ice at the surface and f_{DLER} indicates a replacement ($(f_{DLER}\&8) \equiv 8$), then for a pixel that is thought to be snow-free there was not enough information available before to

Table 19: Overview of the flag variable in version 2 of the DLER database [RD28].

f_{DLER}	mask	description
1	7	no corrections applied clear
2	7	cloud contamination fixed clear
3	7	cloud contamination remains clear
4	7	cell replaced by donor cell clear
5	7	no donor cell found clear
6	7	unphysical value clear
8	8	empty cell replaced clear
16	112	no corrections applied snice
32	112	cloud contamination fixed snice
48	112	cloud contamination remains snice
64	112	cell replaced by donor cell snice
80	112	no donor cell found snice
96	112	unphysical value snice
128	128	empty cell replaced snice

construct a snow-free surface albedo in the database: the 'clear' database has been filled using data from the 'snice' database. In that case the recipe previously used (Sect. D.2) is used to construct an estatimate of the surface albedo that is snow-free:

- Constructing a snow-free albedo
  Adjust A_{s} to a default value A_{def} rather than using A_{clim}, where A_{def} is either A_{land} for scenes over land or A_{water} for scenes over water.

4. If f_{NISE} indicates there *i*s snow or ice at the surface and f_{DLER} indicates a replacement ($(f_{\text{DLER}}\&128) \equiv 128$), then for a pixel that that is thought to have snow or ice there was not enough information available before to construct a snow or ice surface albedo in the database: the 'snice' database has been filled using data from the 'clear' database. In that case the recipe previously used (Sect. D.2) is used to construct an estatimate of the surface albedo having snow or ice:

   - Constructing a snow albedo over land
     Adjust A_{s} to a default value for snow A_{snow} rather than using A_{clim}.
   - Constructing a snow albedo over water
     Adjust A_{s} if the difference between A_{clim} and a default value A_{def} is larger than a given threshold

Table 20: Values for A_{ice}. Since the wavelenth range under consideration excludes the SWIR bands (bands 7 and 8 of TROPOMI), it is reasonalbe to assume that ice is 'white' and therefore that the bright surface of ice has a wavelength independent albedo.

	Hemisphere H	
month M	North	South
January	0.70	0.53
February	0.73	0.50
March	0.76	0.44
April	0.80	0.60
May	0.84	0.61
June	0.78	0.64
July	0.61	0.68
August	0.61	0.76
September	0.62	0.80
October	0.68	0.83
November	0.67	0.78
December	0.71	0.66

A_{thrs}:

$$A_{\text{s}} = \begin{cases} A_{\text{def}} & \text{if } |A_{\text{clim}} - A_{\text{def}}| > A_{\text{thrs}} \\ A_{\text{clim}} & \text{otherwise} \end{cases}$$

where A_{def} depends on the the sea-ice fraction f_{NISE}, the month of the year M and on which hemisphere H the ice is found:

$$A_{\text{def}} = (1.0 - 0.01 \cdot f_{\text{NISE}}) A_{\text{water}} + 0.01 \cdot f_{\text{NISE}} \cdot A_{\text{ice}}(M,H)$$

with A_{ice}(M,H) tabulated in Table 20.

This procedure from the v2.1 DLER makes the albedo over snow and ice covered pixels more realistic. Note, however, that the NO_2 processor does not use this DLER information over snow/ice. The scene albedo from the cloud product is used instead.

D.2 Surface albedo adjustment in processor versions up to v2.6.0

For reference sake, the following text is kept as-is.

The rules for modifying the climatological surface albedo A_{clim} are as follows:

- In case of snow-free land or open ocean (f_{NISE} equal 0 or 255) adjust A_{s} if the difference between A_{clim} and default value $A_{\text{def}} = 0.04$ is larger than a given threshold $A_{\text{thrs}} = 0.1$, where the albedo is decreased only if $A_{\text{clim}} > A_{\text{snow}} = 0.6$.

  $\underline{\text{if}} \quad ((A_{\text{clim}} - A_{\text{def}}) > A_{\text{thrs}} \;\&\; A_{\text{clim}} > A_{\text{snow}}) \quad \underline{\text{then}} \quad A_{\text{s}} = A_{\text{def}} \quad \underline{\text{else}} \quad A_{\text{s}} = A_{\text{clim}}$

- In case of dry or wet snow (flag $f_{\text{NISE}} = 103$) adjust A_{s} if the difference between A_{clim} and $A_{\text{snow}} = 0.6$ is larger than a given threshold $A_{\text{thrs}} = 0.1$.

  $\underline{\text{if}} \quad ((A_{\text{clim}} - A_{\text{snow}}) > A_{\text{thrs}}) \quad \underline{\text{then}} \quad A_{\text{s}} = A_{\text{snow}} \quad \underline{\text{else}} \quad A_{\text{s}} = A_{\text{clim}}$

- In case of a non-zero sea ice concentration (flags $f_{\text{NISE}} = 1 - 100$) adjust A_{s} if the difference between A_{clim} and a default value A_{def} is larger than a given threshold $A_{\text{thrs}} = 0.1$.

  $\underline{\text{if}} \quad (|A_{\text{clim}} - A_{\text{def}}| > A_{\text{thrs}}) \quad \underline{\text{then}} \quad A_{\text{s}} = A_{\text{def}} \quad \underline{\text{else}} \quad A_{\text{s}} = A_{\text{clim}}$

  where A_{def} depends on the month of the year M and on which hemisphere H the ice is found:

  $A_{\text{def}} = (1.0 - 0.01 \cdot f_{\text{NISE}}) * 0.065 + 0.01 \cdot f_{\text{NISE}} \cdot A_{\text{ice}}(M,H)$

  with $A_{\text{ice}}(M,H)$ following from the LUT used to determine the OMI surface albedo database [Kleipool et al., 2008]:

  $A_{\text{ice}}(M,\text{'north'}) = 0.70,\ 0.73,\ 0.76,\ 0.80,\ 0.84,\ 0.78,\ 0.61,\ 0.61,\ 0.62,\ 0.68,\ 0.67,\ 0.71$

  $A_{\text{ice}}(M,\text{'south'}) = 0.53,\ 0.50,\ 0.44,\ 0.60,\ 0.61,\ 0.64,\ 0.68,\ 0.76,\ 0.80,\ 0.83,\ 0.78,\ 0.66$

E Data quality value: the `qa_value` flags

To make the use of the TROPOMI data products easier, a so-called `qa_value` (where 'qa' stands for 'quality assurance') is assigned to each ground pixel. The `qa_value` is intended to serve as an easy filter of the observations (dividing the dataset in useful versus not useful observations), depending on how the data is used.

The data files have for each ground pixel the so-called `processing_quality_flags`, which provides the user information on processing issues, such as errors that were encountered in the processing, as well as a number of warnings. Some of these warnings have been included in the `qa_value`. The meaning of the `processing_quality_flags` values is detailed in App. A of the NO_2 Product User Manual (PUM; available via [ER2]).

The following differentiation of the `qa_value`, f_{QA}, for usage of the NO_2 data product has been made:

$0.75 \leq f_{\mathrm{QA}} \leq 1.00$	The ground pixel is recommended for all applications, including column comparisons, visualisation, trends, monthly/seasonal averages. The data is restricted to cloud-free observations (cloud radiance fraction < 0.5), and snow-ice free observations.
$0.50 \leq f_{\mathrm{QA}} < 0.75$	The ground pixel is recommended for use in data assimilation and comparisons against models or vertical profile observations, given that the averaging kernel is used to specify the sensitivity profile in cloudy situations; this includes good quality retrievals over clouds and snow/ice.
$0 < f_{\mathrm{QA}} < 0.50$	The ground pixel is not recommended for use due to serious retrieval issues.
$f_{\mathrm{QA}} = 0$	A processing error occurred so that the ground pixel cannot be used at all, or the solar zenith angle exceeds the limit set in the data assimilation

The determination of the `qa_value` is done as follows. Starting from the initial value $f_{\mathrm{QA}} = 1$, f_{QA} is multiplied by the modification factor f^i_{QA} of each of the criteria i listed in Table 21 (see next page) that have been met (i.e. if criterion i is not met then $f^i_{\mathrm{QA}} = 1$).

Observations made in the descending part of the orbit, flagged as `descending` set in `geolocation_flags`, get a special treatment for the `qa_value` since v2.7.1 (cf. Fig. 31). Observations with small albedo values (e.g. open water over the Arctic Sea) or high solar zenith angle are observed to deviate from the ascending node observations for the same location (same day, other orbit) and therefore receive a `qa_value` < 0.5, see criteria 17–19 in Table 21.

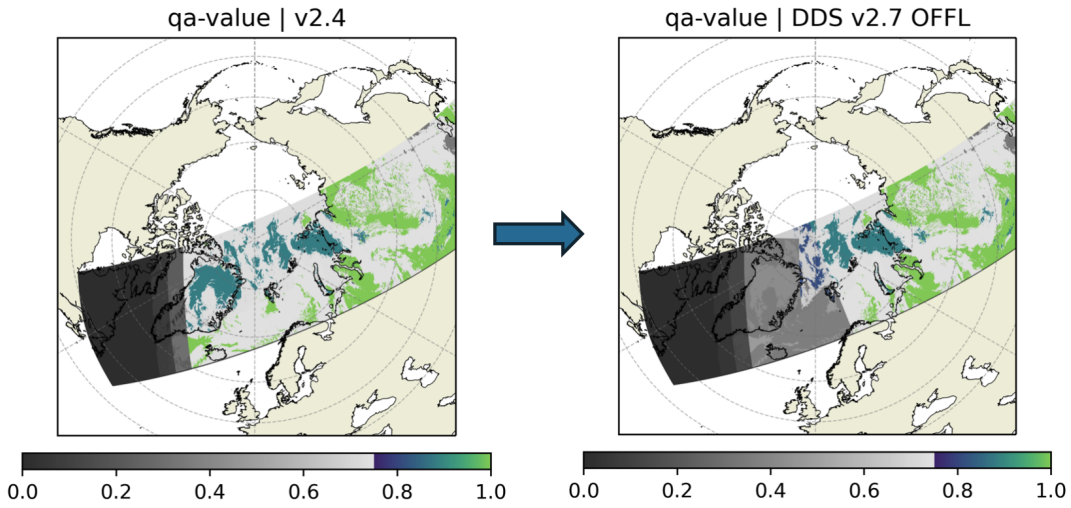

Figure 31: The change in the `qa_value` for the Arctic measurements on 16 June 2021 between v2.4.0 and v2.7.1. In v2.7.1 the `qa_value` is reduced for a large fraction of the descending node observations. Grey and black indicate that the `qa_value` < 0.75.

Table 21: Overview of the selection criteria for the `qa_value`, f_{QA}, for the version v2.2.0 (viz. Table 2); previous versions may have different settings. Some quantities have a minimum or maximum value; these values are configuration parameters in the processing. In this table f_{NISE} stands for the snow/ice flags listed in Table 18 and used by both the NISE and ECMWF snow/ice data sets. And f_{AAI} represents the aerosol index $354/388$ nm pair, which is passed on to the NO_2 data product file as added flag. Warning flags in `processing_quality_flags` not used for f_{QA} are not listed.

i	criterion	f^i_{QA}
0	if fatal error encountered according to `processing_quality_flags`	0.00
1	if `south_atlantic_anomaly_warning` set in `processing_quality_flags`	0.95
2	if `sun_glint_warning` set in `processing_quality_flags` and $f_{NISE} = 255$	0.93
3	if `pixel_level_input_data_missing_warning` set in `processing_quality_flags`	0.90
4	if `interpolation_warning` set in `processing_quality_flags`	0.90
5	if `solar_eclipse` set in `geolocation_flags`	0.20
5b	if `spacecraft_manoeuvre` set in `geolocation_flags` ‡	0.10
6	if $\theta_0 > \theta_0^{max,1} = 81.2°$	0.30
7	if $\theta_0 > \theta_0^{max,2} = 84.5°$	0.10
8	if $M^{trop}/M^{geo} < M^{trop}_{min} = 0.1$	0.45
9	if $\Delta N_s > (\Delta N_s)^{max} = 33.0\times10^{-6}$ mol/m^2 ($= 2\times10^{15}$ molec/cm^2)	0.15
	if $f_{NISE} < f^{max}_{NISE} = 1$ * or $f_{NISE} = 252$ or $f_{NISE} = 255$ [no snow or ice]	
10	if $A_{s,NO_2} > A^{max}_s = 0.3$	0.20
11	if $w_{NO_2} > w^{max}_{NO_2} = 0.5$	0.74
	else-if ($f_{NISE} \neq 253$ and $f_{NISE} \neq 254$) [snow/ice case]	
12	if ($f_{NISE} > 80$ and $f_{NISE} < 104$ and $p_{sc} > 0.97\,p_s$ †) [cloud-free snow/ice]	0.88
13	else [cloudy snow/ice]	0.73
14	if $p_{sc} < p^{min}_{sc} = 3.0\times10^4$ Pa	0.25
15	else [snow/ice error]	0.00
16	if $f_{AAI} > f^{max}_{AAI} = 1.0\times10^{10}$ [for future use]	0.40
	if `descending` set in `geolocation_flags`	
17	if measurement time = local solar afternoon / evening §	0.92
	if measurement time = local solar morning §	
18	if $A_{s,NO_2} > 0.4$ and $\theta_0 < 70°$	0.92
19	else [problematic observation]	0.48

* Note that this criterion means that the system switches to the scene mode if there is 1% or more snow/ice.

† In NO_2 data versions prior to v1.4.0 the threshold was $0.98\,p_s$,
from v1.4.0 up to v2.6.0 the threshold was $0.96\,p_s$.
and for v2.7.1 the threshold was $0.94\,p_s$.
while as of v2.8.0 the threshold is $0.97\,p_s$.

‡ This criterion has been in the code since the beginning but was missing from the list before v2.7.1.

§ Local solar time is the time in UTC $+ 12 \cdot$ longitude / $180°$, with local solar noon at 13:30:00.

F Spike removal in the DOAS fit

In version 2.2.0 of the TROPOMI NO_2 processor a "spike removal" was implemented into the DOAS fit (Sect. 6.2), to remove strong outliers in the fit residual. Such outliers may be caused by, e.g., high-energy particles hitting the CCD detector (so-called transients), variations in the dark current, or bad pixels not correctly flagged in the Level-1b data. After removal of an outlier from the measured reflectance, the NO_2 DOAS fit is redone. To avoid ending up in a cycle, the new fit residual is not checked again for outliers.

To detect outliers the so-called box-plot method used by Veefkind et al. [2016] for the OMI O_2–O_2 cloud algorithm is implemented. This method [ER24] determines lower and upper values based on the first and third quartiles, Q_1 and Q_3, i.e. the 25th and 75th percentile of a distribution (the second quartile, Q_2, is the median). For data with a Gaussian distribution $Q_1 = -0.67$ and $Q_3 = +0.67$, which means that for normally distributed data, one-half of the data is within 2/3-rd of a standard deviation unit of the mean [ER25].

If a certain value is larger than $Q_3 + Q_f \cdot Q_{3-1}$ or lower than $Q_1 - Q_f \cdot Q_{3-1}$, with $Q_{3-1} = Q_3 - Q_1$ the inter-quartile range and Q_f a suitable multiplication factor, it is termed an outlier. If Q_f is set too low, valid observations are unjustly removed from the fit and the NO_2 SCD error will be underestimated.

For the so-called inner fences, defined by $Q_f = 1.5$ [ER24] and used by Veefkind et al. [2016], 0.74% of normally distributed data is termed an outlier [ER25]. This means that on average for each TROPOMI ground pixel 2 or 3 wavelength pixels will be designated as outlier, if the NO_2 fit residual on the 304 or 305 wavelength pixels within the NO_2 fit window would be normally distributed. In reality the fit residual is not normally distributed but drops off less steep, hence $Q_f = 1.5$ is clearly too low a factor to use, as this would inevitably lead to the removal of valid observations.

For the so-called outer fences, defined by $Q_f = 3.0$ [ER24], about 0.002% of normally distributed data is termed an outlier [ER26], or in terms of the NO_2 fit window about 1/100-th of a wavelength pixel (i.e. roughly one wavelength pixel per 100 ground pixels), so that the chance that valid observations are removed is small. Based on this evaluation, the TROPOMI NO_2 processor is configured to use $Q_f = 3.0$.

Figure 32 shows two examples of outlier detection. The fit residual in the *left panel* has one modest outlier, at a level of $Q_f = 3.51$. Removing this one spike, the NO_2 SCD changes from $14.9445 \times 10^{15} \pm 0.6752 \times 10^{15}$ molec/cm^2 to $14.8626 \times 10^{15} \pm 0.6599 \times 10^{15}$ molec/cm^2 ($2.4680 \pm 0.1096 \times 10^{-4}$ mol/m^2), while the RMS error decreases by 3.7% from 5.0822×10^{-4} to 4.8928×10^{-4}. The *right panel* shows the effect on the fit residual of the impact of a high-energy partical in the South Atlantic Anomaly, which appears to be so massive that it affects two neighbouring wavelength pixels as well, while the three ground pixels to the east of this one also have outliers at the same wavelength pixels, showing that the high-energy partical hit the detector under a slant angle. The main outlier has a level of $Q_f = 69.04$, while the two neighbouring pixels have levels of $Q_f = 18.64$ and $Q_f = 14.28$. For this pixel removing these three wavelength pixels changes the NO_2 SCD from an unrealistically low value with large error ($4.8324 \pm 4.5284 \times 10^{15}$ molec/cm^2) to a more realistic $6.8079 \pm 0.6510 \times 10^{15}$ molec/cm^2 ($1.1305 \pm 0.1081 \times 10^{-4}$ mol/m^2), while the RMS error decreases from 33.4750×10^{-4} to 4.4143×10^{-4}.

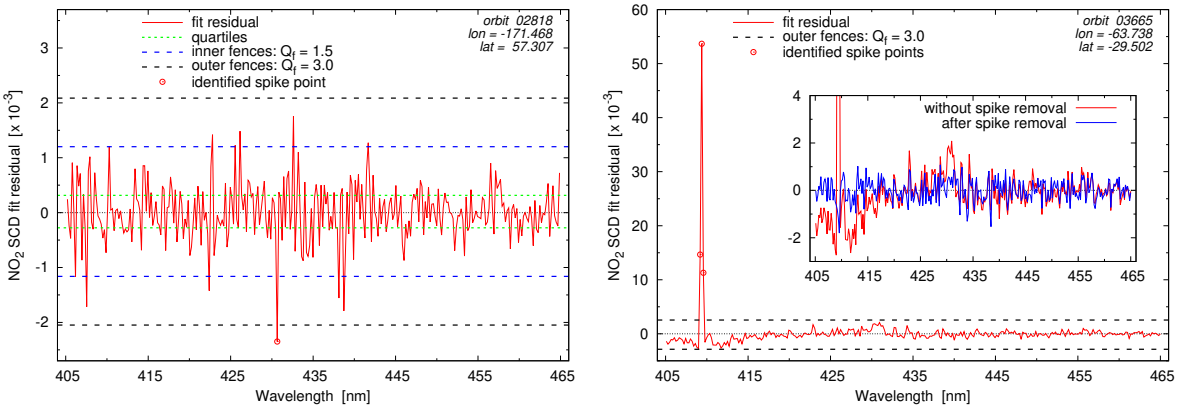

Figure 32: Examples of outliers in the TROPOMI NO_2 fit residual. *Left panel*: fit residual for a ground pixel over the northern Pacific Ocean, where the quartiles and the inner and outer fences are indicated by dashed lines. *Right panel*: fit residual for a ground pixel over Brazil, where the impact of a high-energy partical caused by the South Atlantic Anomaly created a massive spike, involving three wavelength pixels; the inset shows a zoom-in of the residual before and after spike removal. For more details see the text.

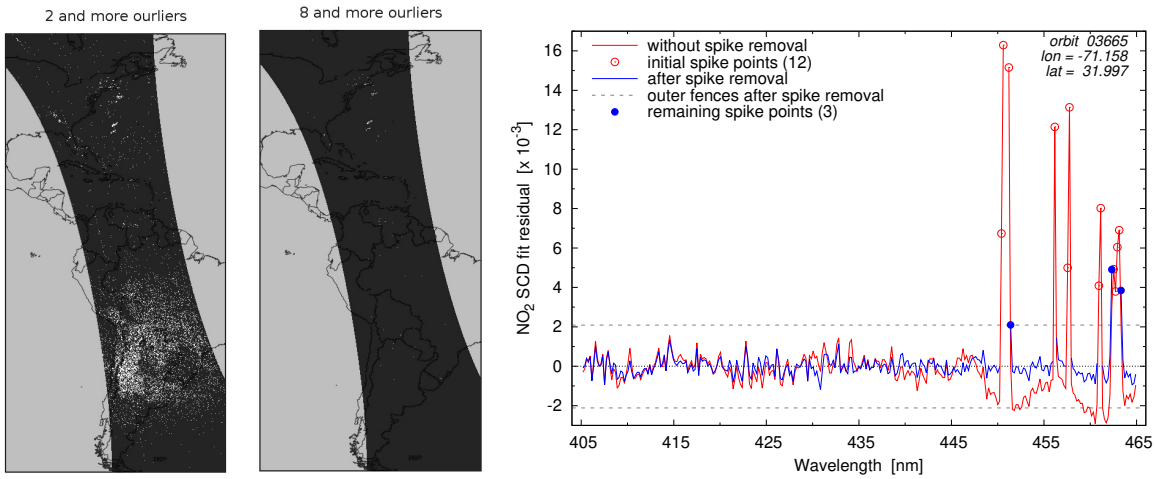

Figure 33: Examples of outliers in the TROPOMI NO_2 SCD retrieval using Level-1b version 1 data of orbit 03658 (28 June 2018) over the Americas. *Left panel*: white spots mark ground pixels with 2 or more outliers, where the South Atlantic Anomaly is clearly visible. *Middle panel*: idem, but 8 or more outliers. *Right panel*: fit residual for a fully clouded ground pixel, where two wavelength pixels are flagged as saturated and thus removed from the fit (at 450.8 and 451.0 nm), the spike removal then finds 12 outliers and after removal of these there are 3 outliers left (these are not removed, because there is no second round in the spike removal); due to the spike removal the RMS error decreases from 21.173×10^{-4} to 5.613×10^{-4}.

Most ground pixels with outliers have one or two outliers, even those over the South Atlantic Anomaly, where high-energy particle impacts on the CCD detector occur more often. Ground pixels suffering from saturation effects, however, may have a much larger number of outliers. Due to the high SNR of TROPOMI, bright scenes, notably over clouds in the tropics, the CCD may be over-exposed. As a result of this a number of wavelength pixels may get saturated and the electronic effects of this may spread to neighbouring wavelength pixels and to grond pixels in neighbouring rows, an effect called "blooming". Saturation effects occur most in the dector parts of band 4 ($400-496$ nm) and in band 6 ($720-785$ nm). In band 4 saturation is most prominent at high wavelengths but may spread far down into the NO_2 fit window.

Version 1 Level-1b data contains flags on wavelength pixels affected by saturation (such wavelength pixels are removed from the spectrum before the DOAS fit), but the criteria for this flagging are set rather conservative and there is no flagging of blooming. This left a number of wavelength pixels unflagged but affected, leading to multiple strong outliers (up to more than 50 outliers were observed in some ground pixels). Even after the spike removal, the new fit may show outliers and these fit results cannot always be trusted.

Version 2 Level-1b data has a better flagging for saturation and flagging for blooming, drastically reducing the number of outliers and spectra repaired by the spike removal give in most cases reliable results. (Flagging for saturation and blooming uses the same Level-1b error code.)

Figure 33 shows the location of ground pixels with outliers detected in an orbit over the Americas, i.e. including part of the South Atlantic Anomaly, with some high and bright cloud complexes over the eastern part of the USA and the western part of the Atlantic Ocean; one of the pixels in the latter region is used to give an example of the fit residual with and without spike removal in Fig. 33.

The treatment of saturation and outliers on wavelength pixels in the NO_2 SCD retrieval is governed by configuration parameters, listed in Table 22: the settings for NO_2-v2.2 are made for use with version-2 Level-1b

Table 22: Configuration parameters in the NO_2 processing related to saturation in the Level-1b spectra and outliers in the NO_2 retrieval residual; NO_2 data version coverages are listed in Table 2.

configuration parameter	NO_2-v1.x L1B-v1.0	NO_2-v2.2 L1B-v2.0
The maximum fraction of the radiance spectrum that is allowed to be flagged as saturated before the ground pixel is skipped	0.01	0.25
The maximum number of outliers that is allowed to be in a spectrum before the ground pixel is skipped	N/A	10

data in mind; prior NO_2 processor versions accepted very few saturation flags.

Since the outlier removal procedure is called only once, spikes may be left in the fit residual of the second DOAS round while the criteria for error flagging in Table 22 are not met in the first DOAS round, in particular in case of saturation effects over bright clouds. In most cases such a problem will lead to large SCD uncertainty estimates, which will be picked up by the limit set to this uncertainty (cf. Sect. 8.1, App. E). but not in all cases, thus leading to potentially unreliable NO_2 column values not flagged as such.

G NO_2 processor version overview before version 2.4.0

For reference sake, Table 23 gives an overview of the NO_2 processor versions before the full mission reprocessing in 2022 using version v2.4.0. The version overview as of v2.4.0 can be found in Table 2 in Sect. 5.6.

Table 23: Overview of periods of operation of the operational NO_2 processor versions in the near-real time (NRTI) and the off-line (OFFL) data streams, as well as for officially reprocessed (RPRO) data, up to the full mission reprocessing in 2022 using version 02.04.00; later versions are listed in Sect. 5.6 in Table 2 (see also the latest PRF [ER3]). Concerning NO_2, there is no difference between the different minor release versions v1.2.x, and the same holds for the versions v1.3.x. The differences between version 1.2.2 and 1.3.2 are relatively small and involve only a small fraction of the observations. Version v1.4.0 involves a major upgrade in the Level-2 cloud product FRESCO used by the NO_2 processor (viz. Sect. 6.4.4), leading to a significant increase of the tropospheric NO_2 over polluted scenes. Major release version v2.2.0 of the NO_2 processor marks the switch to v2.0.0 of the Level-1b spectral data as well as a significant change to the surface albedo treatment. Note that on 6 August 2019, as of orbit 9388, the nadir ground pixel dimensions reduced from approximately 7.0×3.5 km^2 to approximately 5.5×3.5 km^2 without a change in the processor.

Collection	Processor version	ATBD version	Data stream	In operation from		In operation until	
				orbit	date	orbit	date
01	01.00.00	1.2.0	NRTI OFFL	03745 03661	2018-07-04 2018-06-28	03946 03847	2018-07-18 2018-07-11
	01.01.00	1.2.0	NRTI OFFL	03947 03848	2018-07-18 2018-07-11	05333 05235	2018-10-24 2018-10-17
	01.02.00	1.3.0	NRTI OFFL	05336 05236	2018-10-24 2018-10-17	05929 05832	2018-12-05 2018-11-28
	01.02.02	1.3.0	NRTI OFFL RPRO	05931 05833 02818	2018-12-05 2018-11-28 2018-04-30	07518 07424 05235	2019-03-27 2019-03-20 2018-10-17
	01.03.00	1.4.0	NRTI OFFL	07519 07425	2019-03-27 2019-03-20	07999 07906	2019-04-23 2019-04-30
	01.03.01	1.4.0	NRTI OFFL	08000 07907	2019-04-30 2019-04-23	08906 08814	2019-07-03 2019-06-26
	01.03.02	1.4.0	NRTI OFFL	08906 08815	2019-07-03 2019-06-26	16256 16212	2020-12-02 2020-11-29
	01.04.00	2.2.0	NRTI OFFL	16259 16213	2020-12-02 2020-11-29	19306 19257	2021-07-05 2021-07-01
02	02.02.00	2.2.0	NRTI OFFL	19308 19258	2021-07-05 2021-07-01	21222 21187	2021-11-17 2021-11-14
	02.03.01	2.2.0	NRTI OFFL	21223 21188	2021-11-17 2021-11-14	24697 24654	2022-07-20 2022-07-17

The change from version 1.2.x to 1.3.x was a relatively minor update [ER3], affecting only a minority of pixels, and these versions have been combined in past studies. The update from version 1.3.x to 1.4.0 [Van Geffen et al., 2022] on 2 December 2020 has led to significant changes in tropospheric NO_2, in particular over scenes with low but non-zero cloud fractions (cloud radiance fractions between 0.1 and 0.5) and high pollution levels where NO_2 tropospheric columns have increased. The updates from version 1.4.0 to 2.2.0 [Van

Geffen et al., 2022] have mainly affected cloud-free scenes and lead to a further increase in tropospheric NO_2 in polluted regions. Furthermore, for snow/ice conditions and coastal areas the impact on tropospheric NO_2 may be larger. Datasets should therefore not be combined without carefully addressing these changes.

H References

[Adams et al., 2016] Adams, C., Normand, E. N., McLinden, C. A., Bourassa, A. E., Lloyd, N. D., Degenstein, D. A., Krotkov, N. A., Rivas, M. B., Boersma, K. F., and Eskes, H. (2016). Limb-nadir matching using non-coincident no2 observations: proof of concept and the omi-minus-osiris prototype product. *Atmos. Meas. Tech.*, 9:4103–4122.

[Adams et al., 2013] Adams, C., Strong, K., Zhao, X., Bourassa, A. E., Daffer, W. H., Degenstein, D., Drummond, J. R., Farahani, E. E., Fraser, A., Lloyd, N. D., Manney, G. L., McLinden, C. A., Rex, M., Roth, C., Strahan, S. E., Walker, K. A., and Wohltmann, I. (2013). The spring 2011 final stratospheric warming above Eureka: anomalous dynamics and chemistry. *Atmos. Chem. Phys.*, 13:611–624.

[Allen et al., 2021] Allen, D., Pickering, K., E., B., van Geffen, J., Lapiere, J., Koshak, W., and Eskes, H. (2021). Observations of lightning nox production from tropomi case studies over the united states. *J. Geophys. Res. Atmospheres*, 26:23 pp.

[Bak et al., 2013] Bak, J., Kim, J. H., Liu, X., Chance, K., and Kim, J. (2013). Evaluation of ozone profile and tropospheric ozone retrievals from GEMS and OMI spectra. *Atmos. Meas. Tech.*, 6:239–249.

[Barlow, 1989] Barlow, R. J. (1989). *Statistics: a guide to the use of statistical methods in the physical sciences*. John Wiley & Sons, New York.

[Beirle et al., 2011] Beirle, S., Boersma, K. F., Platt, U., Lawrence, M. G., and Wagner, T. (2011). Megacity emissions and lifetimes of nitrogen oxides probed from space. *Science*, 333:1737–1739.

[Beirle et al., 2016] Beirle, S., Hörmann, C., P., J., Liu, S., Penning de Vries, M., Pozzer, A., Sihler, H., Valks, P., and Wagner, T. (2016). The STRatospheric Estimation Algorithm from Mainz (STREAM): estimating stratospheric NO2 from nadir-viewing satellites by weighted convolution. *Atmos. Meas. Tech.*, 9:2753–2779.

[Beirle et al., 2010] Beirle, S., Kühl, S., Puķīte, J., and Wagner, T. (2010). Retrieval of tropospheric column densities of NO_2 from combined SCIAMACHY nadir/limb measurements. *Atmos. Meas. Tech.*, 3:283–299.

[Belmonte-Rivas et al., 2014] Belmonte-Rivas, M., Veefkind, P., Boersma, F., P., Eskes, H., and Gille, J. (2014). Intercomparison of daytime stratospheric NO_2 satellite retrievals and model simulations. *Atmos. Meas. Tech.*, 7:2203–2225.

[Bernath et al., 2005] Bernath, P. F., McElroy, C. T., Abrams, M. C., Boone, C. D., and M. Butler, e. a. (2005). Atmospheric Chemistry Experiment (ACE): Mission overview. *Geophys. Res. Lett.*, 32(L15S01):5 pp.

[Boersma et al., 2002] Boersma, K. F., Bucsela, E., Brinksma, E., and Gleason, J. F. (2002). NO_2. In *OMI Algorithm Theoretical Basis Document – Vol. 4: OMI Trace Gas Algorithms, ATBD-OMI-02 Vers. 2.0*, pages 13–28. NASA Goddard Space Flight Cent., Greenbelt, Md.

[Boersma et al., 2004] Boersma, K. F., Eskes, H. J., and Brinksma, E. J. (2004). Error analysis for tropospheric NO_2 retrieval from space. *J. Geophys. Res.*, 109(D04311):20 pp.

[Boersma et al., 2011] Boersma, K. F., Eskes, H. J., Dirksen, R. J., Van der A, R. J., Veefkind, J. P., Stammes, P., Huijnen, V., Kleipool, Q. L., Sneep, M., Claas, J., Leitão, J., Richter, A., Zhou, Y., and Brunner, D. (2011). An improved retrieval of tropospheric NO_2 columns from the Ozone Monitoring Instrument. *Atmos. Meas. Tech.*, 4:1905–1928.

[Boersma et al., 2018] Boersma, K. F., Eskes, H. J., Richter, A., Smedt, I. D., Lorente, A., Beirle, S., van Geffen, J. H. G. M., Zara, M., Peters, E., Roozendael, M. V., Wagner, T., Maasakkers, J. D., van der A, R. J., Nightingale, J., Rudder, A. D., Irie, H., Pinardi, G., Lambert, J.-C., and Compernolle, S. (2018). Improving algorithms and uncertainty estimates for satellite NO2 retrievals: Results from the Quality Assurance for Essential Climate Variables (QA4ECV) project Variables (QA4ECV) project. *Atmos. Meas. Tech.*, 11:6651–6678.

[Boersma et al., 2007] Boersma, K. F., Eskes, H. J., Veefkind, J. P., Brinksma, E. J., Van der A, R. J., Sneep, M., Van den Oord, G. H. J., , P. F., Stammes, P., F., G. J., and Bucsela, E. J. (2007). Near-real time retrieval of tropospheric NO_2 from OMI. *Atmos. Chem. Phys.*, 7:2013–2128.

[Boersma et al., 2009] Boersma, K. F., Jacob, D. J., Trainic, M., Rudich, Y., DeSmedt, I., Dirksen, R., and Eskes, H. J. (2009). Validation of urban NO_2 concentrations and their diurnal and seasonal variations observed from the SCIAMACHY and OMI sensors using in situ surface measurements in israeli cities. *Atmos. Chem. Phys.*, 9:3867–3879.

[Boersma et al., 2016] Boersma, K. F., Vinken, G. C. M., and Eskes, H. J. (2016). Representativeness errors in comparing chemistry transport and chemistry climate models with satellite UV-Vis tropospheric column retrievals. *Geosci. Model Dev.*, 9:875–898.

[Bovensmann et al., 1999] Bovensmann, H., Burrows, J. P., Buchwitz, M., Frerick, J., Noel, S., Rozanov, V. V., Chance, K. V., and Goede, A. P. H. (1999). SCIAMACHY: mission objectives and measurement modes. *J. Atmos. Sci.*, 56:127–150.

[Bucsela et al., 2006] Bucsela, E. J., Celarier, E. A., Wenig, M. O., Gleason, J. F., Veefkind, J. P., Boersma, K. F., and Brinksma, E. J. (2006). Algorithm for NO_2 vertical column retrieval from the ozone monitoring instrument. *IEEE Trans. Geosci. Rem. Sens.*, 44:1245–1258.

[Bucsela et al., 2013] Bucsela, E. J., Krotkov, N. A., Celarier, E. A., Lamsal, L. N., Swartz, W. H., Bhartia, P. K., Boersma, K. F., Veefkind, J. P., Gleason, J. F., and Pickering, K. E. (2013). A new stratospheric and tropospheric NO_2 retrieval algorithm for nadir-viewing satellite instruments: applications to OMI. *Atmos. Meas. Tech.*, 6:2607–2626.

[Burrows et al., 1999] Burrows, J. P., Weber, M., Buchwitz, M., Rozanov, V., Ladstätter-Weißenmayer, A., Richter, A., Debeek, R., Hoogen, R., Bramstedt, K., Eichmann, K.-U., Eisinger, M., and Perner, D. (1999). The Global Ozone Monitoring Experiment (GOME): Mission concept and first results. *J. Atmos. Sci.*, 56:151–175.

[Castellanos and Boersma, 2012] Castellanos, P. and Boersma, K. F. (2012). Reductions in nitrogen oxides over Europe driven by environmental policy and economic recession. *Scientific Reports*, 2:7 pp.

[Chance and Kurucz, 2010] Chance, K. V. and Kurucz, R. L. (2010). An improved high-resolution solar reference spectrum for earth's atmosphere measurements in the ultraviolet, visible, and near infrared. *J. Quant. Spectrosc. Radiat. Transfer*, 111:1289–1295.

[Chance and Spurr, 1997] Chance, K. V. and Spurr, R. J. D. (1997). Ring effect studies: Rayleigh scattering, including molecular parameters for rotational Raman scattering and the Fraunhofer spectrum. *Appl. Opt.*, 36(21):5224–5230.

[Chandrasekhar, 1960] Chandrasekhar, S. (1960). *Radiative Transfer*. Dover Publications, New York.

[Chu and McCormick, 1986] Chu, W. P. and McCormick, M. P. (1986). Sage observations of strastospheric nitrogen dioxide. *J. Geophys. Res.*, 91(D5):5465–5476.

[Cooper et al., 2018] Cooper, M. J., Martin, R. V., Lyapustin, A. I., and McLinden, C. A. (2018). Assessing snow extent data sets over north america to inform and improve trace gas retrievals from solar backscatter. *Atmos. Meas. Tech.*, 11:2983–2994.

[Crutzen, 1970] Crutzen, P. J. (1970). The influence of nitrogen oxides on the atmospheric ozone content. *Quart. J. R. Meteorol. Soc.*, 96:320–325.

[De Haan et al., 1987] De Haan, J. F., Bosma, P. B., and Hovenier, J. W. (1987). The adding method for multiple scattering in a non-homogeneous Rayleigh atmosphere. *Astron. & Astroph.*, 183:371–391.

[De Rosnay et al., 2015] De Rosnay, P., Isaksen, L., and Dahoui, M. (2015). Snow data assimilation at ecmwf. *ECMWF Newsletter No. 143, Spring 2015*, pages 26–31.

[De Ruyter de Wildt et al., 2012] De Ruyter de Wildt, M., Eskes, H., and Boersma, K. F. (2012). The global economic cycle and satellite-derived NO_2 trends over shipping lanes. *Geophys. Res. Lett.*, 39(L01802):6 pp.

[Dentener et al., 2006] Dentener, F., Drevet, J., Lamarque, J. F., Bey, I., Eickhout, B., Fiore, A. M., Hauglustaine, D., Horowitz, L. W., Krol, M., Kulshrestha, U. C., Lawrence, M., Galy-Lacaux, C., Rast, S., Shindell, D., Stevenson, D., Noije, T. V., Atherton, C., Bell, N., Bergman, D., Butler, T., Cofala, J., Collins, B., Doherty, R., Ellingsen, K., Galloway, J., Gauss, M., Montanaro, V., Müller, J. F., Pitari, G., Rodriguez, J., Sanderson, M., Solmon, F., Strahan, S., Schultz, M., Sudo, K., Szopa, S., and Wild, O. (2006). Nitrogen and sulfur deposition on regional and global scales: A multimodel evaluation. *Global Biogeochem. Cycles*, 20(GB4003):21 pp.

[Dentener et al., 2003] Dentener, F., Van Weele, M., Krol, M., Houweling, S., and van Velthoven, P. (2003). Trends and inter-annual variability of methane emissions derived from 1979-1993 global CTM simulations. *Atmos. Chem. Phys.*, 3:73–88.

[Desmons et al., 2019] Desmons, M., Wang, P., Stammes, P., and Tilstra, L. G. (2019). Fresco-b: a fast cloud retrieval algorithm using oxygen b-band measurements from gome-2. *Atmos. Meas. Tech.*, 12:2485–2498.

[Dirksen et al., 2011] Dirksen, R. J., Boersma, K. F., Eskes, H. J., Ionov, D. V., Bucsela, E. J., , P. F., and Kelder, H. M. (2011). Evaluation of stratospheric NO_2 retrieved from the Ozone Monitoring Instrument: Intercomparison, diurnal cycle, and trending. *J. Geophys. Res.*, 116(D08305):22 pp.

[Dobber et al., 2008] Dobber, M., Voors, R., Dirksen, R., Kleipool, Q., and Levelt, P. (2008). The high-resolution solar reference spectrum between 250 and 550 nm and its application to measurements with the Ozone Monitoring Instrument. *Solar Physics*, 249:281–291.

[Eskes and Boersma, 2003] Eskes, H. J. and Boersma, K. F. (2003). Averaging kernels for DOAS total-column satellite retrievals. *Atmos. Chem. Phys.*, 3:1285–1291.

[Eskes et al., 2003] Eskes, H. J., Van Velthoven, P. F. J., Valks, P., and Kelder, H. M. (2003). Assimilation of GOME total ozone satellite observations in a three-dimensional tracer transport model. *Q. J. R. Meteorol. Soc.*, 129(590):1663–1681.

[Fuglestvedt et al., 1999] Fuglestvedt, J. S., Berntsen, T., Isaksen, I. S. A., Mao, H., Liang, X.-Z., and Wang, W.-C. (1999). Climatic forcing of nitrogen oxides through changes in tropospheric ozone and methane. *Atmos. Environ.*, 33(3):961–977.

[Georgoulias et al., 2020] Georgoulias, A. K., Boersma, K. F., van Vliet, J., Zhang, X., van der A, R. J., Zanis, P., and de Laat, J. (2020). "Detection of NO2 pollution plumes from individual ships with the TROPOMI/S5P satellite sensor. *Environmental Research Letters*, 15:124037, 11 pp.

[Gkatzelis et al., 2021] Gkatzelis, G. I., Gilman, J. B., Brown, S. S., Eskes, H., Gomes, A. R., Lange, A. C., McDonald, B. C., Peisch, J., Petzold, A., Thompson, C. R., and Kiendler-Scharr, A. (2021). The global impacts of COVID-19 lockdowns on urban air quality: A critical review and recommendations. *Elementa: Science of the Anthropocene*, in press.

[Gordley et al., 1996] Gordley, L. L., III, J. M. R., Mickley, L. J., Frederick, J. E., Park, J. H., Stone, K. A., Beaver, G. M., McInerney, J. M., Deaver, L. E., Toon, G. C., Murcray, F. J., Blatherwick, R. D., Gunson, M. R., Abbatt, J. P. D., III, R. L. M., Mount, G. H., Sen, B., and Blavier, J.-F. (1996). Validation of nitric oxide and nitrogen dioxide measurements made by the Halogen Occultation Experiment for UARS platform. *J. Geophys. Res.*, 101(D6):10241–10266.

[Gorshelev et al., 2014] Gorshelev, V., Serdyuchenko, A., Weber, M., and Burrows, J. P. (2014). High spectral resolution ozone absorption cross-sections: Part I. Measurements, data analysis and comparison around 293K. *Atmos. Meas. Tech.*, 7:609–624.

[Griffin et al., 2019] Griffin, D., Zhao, X., McLinden, C. A., Boersma, F., Bourassa, A., Dammers, E., Degenstein, D., Eskes, H., Fehr, L., Fioletov, V., Hayden, K., Kharol, S. K. Li, S.-M., Makar, P., Martin, R. V., Mihele, C., Mittermeier, R. L., Krotkov, N., Sneep, M., Lamsal, L. N., ter Linden, M., van Geffen, J., Veefkind, P., and Wolde, M. (2019). High resolution mapping of nitrogen dioxide with TROPOMI: First results and validation over the Canadian oil sands. *Geophys. Res. Lett.*, 46:1049–1060.

[Grooß and Russel, 2005] Grooß, J.-U. and Russel, J. M. (2005). Technical note: A stratospheric climatology for O3, H2O, CH4, NOx, HCl and HF derived from HALOE measurements. *Atmos. Chem. Phys.*, 5:2797–2807.

[Gruzdev and Elokhov, 2009] Gruzdev, A. N. and Elokhov, A. S. (2009). Validating NO_2 measurements in the vertical atmospheric column with the OMI instrument aboard the EOS Aura satellite against ground-based measurements at the Zvenigorod Scientific Station. *Izv. Atmos. Oceanic Phys.*, 45(4):444–455.

[Hains et al., 2010] Hains, J. C., Boersma, K. F., Kroon, M., Dirksen, R. J., Cohen, R. C., Perring, A. E., Bucsela, E., Volten, H., Swart, D. P. J., Richter, A. andWittrock, F., Schoenhardt, A., Wagner, T., Ibrahim, O. W., Roozendael, V., M., Pinardi, G., Gleason, J. F., Veefkind, J. P., and , P. (2010). Testing and improving OMI DOMINO tropospheric NO_2 using observations from the DANDELIONS and INTEX-B validation campaigns. *J. Geophys. Res.*, 115(D05301):20 pp.

[Hendrick et al., 2012] Hendrick, F., Mahieu, E., Bodeker, G. E., Boersma, K. F., Chipperfield, M. P., De Mazière, M., De Smedt, I., Demoulin, P., Fayt, C., Hermans, C., Kreher, K., Lejeune, B., Pinardi, G., Servais, C., Stübi, R., Van der A, R., Vernier, J.-P., and Van Roozendael, M. (2012). Analysis of stratospheric NO_2 trends above Jungfraujoch using ground-based UV-visible, FTIR, and satellite nadir observations. *Atmos. Chem. Phys.*, 12:8851–8864.

[Hilboll et al., 2013a] Hilboll, A., Richter, A., and Burrows, J. P. (2013a). Long-term changes of tropospheric NO_2 over megacities derived from multiple satellite instruments. *Atmos. Chem. Phys.*, 13:4145–4169.

[Hilboll et al., 2013b] Hilboll, A., Richter, A., Rozanov, A., Hodnebrog, O., Heckel, A., Solberg, S., Stordal, F., and Burrows, J. P. (2013b). Improvements to the retrieval of tropospheric NO_2 from satellite – stratospheric correction using SCIAMACHY limb/nadir matching and comparison to Oslo CTM2 simulations. *Atmos. Meas. Tech.*, 6:565–584.

[Huijnen et al., 2010a] Huijnen, V., Eskes, H. J., Poupkou, A., Elbern, H., Boersma, K. F., Foret, G., Sofiev, M., Valdebenito, A., Flemming, J., Stein, O., Gross, A., Robertson, L., D'Isidoro, M., Kioutsioukis, I., Friese, E., Amstrup, B., Bergstrom, R., Strunk, A., Vira, J., Zyryanov, D., Maurizi, A., Melas, D., Peuch, V.-H., and Zerefos, C. (2010a). Comparison of OMI NO_2 tropospheric columns with an ensemble of global and European regional air quality models. *Atmos. Chem. Phys.*, 10:3273–3296.

[Huijnen et al., 2010b] Huijnen, V., Williams, J., Van Weele, M., Van Noije, T., Krol, M., Dentener, F., Segers, A., Houweling, S., Peters, W., De Laat, J., Boersma, F., Bergamaschi, P., Van Velthoven, P., Le Sager, P., Eskes, H., Alkemade, F., Scheele, R., Nédélec, P., and Pätz, H.-W. (2010b). The global chemistry transport model tm5: description and evaluation of the tropospheric chemistry version 3.0. *Geosc. Model Dev.*, 3(2):445–473.

[Ialongo et al., 2020] Ialongo, I., Virta, H., Eskes, H., Hovila, J., and Douros, J. (2020). Comparison of tropomi/sentinel-5 precursor no2 observations with ground-based measurements in helsinki. *Atmos. Meas. Tech.*, 13:205–218.

[Ingmann et al., 2012] Ingmann, P., Veihelmann, B., Langen, J., Lamarre, D., Stark, H., and Courrèges-Lacoste, G. B. (2012). Requirements for the GMES Atmosphere Service and ESA's implementation concept: Sentinels-4/-5 and -5p. *Rem. Sens. Environment*, 120:58–69.

[Irie et al., 2012] Irie, H., Boersma, K. F., Kanaya, Y., Takashima, H., Pan, X., and Wang, Z. F. (2012). First quantitative bias estimates for tropospheric NO_2 columns retrieved from SCIAMACHY, OMI, and GOME-2 using a common standard. *Atmos. Meas. Tech.*, 5:2403–2411.

[Jacob, 1999] Jacob, D. J. (1999). *Introduction to Atmospheric Chemistry*. Princeton University Press.

[Judd et al., 2020] Judd, L. M., Al-Saadi, J. A., Szykman, J. J., Valin, L. C., Janz, S. J., Kowalewski, M. G., Eskes, H. J., Veefkind, J. P., Cede, A., Mueller, M., Gebetsberger, M., Swap, R., Pierce, R. B., Nowlan, C. R., Abad, G. G., Nehrir, A., and Williams, D. (2020). Evaluating sentinel-5p tropomi tropospheric no2 column densities with airborne and pandora spectrometers near new york city and long island sound. *Atmos. Meas. Tech.*, 13:6113–6140.

[Kim et al., 2020] Kim, J., Jeong, U., Ahn, H.-H., Kim, J. H., Park, R. J., and et al., H. L. (2020). New era of air quality monitoring from space: Geostationary Environment Monitoring Spectrometer (GEMS). *Bulletin of the American Meteorological Society*, 101:22 pp.

[Kleipool et al., 2018] Kleipool, Q., Ludewig, A., L., B., Bartstra, R., Braak, R., Dierssen, W., Dewitte, P.-J., Kenter, P., Landzaat, R., Leloux, J., Loots, E., Meijering, P., van der Plas, E., Rozemeijer, N., Schepers, D., Schiavini, D., Smeets, J., Vacanti, G., Vonk, F., and Veefkind, J. P. (2018). Pre-launch calibration results of the TROPOMI payload on-board the Sentinel-5 Precursor satellite. *Atmos. Meas. Tech.*, 11:6439–6479.

[Kleipool et al., 2008] Kleipool, Q. L., Dobber, M. R., De Haan, J. F., and , P. F. (2008). Earth surface reflectance climatology from 3 years of OMI data. *J. Geophys. Res.*, 113(D18308):22 pp.

[Kong et al., 2023] Kong, H., Lin, J., Zhang, Y., Li, C., Xu, C., Shen, L., Liu, X., Yang, K., Su, H., and Xu, W. (2023). High natural nitric oxide emissions from lakes on tibetan plateau under rapid warming. *Nat. Geosci.*, 16:474–477.

[Labzovskii et al., 2024] Labzovskii, L., van Geffen, J., Liu, M., van der A, R., de Laat, J., Leune, B., Eskes, H., Lin, X., Ding, J., and Richter, A. (2024). No2 satellite retrievals biased by absorption in water. *Nat. Geosci.*, 17:972–975.

[Lampel et al., 2015] Lampel, J., Frieß, U., and U., P. (2015). The impact of vibrational raman scattering of air on doas measurements of atmospheric trace gases. *Atmos. Meas. Tech.*, 8:3767–3787.

[Lamsal et al., 2021] Lamsal, L. N., Krotkov, N. A., Vasilkov, A., Marchenko, S., Qin, W., Yang, E.-S., Fasnacht, Z., Joiner, J., Choi, S., Haffner, D., Swartz, W. H., Fisher, B., and Bucsela, E. (2021). Ozone monitoring instrument (omi) aura nitrogen dioxide standard product version 4.0 with improved surface and cloud treatments. *Atmos. Meas. Tech.*, 14:455–479.

[Lamsal et al., 2010] Lamsal, L. N., Martin, R. V., Van Donkelaar, A., Celarier, E. A., Bucsela, E. J., Boersma, K. F., Dirksen, R., Luo, C., and Wang, Y. (2010). Indirect validation of tropospheric nitrogen dioxide retrieved from the OMI satellite instrument: Insight into the seasonal variation of nitrogen oxides at northern midlatitudes. *J. Geophys. Res.*, 115(D05302):15 pp.

[Laughner et al., 2019] Laughner, J. L., Zhu, Q., and Cohen, R. C. (2019). Evaluation of version 3.0B of the BEHR OMI NO2 product. *Atmos. Meas. Tech.*, 12:129–146.

[Leitão et al., 2010] Leitão, J., Richter, A., Vrekoussis, M., Kokhanovsky, A., Zhang, Q., Beekmann, M., and Burrows, J. P. (2010). On the improvement of NO_2 satellite retrievals – aerosol impact on the airmass factors. *Atmos. Meas. Tech.*, 3:475–493.

[Lerot et al., 2010] Lerot, C., Stavrakou, T., De Smedt, I., Müller, J.-F., and Van Roozendael, M. (2010). Glyoxal vertical columns from GOME-2 backscattered light measurements and comparisons with a global model. *Atmos. Chem. Phys.*, 10:12059–12072.

[Leue et al., 2001] Leue, C., Wenig, M., Wagner, T., Klimm, O., Platt, U., and Jähne, B. (2001). Quantitative analysis of NO_x emissions from Global Ozone Monitoring Experiment satellite image sequences. *J. Geophys. Res.*, 106(D6):5493–5505.

[Levelt et al., 2006] Levelt, P. F., van den Oord, G. H. J., Dobber, M. R., Mälkki, A., Visser, H., de Vries, J., Stammes, P., Lundell, J. O. V., and Saari, H. (2006). The Ozone Monitoring Instrument. *IEEE Trans. Geosci. Rem. Sens.*, 44:1093–1101.

[Liley et al., 2000] Liley, J. B., Johnston, P. V., McKenzie, R. L., Thomas, A. J., and Boyd, I. S. (2000). Stratospheric NO_2 variations from a long time series at Lauder, New Zealand. *J. Geophys. Res.*, 105(D9):11,633–11,640.

[Lin et al., 2014] Lin, J., Martin, R. V., Boersma, K. F., Sneep, M., Stammes, P., Spurr, R., Wang, P., Roozendael, M. V., Clémer, K., and Irie, H. (2014). Retrieving tropospheric nitrogen dioxide over China from the Ozone Monitoring Instrument: Effects of aerosols, surface reflectance anisotropy and vertical profile of nitrogen dioxide. *Atmos. Chem. Phys.*, 14:1441–1461.

[Lin et al., 2010] Lin, J.-T., McElroy, M. B., and Boersma, K. F. (2010). Constraint of anthropogenic NO_x emissions in china from different sectors: a new methodology using multiple satellite retrievals. *Atmos. Chem. Phys.*, 10:63–78.

[Liu et al., 2020] Liu, M., Lin, J., Kong, H., Boersma, K. F., Eskes, H., Kanaya, Y., He, Q., Tian, X., Qin, K., Xie, P., Spurr, R., Ni, R., Yan, Y., Weng, H., and Wang, J. (2020). A new TROPOMI product for tropospheric NO2 columns over East Asia with explicit aerosol corrections. *Atmos. Meas. Tech.*, 13:4247–4259.

[Liu et al., 2019] Liu, S., Valks, P., Pinardi, G., De Smedt, I., Yu, H., Beirle, S., and Richter, A. (2019). An Improved Total and Tropospheric NO2 Column Retrieval for GOME-2. *Atmos. Meas. Tech.*, 12:1029–1057.

[Llewellyn et al., 2004] Llewellyn, E. J., Lloyd, N. D., Degenstein, D. A., Gattinger, R. L., and S. V. Petelina, e. a. (2004). The OSIRIS instrument on the Odin spacecraft. *Canadian Journal of Physics*, 82(6):411–422.

[Lorente et al., 2017] Lorente, A., Folkert Boersma, K., Yu, H., Dörner, S., Hilboll, A., Richter, A., Liu, M., Lamsal, L. N., Barkley, M., De Smedt, I., Van Roozendael, M., Wang, Y., Wagner, T., Beirle, S., Lin, J.-T., Krotkov, N., Stammes, P., Wang, P., Eskes, H. J., and Krol, M. (2017). Structural uncertainty in air mass factor calculation for NO2 and HCHO satellite retrievals. *Atmos. Meas. Tech.*, 10:759–782.

[Loyola et al., 2020] Loyola, D. G., Xu, J., Heue, K.-P., and Zimmer, W. (2020). Applying fp_ilm to the retrieval of geometry-dependent effective lambertian equivalent reflectivity (ge_ler) daily maps from uvn satellite measurements. *Atmos. Meas. Tech.*, 13:985–999.

[Ludewig et al., 2020] Ludewig, A., Kleipool, Q., Bartstra, R., Landzaat, R., Leloux, J., Loots, E., Meijering, P., van der Plas, E., Rozemeijer, N., Vonk, F., and Veefkind, J. P. (2020). In-flight calibration results of the TROPOMI payload on-board the Sentinel-5 Precursor satellite. *Atmos. Meas. Techn.*, 13:3561–3580.

[Ma et al., 2013] Ma, J. Z., Beirle, S., Jin, J. L., Shaiganfar, R., Yan, P., and Wagner, T. (2013). Tropospheric NO_2 vertical column densities over Beijing: results of the first three years of ground-based MAX-DOAS measurements (2008-2011) and satellite validation. *Atmos. Chem. Phys.*, 13:1547–1567.

[Maasakkers et al., 2013] Maasakkers, J. D., Boersma, K. F., Williams, J. E., Van Geffen, J., Vinken, G. C. M., Sneep, M., Hendrick, F., Van Roozendael, M., and Veefkind, J. P. (2013). Vital improvements to the retrieval of tropospheric NO_2 columns from the Ozone Monitoring Instrument. *Geophys. Res. Abstracts*, 15(EGU2013-714):1. EGU General Assembly 2013.

[Marécal et al., 2015] Marécal, V., Peuch, V.-H., Andersson, C., Andersson, S., Arteta, J., Beekmann, M., Benedictow, A., Bergström, R., Bessagnet, B., Cansado, A., Chéroux, F., Colette, A., Coman, A., Curier, R. L., Denier van der Gon, H. A. C., Drouin, A., Elbern, H., Emili, E., Engelen, R. J., Eskes, H. J., Foret, G., Friese, E., Gauss, M., Giannaros, C., Guth, J., Joly, M., Jaumouillé, E., Josse, B., Kadygrov, N., Kaiser, J. W., Krajsek, K., Kuenen, J., Kumar, U., Liora, N., Lopez, E., Malherbe, L., Martinez, I., Melas, D., Meleux, F., Menut, L., Moinat, P., Morales, T., Parmentier, J., Piacentini, A., Plu, M., Poupkou, A., Queguiner, S., Robertson, L., Rouïl, L., Schaap, M., Segers, A., Sofiev, M., Tarasson, L., Thomas, M., Timmermans, R., Valdebenito, A., van Velthoven, P., van Versendaal, R., Vira, J., and Ung, A. (2015). A regional air quality forecasting system over Europe: the MACC-II daily ensemble production. *Geosci. Model Dev.*, 8:2777–2813.

[Martin et al., 2002] Martin, R. V., Chance, K., Jacob, D. J., Kurosu, T. P., Spurr, R. J. D., Bucsela, E., Gleason, J. F., Palmer, P. I., Bey, I., Fiore, A. M., Li, Q., Yantosca, R. M., and Koelemeijer, R. B. A. (2002). An improved retrieval of tropospheric nitrogen dioxide from gome. *J. Geophys. Res.*, 107(D20):4437–4457.

[Merlaud et al., 2012] Merlaud, A., Van Roozendael, M., Van Gent, J., Fayt, C., Maes, J., Toledo-Fuentes, X., Ronveaux, O., and De Maziére, M. (2012). DOAS measurements of NO_2 from an ultralight aircraft during the Earth Challenge expedition. *Atmos. Meas. Tech.*, 5:2057–2068.

[Mijling and Van der A, 2012] Mijling, B. and Van der A, R. J. (2012). Using daily satellite observations to estimate emissions of short-lived air pollutants on a mesoscopic scale. *J. Geophys. Res.*, 117(D17302):20 pp.

[Mount et al., 1984] Mount, G. H., Rusch, D. W., Noxon, J. F., Zawodny, J. M., and Barth, C. A. (1984). Measurements of stratospheric NO_2 from the Solar Mesosphere Explorer Satellite: 1. An overview of the results. *J. Geophys. Res.*, 89(D1):1327–1340.

[Munro et al., 2006] Munro, R., Eisinger, M., Anderson, C., Callies, J., Corpaccioli, E., Lang, R., Lefebvre, A., Livschitz, Y., and Albinana, A. P. (2006). GOME-2 on MetOp. In *Proceedings of the Atmospheric Science Conference 2006*, SP 628. ESA, ESA, Paris.

[Murphy et al., 1993] Murphy, D. M., Fahey, D. W., Proffitt, M. H., Liu, S. C., Chan, K. R., Eubank, C. S., Kawa, S. R., and Kelly, K. K. (1993). Reactive nitrogen and its correlation with ozone in the lower stratosphere and upper troposphere. *J. Geophys. Res.*, 98(D5):8751–8773.

[Nowlan et al., 2016] Nowlan, C. R., Liu, X., Leitch, J. W., Chance, K., González Abad, G., Liu, C., Zoogman, P., Cole, J., Delker, T., Good, W., Murcray, F., Ruppert, L., Soo, D., Follette-Cook, M. B., Janz, S. J., Kowalewski, M. G., Loughner, C. P., Pickering, K. E., Herman, J. R., Beaver, M. R., Long, R. W., Szykman, J. J., Judd, L. M., Kelley, P., Luke, W. T., Ren, X., and Al-Saadi, J. A. (2016). Nitrogen dioxide observations from the Geostationary Trace gas and Aerosol Sensor Optimization (GeoTASO) airborne instrument: Retrieval algorithm and measurements during DISCOVER-AQ Texas 2013. *Atmos. Meas. Tech.*, 9:2647–2668.

[Ott et al., 2010] Ott, L. E., Pickering, K. E., Stenchikov, G. L., Allen, D. J., DeCaria, A. J., Ridley, B., Lin, R.-F., Lang, S., and Tao, W.-K. (2010). Production of lightning NO and its vertical distribution calculated from three-dimensional cloud-scale chemical transport model simulations. *J. Geophys. Res.*, 115(D04301):19 pp.

[Palmer et al., 2001] Palmer, P. I., Jacob, D., Chance, K., Martin, R. V., Spurr, R. J. D., Kurosu, T. P., Bey, I., Yantosca, R., Fiore, A., and Li, Q. (2001). Air-mass factor formulation for spectroscopic measurements from satellite: applications to fomaldehyde retrievals from the Global Ozone Monitoring Experiment. *J. Geophys. Res.*, 106:14539–14550.

[Platt, 1994] Platt, U. (1994). Differential Optical Absorption Spectroscopy (DOAS). *Air monitoring by spectroscopic techniques, Chem. Anal.*, 127:27–76. edited by M.W. Sigrist.

[Platt and Stutz, 2008] Platt, U. and Stutz, Z. (2008). *Differential Optical Absorption Spectroscopy, Principles and Applications*. Springer, Heidelberg, Germany.

[Pope and Fry, 1997] Pope, R. M. and Fry, E. S. (1997). Absorption spectrum (380-700 nm) of pure water. II. Integrating cavity measurements. *Appl. Opt.*, 36(33):8710–8723.

[Randall et al., 1998] Randall, C. E., Rusch, D. W., Bevilacqua, R. M., Hoppel, K. W., and Lumpe, J. D. (1998). Polar Ozone and Aerosol Measurement (POAM) II stratospheric NO_2 1993-1996. *J. Geophys. Res.*, 103(D21):28361–28371.

[Ravishankara et al., 2009] Ravishankara, A. R., Daniel, J. S., and Portmann, R. W. (2009). Nitrous Oxide (N2O): The Dominant Ozone-Depleting Substance Emitted in the 21st Century. *Science*, 326(5949):123–125.

[Richter et al., 2011] Richter, A., Begoin, M., Hilboll, A., and Burrows, J. P. (2011). An improved NO_2 retrieval for the GOME-2 satellite instrument. *Atmos. Meas. Tech.*, 4:1147–1159.

[Richter and Burrows, 2002] Richter, A. and Burrows, J. P. (2002). Tropospheric NO_2 from GOME measurements. *Adv. Space Res.*, 29(11):1673–1683.

[Rodgers, 2000] Rodgers, C. D. (2000). *Inverse Methods for Atmospheric Sounding: Theory and Practice*. World Scientific Publishing.

[Schaub et al., 2007] Schaub, D., Brunner, D., Boersma, K. F., Keller, J., Folini, D., Buchmann, B., Berresheim, H., and Staehelin, J. (2007). SCIAMACHY tropospheric NO_2 over Switzerland: estimates of NO_x lifetimes and impact of the complex Alpine topography on the retrieval. *Atmos. Chem. Phys.*, 7:5971–5987.

[Seinfeld and Pandis, 2006] Seinfeld, J. H. and Pandis, S. N. (2006). *Atmospheric Chemistry and Physics - From Air Pollution to Climate Change (2nd Edition)*. John Wiley & Sons, New York.

[Serdyuchenko et al., 2014] Serdyuchenko, A., Gorshelev, V., Weber, M., Chehade, W., and Burrows, J. P. (2014). High spectral resolution ozone absorption cross-sections: Part II. Temperature dependence. *Atmos. Meas. Tech.*, 7:625–636.

[Shindell et al., 2009] Shindell, D. T., Faluvegi, G., Koch, D. M., Schmidt, G. A., Unger, N., and Bauer, S. E. (2009). Improved attribution of climate forcing to emissions. *Science*, 326(5953):716–718.

[Sierk et al., 2006] Sierk, B., Richter, A., Rozanov, A., Von Savigny, C., Schmoltner, A. M., Buchwitz, M., Bovensmann, H., and Burrows, J. P. (2006). Retrieval and monitoring of atmospheric trace gas concentrations in nadir and limb geometry using the space-borne SCIAMACHY instrument. *Environmental Monitoring and Assessment*, 120:65–73.

[Sillman et al., 1990] Sillman, S., Logan, J. A., and Wofsy, S. C. (1990). The sensitivity of ozone to nitrogen oxides and hydrocarbons in regional ozone episodes. *J. Geophys. Res.*, 95(D2):1837–1851.

[Silver et al., 2013] Silver, J. D., Brandt, J., Hvidberg, M., Frydendall, J., and Christensen, J. H. (2013). Assimilation of OMI NO_2 retrievals into the limited-area chemistry-transport model DEHM (V2009.0) with a 3-D OI algorithm. *Geosc. Model Dev.*, 6:1–16.

[Solomon, 1999] Solomon, S. (1999). Stratospheric ozone depletion: A review of concepts and history. *Rev. Geophys.*, 37(3):275–316.

[Stammes, 2001] Stammes, P. (2001). Spectral radiance modeling in the UV-visible range. In Smith, W. and Timofeyev, Y., editors, *IRS 2000: Current Problems in Atmospheric Radiation*, pages 385–388. A. Deepak, Hampton, Va.

[Stavrakou et al., 2008] Stavrakou, T., Müller, J.-F., Boersma, K. F., De Smedt, I., and Van der A, R. J. (2008). Assessing the distribution and growth rates of NO_2 emission sources by inverting a 10-year record of NO_2 satellite columns. *Geophys. Res. Lett.*, 35(L10801):5 pp.

[Tack et al., 2021] Tack, F., Merlaud, A., Iordache, M.-D., Pinardi, G., Dimitropoulou, E., Eskes, H., Bomans, B., Veefkind, P., and Van Roozendael, M. (2021). Assessment of the tropomi tropospheric no2 product based on airborne apex observations. *Atmos. Meas. Tech.*, 14:615–646.

[Thalman and Volkamer, 2013] Thalman, R. and Volkamer, R. (2013). Temperature dependant absorption cross-sections of O2-O2 collision pairs between 340 and 630 nm at atmospherically relevant pressure. *Phys. Chem. Chem. Phys.*, 15:15371–15381.

[Tilstra et al., 2024] Tilstra, L. G., de Graaf, M., Trees, V. J. H., Litvinov, P., Dubovik, O., and Stammes, P. (2024). A directional surface reflectance climatology determined from TROPOMI observations. *Atmos. Meas. Tech.*, 17:2235–2256.

[Tilstra et al., 2017] Tilstra, L. G., Tuinder, O. N. E., Wang, P., and Stammes, P. (2017). Surface reflectivity climatologies from UV to NIR determined from Earth observations by GOME-2 and SCIAMACHY. *J. Geophys. Res.*, 122:4084–4111.

[Tilstra et al., 2021] Tilstra, L. G., Tuinder, O. N. E., Wang, P., and Stammes, P. (2021). Directionally dependent Lambertian-equivalent reflectivity (DLER) of the Earth's surface measured by the GOME-2 satellite instruments. *Atmos. Meas. Tech.*, 14:4219–4238.

[Valks et al., 2011] Valks, P., Pinardi, G., Richter, A., Lambert, J.-C., Hao, N., Loyola, D., Van Roozendael, M., and Emmadi, S. (2011). Operational total and tropospheric NO_2 column retrieval for GOME-2. *Atmos. Meas. Tech.*, 4:1491–1514.

[Van der A et al., 2015] Van der A, R. J., Allaart, M. A. F., and Eskes, H. J. (2015). Extended and refined multi sensor reanalysis of total ozone for the period 1970-2012. *Atmos. Meas. Tech.*, 8:3021–3035.

[Van der A et al., 2008] Van der A, R. J., Eskes, H. J., Boersma, K. F., Van Noije, T. P. C., Van Roozendael, M., De Smedt, I., Peters, D. H. M. U., Kuenen, J. J. P., and Meijer, E. W. (2008). Trends, seasonal variability and dominant NO_x source derived from a ten year record of NO_2 measurd from space. *J. Geophys. Res.*, 113(D04302):12 pp.

[Van Diedenhoven et al., 2007] Van Diedenhoven, B., Hasekamp, O. P., and Landgraf, J. (2007). Retrieval of cloud parameters from satellite-based reflectance measurements in the ultraviolet and the oxygen A-band. *J. Geophys. Res.*, 112(D15208):15 pp.

[Van Geffen et al., 2020] Van Geffen, J. H. G. M., Boersma, K. F., Eskes, H., Sneep, M., ter Linden, M., Zara, M., and Veefkind, J. P. (2020). S5P/TROPOMI NO_2 slant column retrieval: method, stability, uncertainties, and comparisons with OMI. *Atmos. Meas. Tech.*, 13:1315–1335.

[Van Geffen et al., 2015] Van Geffen, J. H. G. M., Boersma, K. F., Van Roozendael, M., Hendrick, F., Mahieu, E., De Smedt, I., M., S., and Veefkind, J. P. (2015). Improved spectral fitting of nitrogen dioxide from OMI in the 405 – 465 nm window. *Atmos. Meas. Tech.*, 8:1685–1699.

[Van Geffen et al., 2022] Van Geffen, J. H. G. M., Eskes, H., Compernolle, S., Pinardi, G., Verhoelst, T., Sneep, M., ter Linden, M., Ludewig, A., Boersma, K. F., and Veefkind, J. P. (2022). Sentinel-5P TROPOMI NO_2 retrieval: impact of version v2.2 improvements and comparisons with OMI and ground-based data. *Atmos. Meas. Tech.*, 15:2037–2060.

[Van Geffen et al., 2026] Van Geffen, J. H. G. M., Eskes, H., Sneep, M., ter Linden, M., and Veefkind, J. P. (2026). Removing trouble around 430 nm in TROPOMI and OMI NO_2 retrievals – *title TBD*. *Atmos. Meas. Tech.*, in preparation.

[Van Roozendael et al., 2006] Van Roozendael, M., Loyola, D., Spurr, R., Balis, D., Lambert, J.-C., Livschitz, Y., Valks, P., Ruppert, T., Kenter, P., Fayt, C., and Zehner, C. (2006). Ten years of GOME/ERS-2 total ozone data – The new GOME data processor (GDP) version 4: 1. Algorithm description. *J. Geophys. Res.*, 111(D14311):21 pp.

[Vandaele et al., 1998] Vandaele, A. C., Hermans, C., Simon, P. C., Carleer, M., Colin, R., Fally, S., Mérienne, M. F., Jenouvrier, A., and Coquart, B. (1998). Measurements of the NO_2 absorption cross-section from 42000 cm^{-1} to 10000 cm^{-1} (238-1000 nm) at 220 K and 294 K. *J. Quant. Spectrosc. & Radiat. Transfer*, 59:171–184.

[Vandevender and Haskell, 1982] Vandevender, W. H. and Haskell, K. H. (1982). The SLATEC mathematical subroutine library. *ACM SIGNUM Newsletter*, 17.3:16–21.

[Vasilkov et al., 2017] Vasilkov, A., Qin, W., Krotkov, N., Lamsal, L., Spurr, R., Haffner, D., Joiner, J., Yang, E.-S., and Marchenko, S. (2017). Accounting for the effects of surface BRDF on satellite cloud and trace-gas retrievals: a new approach based on geometry-dependent Lambertian equivalent reflectivity applied to OMI algorithms. *Atmos. Meas. Tech.*, 10:333–349.

[Vasilkov et al., 2002] Vasilkov, A. P., Joiner, J., Gleason, J., and Bhartia, P. K. (2002). Ocean Raman scattering in satellite backscatter UV measurements. *Geophys. Res. L*, 29(17):1837–1840.

[Veefkind et al., 2012] Veefkind, J. P., Aben, I., McMullan, K., Förster, H., De Vries, J., Otter, G., Claas, J., Eskes, H. J., De Haan, J. F., Kleipool, Q., Van Weele, M., Hasekamp, O., Hoogeveen, R., Landgraf, J., Snel, R., Tol, P., Ingmann, P., Voors, R., Kruizinga, B., Vink, R., Visser, H., and , P. F. (2012). TROPOMI on the ESA Sentinel-5 Precursor: A GMES mission for global observations of the atmospheric composition for climate, air quality and ozone layer applications. *Rem. Sens. Environment*, 120:70–83.

[Veefkind et al., 2016] Veefkind, J. P., De Haan, J. F., Sneep, M., and , P. (2016). Improvements of the OMI O2-O2 operational cloud algorithm and comparisons with ground-based radar-lidar observations. *Atmos. Meas. Techn.*, 9:6035–6049.

[Verhoelst et al., 2021] Verhoelst, T., Compernolle, S., Pinardi, G., Lambert, J.-C., Eskes, H. J., Eichmann, K.-U., Fjæraa, A. M., Granville, J., Niemeijer, S., Cede, A., Tiefengraber, M., Hendrick, F., Pazmiño, A., Bais, A., Bazureau, A., Boersma, K. F., Bognar, K., Dehn, A., Donner, S., Elokhov, A., Gebetsberger, M., Goutail, F., Grutter de la Mora, M., Gruzdev, A., Gratsea, M., Hansen, G. H., Irie, H., Jepsen, N., Kanaya, Y., Karagkiozidis, D., Kivi, R., Kreher, K., , P. F., Liu, C., Müller, M., Navarro Comas, M., Piters, A. J. M., Pommereau, J.-P., Portafaix, T., Prados-Roman, C., Puentedura, O., Querel, R., Remmers, J., Richter, A., Rimmer, J., Rivera Cárdenas, C., Saavedra de Miguel, L., Sinyakov, V. P., Stremme, W., Strong, K., Van Roozendael, M., Veefkind, J. P., Wagner, T., Wittrock, F., Yela González, M., and Zehner, C. (2021). Ground-based validation of the copernicus sentinel-5p tropomi no2 measurements with the ndacc zsl-doas, max-doas and pandonia global networks. *Atmos. Meas. Tech.*, 14:481–510.

[Vermote and Tanré, 1992] Vermote, E. and Tanré, D. (1992). Analytic expressions for radiative properties of planar Rayleigh scattering media, including polarization contributions. *J. Quant. Spectrosc. & Radiat. Transfer*, 47:305–314.

[Vountas et al., 2003] Vountas, M., Richter, A., Wittrock, F., and Burrows, J. P. (2003). Inelastic scattering in ocean water and its impact on trace gas retrievals from satellite data. *Atmos. Chem. Phys.*, 3:1365–1375.

[Wang et al., 2008] Wang, P., Stammes, P., Van der A, R., Pinardi, G., and Van Roozendael, M. (2008). FRESCO+: an improved O_2 A-band cloud retrieval algorithm for tropospheric trace gas retrievals. *Atmos. Chem. Phys.*, 8:6565–6576.

[Wang et al., 2012] Wang, S. W., Zhang, Q., Streets, D. G., He, K., Martin, R. V., Lamsal, L. N., Chen, D., Lei, Y., and Lu, Z. (2012). Growth in NO_x emissions from power plants in China: bottom-up estimates and satellite observations. *Atmos. Chem. Phys.*, 12:4429–4447.

[Wenig et al., 2003] Wenig, M., Spichtinger, N., Stohl, A., Held, G., Beirle, S., Wagner, T., Jähne, B., and Platt, U. (2003). Intercontinental transport of nitrogen oxide pollution plumes. *Atmos. Chem. Phys.*, 3:387–393.

[Williams et al., 2017] Williams, J. E., Boersma, K. F., Le Sager, P., and Verstraeten, W. W. (2017). The high-resolution version of TM5-MP for optimized satellite retrievals: description and validation. *Geosci. Model Dev.*, 10:721–750.

[World Health Organisation, 2003] World Health Organisation (2003). *Health Aspects of Air Pollution with Particulate Matter, Ozone and Nitrogen Dioxide*. World Health Organisation, Bonn.

[Yang et al., 2014] Yang, K., Carn, S. A., Ge, C., Wang, J., and Dickerson, R. R. (2014). Advancing measurements of tropospheric NO2 from space: New algorithm and first global results from OMPS. *Geophys. Res. Lett.*, 41:4777–4786.

[Zara et al., 2018] Zara, M., Boersma, K. F., De Smedt, E., Richter, A., Peters, E., Van Geffen, J. H. G. M., Beirle, S., Wagner, T., Van Roozendael, M., Marchenko, S., Lamsal, L. N., and Eskes, H. J. (2018). Improved slant column density retrieval of nitrogen dioxide and formaldehyde for OMI and GOME-2A from QA4ECV: intercomparison, uncertainty characterization, and trends. *Atmos. Meas. Tech.*, 11:4033–4058.

[Zhao et al., 2020] Zhao, X., Griffin, D., Fioletov, V., McLinden, C., Cede, A., Tiefengraber, M., Müller, M., Bognar, K., Strong, K., Boersma, F., Eskes, H., Davies, J., Ogyu, A., and Lee, S. C. (2020). Assessment of the quality of tropomi high-spatial-resolution no2 data products in the greater toronto area. *Atmos. Meas. Tech.*, 13:2131–2159.

[Zhou et al., 2009] Zhou, Y., Brunner, D., Boersma, K. F., Dirksen, R., and Wang, P. (2009). An improved tropospheric NO_2 retrieval for omi observations in the vicinity of mountainous terrain. *Atmos. Meas. Tech.*, 2:401–416.

[Zhou et al., 2010] Zhou, Y., Brunner, D., Spurr, R. J. D., Boersma, K. F., Sneep, M., Popp, C., and Buchmann, B. (2010). Accounting for surface reflectance anisotropy in satellite retrievals of tropospheric NO_2. *Atmos. Meas. Tech.*, 3:1185–1203.

[Zoogman et al., 2017] Zoogman, P., Liu, X., Suleiman, R. M., Pennington, W. F., and Flittner, D. E., e. a. (2017). Tropospheric emissions: Monitoring of pollution (TEMPO). *J. Quant. Spectrosc. Radiat. Transf.*, 186:17–39.